

AD-A196 516

DTIC FILE COPY

(2)

NAVAL POSTGRADUATE SCHOOL

Monterey, California



DTIC
SELECTED
AUG 08 1988
S A H D

THESIS

Studies of Barotropic Flow Over Topography
Using a Galerkin Finite Element Model

by
Thomas I. Petroliagis

March 1988

Thesis Advisor

Roger Tery Williams

Approved for public release; distribution is unlimited.

30 8 98 24

Unclassified

SECURITY CLASSIFICATION OF THIS PAGE

REPORT DOCUMENTATION PAGE

1a. REPORT SECURITY CLASSIFICATION Unclassified		1b. RESTRICTIVE MARKINGS	
2a. SECURITY CLASSIFICATION AUTHORITY		3. DISTRIBUTION/AVAILABILITY OF REPORT Approved for public release; distribution is unlimited	
2b. DECLASSIFICATION/DOWNGRADING SCHEDULE			
4. PERFORMING ORGANIZATION REPORT NUMBER(S)		5. MONITORING ORGANIZATION REPORT NUMBER(S)	
6a. NAME OF PERFORMING ORGANIZATION Naval Postgraduate School	6b. OFFICE SYMBOL (If applicable) 63	7a. NAME OF MONITORING ORGANIZATION Naval Postgraduate School	
6c. ADDRESS (City, State, and ZIP Code) Monterey, California 93943-5000		7b. ADDRESS (City, State, and ZIP Code) Monterey, California 93943-5000	
8a. NAME OF FUNDING SPONSORING ORGANIZATION	8b. OFFICE SYMBOL (If applicable)	9. PROCUREMENT INSTRUMENT IDENTIFICATION NUMBER	
8c. ADDRESS (City, State, and ZIP Code)		10. SOURCE OF FUNDING NUMBERS	
		PROGRAM ELEMENT NO.	PROJECT NO.
		TASK NO.	WORK UNIT ACCESSION NO.
11. TITLE (Include Security Classification) Studies of Barotropic Flow over Topography using a Galerkin Finite Element Model			
12. PERSONAL AUTHOR(S) Petroliagis, Thomas I.			
13a. TYPE OF REPORT Master's Thesis	13b. TIME COVERED FROM TO	14. DATE OF REPORT (Year, Month, Day) 1988 March	15. PAGE COUNT 200
16. SUPPLEMENTARY NOTATION The views expressed in this thesis are those of the author and do not reflect the official policy or position of the Department of Defense or the U.S. Government			
17. COSATI CODES		18. SUBJECT TERMS (Continue on reverse if necessary and identify by block number) Numerical Weather Prediction, Finite Elements, Rossby Waves, Hydraulic Jumps	
19. ABSTRACT (Continue on reverse if necessary and identify by block number)			
<p>A finite element shallow-water model is tested with two types of surface topography. The model uses rectangular subdivisions in a vorticity-divergence formulation, and a semi-explicit time discretization. In the first experiment an east-west ridge or valley is placed in a channel with east-west periodic conditions. Linear quasi-geostrophic solutions are derived with the rigid lid assumption. The Rossby waves are successfully simulated in the model with linear solutions as the initial conditions. The model phase speeds are very close to the analytic values when the latter</p>			
20. DISTRIBUTION/AVAILABILITY OF ABSTRACT <input checked="" type="checkbox"/> UNCLASSIFIED/UNLIMITED <input type="checkbox"/> SAME AS RPT <input type="checkbox"/> DTIC USERS		21. ABSTRACT SECURITY CLASSIFICATION Unclassified	
22a. NAME OF RESPONSIBLE INDIVIDUAL R. T. Williams		22b. TELEPHONE (Include Area Code) (408) 646-2296	22c. OFFICE SYMBOL 63Wu

19. ABSTRACT (Continued) :

are properly corrected. In the second experiment a ridge is placed across the channel and the Coriolis parameter is set to zero. The initial conditions consist of a uniform flow through the channel and constant free-surface height. The numerical simulations agree with hydraulic jump theory. In the jump cases the model predicts increasing wind speeds and decreasing free surface heights. Higher spatial resolution would be required to properly simulate the details of the hydraulic jump formation.



Accession For	
NTIS GRA&I	<input checked="" type="checkbox"/>
DTIC TAB	<input type="checkbox"/>
Unannounced	<input type="checkbox"/>
Justification	
By _____	
Distribution / _____	
Availability Codes	
Dist	Avail and/or
	Special
R-1	

Approved for public release; distribution unlimited

Studies of Barotropic Flow Over Topography
Using a Galerkin Finite Element Model

by

Thomas I. Petroliagis
Captain, Hellenic Air Force
B.S., Hellenic Air Force Academy, 1980
B.S., University of Thessaloniki, Greece, 1986

Submitted in partial fulfillment of the
requirements for the degree of

MASTER OF SCIENCE IN METEOROLOGY

from the

NAVAL POSTGRADUATE SCHOOL

March 1988

Author:

Thomas I. Petroliagis

Thomas I. Petroliagis

Approved by

Roger Terry Williams

Roger Terry Williams, Thesis Advisor

Robert Lee Haney

Robert Lee Haney, Second Reader

Robert Joseph Renard

Robert Joseph Renard, Chairman,

Department of Meteorology

Gordon E. Schacher

Gordon E. Schacher,
Dean of Science and Engineering

ABSTRACT

A finite element shallow-water model is tested with two types of surface topography. The model uses rectangular subdivisions in a vorticity-divergence formulation, and a semi-implicit time discretization. In the first experiment an east-west ridge or valley is placed in a channel with east-west periodic conditions. Linear quasi-geostrophic solutions are derived with the rigid lid assumption. The Rossby waves are successfully simulated in the model with linear solutions as the initial conditions. The model phase speeds are very close to the analytic values when the latter are properly corrected. In the second experiment a ridge is placed across the channel and the Coriolis parameter is set to zero. The initial conditions consist of a uniform flow through the channel and constant free-surface height. The numerical simulations agree with hydraulic jump theory. In the jump cases the model predicts increasing wind speeds and decreasing free surface heights. Higher spatial resolution would be required to properly simulate the details of the hydraulic jump formation.

TABLE OF CONTENTS

I.	INTRODUCTION.....	001
	A. GENERAL.....	001
	B. BACKGROUND.....	002
	C. OBJECTIVES.....	005
II.	THE FINITE ELEMENT METHOD.....	007
	A. HISTORICAL INTRODUCTION.....	007
	B. FINITE ELEMENT APPROXIMATIONS.....	009
	C. THE METHOD OF WEIGHTED RESIDUALS.....	010
	D. GALERKIN METHOD.....	012
	E. TWO-DIMENSIONAL BASIS FUNCTIONS.....	016
	1. Step I.....	019
	2. Step II.....	020
	3. Step III.....	022
	4. Step IV.....	028
III.	THE SHALLOW-WATER MODEL AND THE TOPOGRAPHIC ROSSBY WAVE.....	037
	A. GENERAL.....	037
	B. THE SHALLOW-WATER MODEL.....	037

C.	SMALL-AMPLITUDE MOTIONS.....	039
D.	THE TOPOGRAPHIC ROSSBY WAVE.....	045
IV. HYDRAULIC JUMPS IN ROTATING AND NONROTATING SYSTEMS.....		054
A.	GENERAL.....	054
B.	HYDRAULIC JUMPS IN A NONROTATING SYSTEM.....	055
C.	HYDRAULIC JUMPS IN A ROTATING SYSTEM.....	063
V. MODEL DESCRIPTION.....		069
A.	GENERAL.....	069
B.	EQUATION FORMULATION.....	071
C.	STABILITY ANALYSIS.....	083
VI. INITIAL CONDITIONS.....		086
A.	TOPOGRAPHIC ROSSBY WAVE.....	086
B.	HYDRAULIC JUMPS.....	112
VII. EXPERIMENTS AND RESULTS.....		115
A.	EXPERIMENT I.....	115
B.	RESULTS I.....	120
C.	EXPERIMENT II.....	150

D. RESULTS II.....	151
VIII. CONCLUSIONS.....	166
APPENDIX: NUMERICAL QUADRATURE.....	168
LIST OF REFERENCES.....	172
INITIAL DISTRIBUTION LIST.....	176

LIST OF TABLES

I.	Relationship between Local Numbers and Global Node Numbers.....	027
II.	Evaluatd Integrals for One Element in Local Coordinates for equation (2-20).....	029
III.	Evaluatd Integrals for the Four Elements of Fig. 2.4, in Global Coordinates for equation (2-20).....	030
IV.	Numerical solutions of equation (6-44), obtained using Newton's method.....	097
V.	Peak (in geopotential meters and in meters), and south slope values for cases I through VII.....	121
VI.	Estimated, estimated corrected by the free surface term, estimated corrected by both the free surface and H terms, and observed phase speed values (in m/s), for cases II through VII.....	143

VII.	Froude number (F_0), maximum height of the ridge (R), parameter F, mean depth (H), mean flow (U), and domain (D), for cases I through V.....	153
VIII.	Parameter F, maximum height of the ridge (R), domain (D), and classification of the asymptotic flow conditions, for cases I through V.....	154

LIST OF FIGURES

2.1	Schematic representation of the one-dimensional weighting functions for the Galerkin method. (It is assumed that the chapeau function is used as a basis function).....	013
2.2	As in Fig. 2.1, except for the subdomain method.....	014
2.3	As in Fig. 2.1, except for the collocation method.....	015
2.4	Discretized domain for two-dimensional heat flow. Finite element nodes are indicated by small circles, and the elements themselves by Roman numerals.....	017
2.5	Two-dimensional basis function that is linear along each side.....	018
2.6a	Rectangular element in (x,y) coordinates.....	023
2.6b	Same element as Fig. 2.6a transformed into the (ξ, η) local coordinate system.....	024

3.1	The Shallow-Water Model.....	038
3.2	The infinite channel of width L, rotating with with angular velocity $f/2$	047
3.3	A schematic representation of the dispersion diagram for Poincare, Kelvin, and topographic Rossby waves in a channel.....	052
4.1	A cross section view of the one-dimensional Shallow-Water Model with a mean flow u	056
4.2	Parameter R as a function of solution U_* , as given by equation (4-12) for $F^2 = 1.02$	060
4.3	As in Fig. 4.2, except for $F^2 = 1.125$	061
4.4	As in Fig. 4.2, except for $F^2 = 3.0$	062
4.5	Classification of asymptotic flow conditions as a function of the maximum height of the ridge, $R_{critical}$, and initial flow speed parameter F.....	064

5.1	Rectangular uniform subdivision for a channel in Cartesian coordinates.....	070
6.1	Schematic representation of the non-dimensional domain of integration.....	091
6.2	Graph of the solution $\psi_2(y)$ where the upper part of the channel controls c, obtained from equations (6-48), and (6-49).....	099
6.3	As in Fig. 6.2, except for equations (6-50), and (6-51).....	101
6.4	As in Fig. 6.2, except for equations (6-52), and (6-53).....	103
6.5	Graph of the solution $\psi_1(y)$ where the lower part of the channel controls c, obtained from equations (6-54), and (6-55).....	104
6.6	As in Fig. 6.5, except for equations (6-56), and (6-57).....	106
6.7	As in Fig. 6.5, except for equations (6-58), and (6-59).....	107
6.8	Initial conditions for the GFEM model with a rectangular	

subdivision, and wave number one. Contour intervals are 600 m ² /s ² for geopotential height, 0.2 m/s for u and v, 0.6×10^{-6} s ⁻¹ for vorticity. Nodal points are denoted by an x.....	113
7.1 Schematic representation of the domain of integration.....	117
7.2 Schematic representation of the bottom topography for the case of triangular mountain.....	118
7.3 As in Fig. 7.2, except for the case of triangular valley.....	119
7.4 Initial conditions for experiment I (cases I through VII). Contour intervals are 600 m ² /s ² for geopotential height, and 0.2 m/s for u and v. Nodal points are denoted by an x.....	122
7.5 As in Fig. 7.4, except for case I, and a 48 hour integration.....	123
7.6 As in Fig. 7.5, except for a 96 hour integration.....	124
7.7 As in Fig. 7.5, except for case II.....	125

7.8	As in Fig. 7.6, except for case II.....	126
7.9	As in Fig. 7.5, except for case III.....	128
7.10	As in Fig. 7.6, except for case III.....	129
7.11	As in Fig. 7.5, except for case IV.....	130
7.12	As in Fig. 7.6, except for case IV.....	131
7.13	As in Fig. 7.5, except for case V.....	132
7.14	As in Fig. 7.6, except for case V.....	133
7.15	As in Fig. 7.5, except for case VI.....	135
7.16	As in Fig. 7.6, except for case VI.....	136
7.17	As in Fig. 7.5, except for case VII.....	137
7.18	As in Fig. 7.6, except for case VII.....	138
7.19	The required ambient potential-vorticity gradient.	

A clue for the physical explanation of the topographic Rossby wave oscillation.....	139
7.20 The position of the three-point vortices L, C, and R at three successive times. Initially collinear and positioned along an isobath, C is displaced upwards, producing velocities at L and R which move them as shown. The vorticity induced on L and R produces a velocity at C with a tendency to restore it to its original position.....	141
7.21 Comparison of the observed phase speed values, with estimated, estimated corrected by the free surface term, and estimated corrected by both the free surface and H terms, phase speed values (in m/s) for cases II through IV (scatter diagram).....	144
7.22 As in Fig. 7.21, except for cases V through VII.....	145
7.23 As in Fig. 7.21, except for bar representation.....	148
7.24 As in Fig. 7.22, except for bar representation.....	149
7.25 Schematic representation of the bottom topography,	

along x-axis, valid for each node per horizontal row, for the hydraulic jump case.....	152
7.26 U-component amplitude as a function of time for case I.....	155
7.27 Φ -amplitude as a function of time for case I.....	156
7.28 As in Fig. 7.26, except for case II.....	157
7.29 As in Fig. 7.27, except for case II.....	159
7.30 As in Fig. 7.26, except for case III.....	160
7.31 As in Fig. 7.27, except for case III.....	161
7.32 As in Fig. 7.26, except for case IV.....	162
7.33 As in Fig. 7.27, except for case IV.....	163
7.34 As in Fig. 7.26, except for case V.....	164
7.35 As in Fig. 7.27, except for case V.....	165

A.1	Orthogonal axis transformation for rectangular integration formulas.....	169
-----	---	-----

ACKNOWLEDGEMENTS

The author expresses his thanks to Professors Roger Terry Williams and Robert Lee Haney for their invaluable encouragement, direction and support in all the phases of this study.

The author also, is especially grateful to his wife, *Maria*, for her love, patience and understanding which made this work possible.

I. INTRODUCTION

A. GENERAL

Wilhelm Bjerkens (1904) was the first to point out that the future meteorological conditions can in principle be obtained by an integration of differential equations which govern the behavior of the atmosphere. Such an integration performed using numerical methods is called *numerical weather prediction.*

Richardson was the first to attempt a numerical weather prediction. After very long and time-consuming computations, he obtained a totally unacceptable result (Richardson, 1922). That wrong result, and Richardson's estimate that 64,000 men are required to advance the calculations as fast as the weather itself is advancing, left some doubt about the practical use of the method. However, a number of developments that followed improved the situation. Mainly due to the work of Rossby in the late 1930's, it became clear that even a rather simple equation, one that describes the conservation of absolute vorticity following the motion of air particles, suffices for an approximate description of large scale motions of the atmosphere.

Finally, in 1945, the first electronic computer, ENIAC, was constructed. The absolute vorticity conservation equation, and ENIAC, were used by Charney, Fjortoft and Von Neumann in the late 1940's for the first successful numerical forecast (Charney *et al.* 1950). Much faster

computers, and improved understanding of computational problems, now also enable long-term integrations of the basic primitive equations. With the introduction of each new generation of computers, the gap between numerical forecasts and atmospheric observations has decreased, but the rate at which this gap is decreasing appears to be leveling off. This indicates that technological improvements in computing power may not be the primary limitation to better numerical forecasts.

During the past 15 years, there has been a significant effort within the numerical weather prediction area in developing limited-area, fine-mesh primitive equations models and applying them to operational, short range weather forecasts. An important practical motivation for the development of regional models has been the limited success of operational global models in the prediction of precipitation and severe weather. A parallel motivation for the development of regional models is their potential scientific value to researchers studying the structure and dynamics of mesoscale phenomena. (Keyser and Uccellini, 1987)

B. BACKGROUND

There are two fundamental methods of simulating the atmospheric flow; physical-models and mathematical-models techniques. With the physical-models technique, we construct scale model replicas of observed ground surface characteristics and insert them into a chamber such as a wind tunnel. The flow of air in this chamber is adjusted so as to best

represent the large scale, observed atmospheric conditions. Mathematical modeling, on the other hand, makes use of such basic analysis techniques as algebra and calculus to solve directly the equations governing atmospheric flows.

Numerical solution of the equations of motion is performed using the grid point method for most applications. Following this method a set of points is introduced in the region of interest and dependent variables are initially defined and subsequently computed at these points. This set of points is called a grid. It is very important to note that most of the time the grid points are at fixed locations in the horizontal. This means that, according to the Eulerian system of equations, space and time coordinates are chosen as independent variables.

With the grid point method, the most common way of solving the governing equations is to find approximate expressions for derivatives appearing in the equations. The required approximate expressions are defined using values of the dependent variables only defined at the grid points, and at discrete time intervals. Thus, they are formed using differences of dependent variables over finite space and time intervals ; that is the reason why this approach is called the finite difference method. The approximations for derivatives are then used to construct a system of algebraic equations that approximates the governing partial differential equations. This set of algebraic equations is to be solved, usually using an electronic computer, by a proper step-wise procedure in time.

A major limiting factor of finite difference approximations is the truncation error. That is, the smaller the grid interval, the smaller the truncation error. For a finite difference model to improve its accuracy, it would require increasing the grid matrix density. This would require increased computer storage and computational time. The problem here is not a simple one. It goes beyond numerical techniques and computer technology. For instance if we further reduce the grid spacing on the 7LPE (National Weather Service 7 Layer Primitive Equation Model) we do not get any significant improvement in the accuracy of the solution (Woodward, 1981). The required additional computer capability can not be utilized using finite difference methods. Therefore, new numerical integration techniques must be investigated.

Two alternative techniques, the spectral method and the finite element method, have been the subject of intensive research. Both the spectral and finite element methods require more computational time per forecast time step than does the finite difference method. That is why both the spectral and finite element methods must utilize efficient numerical techniques to be considered a viable option for numerical weather prediction. For long range weather predictions, the spectral method appears to be a natural method, when applied over the globe or hemisphere. This is due to the existence of efficient transforms for the nonlinear terms in spherical geometry. However, the spherical harmonics are globally rather than locally defined.

That is the reason why the finite element method appears to be more suitable for problems of more detailed limited area forecasting.

The Galerkin Finite Element Method (GFEM) has the potential to increase efficiently the spatial resolution for the purpose of simulating accurately the small-scale processes. More specifically, the GFEM model used by Hinsman, 1983, has demonstrated desirable characteristics. It propagates atmospheric waves better than an equivalent finite difference model. It also allows variable-resolution grids and responds better than an equivalent finite difference model near the smallest gridlength. Moving grids can be achieved with no apparent noise generation. Finally, it can utilize direct solvers and is a natural choice for vectorization on large computers. Furthermore, the superior small-scale response of the GFEM indicates potential increase in skill for regional forecasting, and it truly is a viable option for simulation of atmospheric flow.

C. OBJECTIVES

The main objective of this study is to test the Galerkin Finite Element model which was developed by Hinsman (1983), with topography. This shallow-water model uses bilinear basis functions. An earlier study with the same model was carried out by Neta *et al.* (1986), in which the bottom topography changes linearly to the north.

In this thesis two types of bottom topography will be considered in a channel domain encompassed by solid north-south walls with east-west

boundary conditions. In the first case the bottom is composed of two regions. These regions have a constant but opposite northward slope so that they can form either an east-west oriented ridge or an east-west oriented valley in the surface topography. Lines of constant bottom height run parallel to the x-axis, and pure geostrophic motion is possible only if the v-component of the velocity is identically zero. If we consider no mean flow and no beta effect, topographic Rossby waves can exist moving either east or west depending on the slope of the bottom.

In the second case, a mean zonal flow passes over a ridge which extends north-south across the channel. It is clear now that the lines of constant bottom height run parallel to the y-axis. The Coriolis parameter for this case is set to zero, and the formation of hydraulic jumps is to be investigated for different values of the mean flow and peak of the topographic ridge.

II. THE FINITE ELEMENT METHOD

A. HISTORICAL INTRODUCTION

The finite element concept is to a large extent physical rather than abstract in nature, and it has been used in a variety of forms for centuries. The basic idea has always been to replace an actual problem by a simpler one. In other words the finite element method is the replacement of continuous functions by piecewise approximations, usually polynomials. Indeed the early geometers used "finite elements" to determine an approximate value of π . They did this by bounding a quadrant of a circle with inscribed and circumscribed polygons, the straight-line segments being the finite element approximations to an arc of the circle. In this way they were able to obtain extremely accurate estimates. Upper and lower bounds were obtained, and by taking an increasing number of elements, monotonic convergence to the exact solution would be expected. Archimedes used these ideas to determine areas of plane figures and volumes of solids, although of course he did not have a precise concept of a limiting procedure. The interesting point here is that while many problems of applied mathematics are posed in terms of differential equations, the finite element solution of such equations utilizes ideas which are in fact much older than those used to set up the equations initially.

The modern use of finite elements really started in the field of structural engineering. Probably the first attempts were by Hrennikoff

(1941) and McHenry (1943) who developed analogies between actual discrete elements and the corresponding portions of a continuous solid. The term "finite element" was introduced later by Clough (1960) in a paper describing an application in plane elasticity.

The engineers had put the finite element method on the map as a practical technique for solving their elasticity problems, and although a rigorous mathematical basis had not been developed, the next few years saw an expansion of the method to solve a large variety of structural problems. The workers in the early-1960s soon turned their attention towards the solution of non-linear problems. Turner *et al.* (1960) showed how to use an incremental technique to solve geometrically non-linear problems, i. e., problems in which the strains remains small but the displacements are large. Stability analysis also comes into this category and was discussed by Martin (1965). Plasticity problems, involving non-linear material behavior were modelled at this time (Gallagher *et al.* 1962), and the method was also applied to the solution of problems in visco-elasticity (Zienkiewicz *et al.* 1968).

Finally, besides the static analysis, dynamic problems were also being tackled, and Archer (1963) introduced the concept of the consistent mass matrix. Both vibration problems (Zienkiewicz *et al.* 1966) and transient problems (Koenig and Davids, 1969) were considered. Thus the period from its conception in early-1950s to the mid-1960s saw the method being applied extensively by the engineering community. Once it was realized

that the method could be interpreted in terms of variational methods, the mathematicians and engineers were brought together, and many extensions of the method to new areas soon followed. In particular it was realized that the concept of piecewise polynomial approximation offered a simple and efficient procedure for the application of the classical Rayleigh-Ritz method. The method had now become an important technique from both a practical and theoretical point of view, and the number of published papers using this method began to increase at a tremendous rate.

In the area of meteorology also, the finite-element method has been successfully employed in the horizontal representation of atmospheric variables in numerical weather prediction and atmospheric modeling (Cullen, 1974a, 1974b, 1979; Hinsman, 1975, 1983; Staniforth and Mitchell, 1977, 1978). The finite element method when applied to meteorological equations gives very accurate phase propagation and also handles nonlinearities very well.

B. FINITE ELEMENT APPROXIMATIONS

In contrast to the finite difference schemes wherein the domain of interest is replaced by a set of discrete points, in the finite element method the domain is divided into subdomains called finite elements. The unknown function, let us name it u , is represented within each element by an interpolating polynomial which is continuous along with its derivatives to a specified order within the element. Generally, the interpolating function is

of lower-order continuity between elements than within an element. Thus the fundamental building block in the finite element method is the subdomain or element.

C. THE METHOD OF WEIGHTED RESIDUALS

There are several ways that can lead us to the same finite element formulation. A conceptually simple approach can be formulated using the method of weighted residuals. The two primarily special cases of the method of weighted residuals (MWR) are the Galerkin and the collocation methods.

In the method of weighted residuals, the desired function $u(\cdot)$ is replaced by a finite series approximation as

$$u(\cdot) \approx \hat{u}(\cdot) = \sum_{j=1}^N U_j \phi_j(\cdot). \quad (2-1)$$

In general, the set of functions $\phi_j(\cdot)$, $j = 1, 2, \dots, N$, can be defined over both the time and space domain and U_j , $j = 1, 2, \dots, N$, are undetermined coefficients. The equation (2-1) can be written

$$\hat{u}(\cdot) = U_0 \phi_0(\cdot) + \sum_{j=1}^{N-1} U_j \phi_j(\cdot), \quad (2-2)$$

where $\phi_j(\cdot)$ satisfy the homogeneous boundary conditions. The functions $\phi_j(\cdot)$ are chosen to be polynomials that satisfy certain of the boundary conditions imposed on the problem. These functions are variously denoted shape functions, basis functions, and interpolation functions, depending upon the discipline in which the method is being applied. Even if we choose the basis functions to satisfy all boundary conditions, they will not normally satisfy the PDE as well. If we now substitute the $\hat{u}(\cdot)$ into the PDE, say $L\hat{u} - f = 0$, we can easily get

$$L\hat{u}(\cdot) - f = R(\cdot), \quad (2-3)$$

where $R(\cdot)$ is a residual.

Our objective at this point should be to select the undetermined coefficients U_j such that this residual is minimized in some sense. A straightforward scheme would be to set the integral of $R(\cdot)$ to zero as

$$\int_t \int_v R(\cdot) dv dt = 0. \quad (2-4)$$

This scheme, however, generates only one equation for the N unknown coefficients U_j . It can be suitably modified by introducing weighting functions $w_i(\cdot)$, $i = 1, 2, \dots, N$.

Setting the integral of each weighted residual to zero yields n independent equations

$$\int \int_R (\bullet) w_i(\bullet) dv dt = 0, \quad i = 1, 2, \dots, N. \quad (2-5)$$

At this point we can solve equation (2-5), in theory at least, for N unknown coefficients. Equation (2-5) represents the general equation describing the MWR, and a multiplicity of schemes arise out of this one expression through the definition of the weighting functions w_i .

Among the MWR family of methods, the Galerkin, subdomain, and collocation schemes are most commonly encountered in practice. The one-dimensional weighting function for the Galerkin scheme is illustrated in Fig. 2.1, for the subdomain scheme in Fig. 2.2, and for the collocation scheme in Fig. 2.3.

D. GALERKIN METHOD

The Galerkin method results when the weighting function is chosen to be the basis function, as defined in (2-1). Thus we have

$$\int \int_R R(\bullet) \phi_i(\bullet) dv dt = 0, \quad i = 1, 2, \dots, N. \quad (2-6)$$

The basis functions are formally required to be members of a complete set of functions. Because a complete set of functions can exactly represent

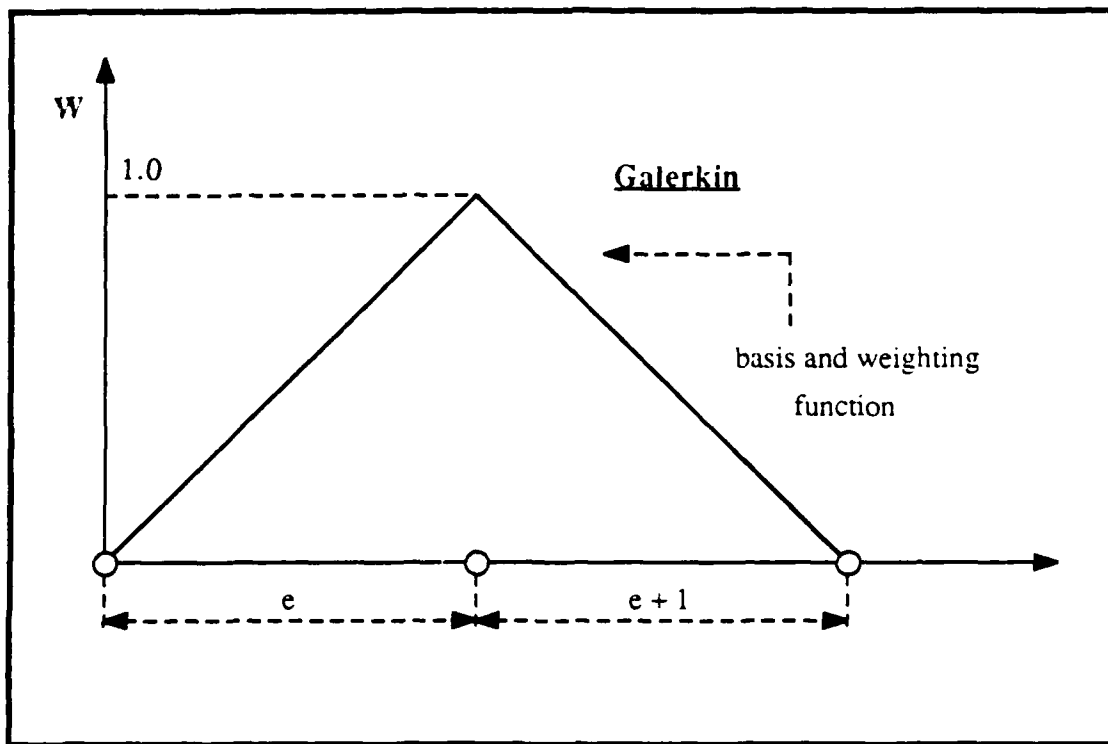


Fig. 2.1 Schematic representation of the one-dimensional weighting functions for the Galerkin method. (It is assumed that the chapeau function is used as a basis function).

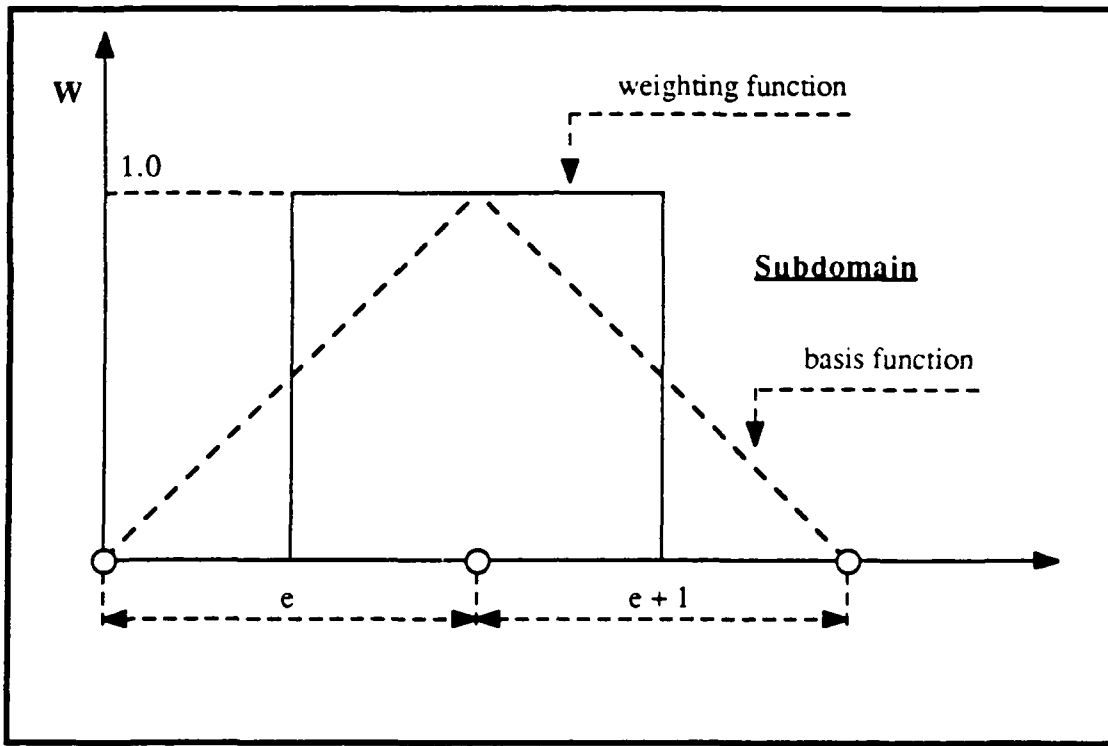


Fig. 2.2 As in Fig. 2.1, except for the subdomain method.

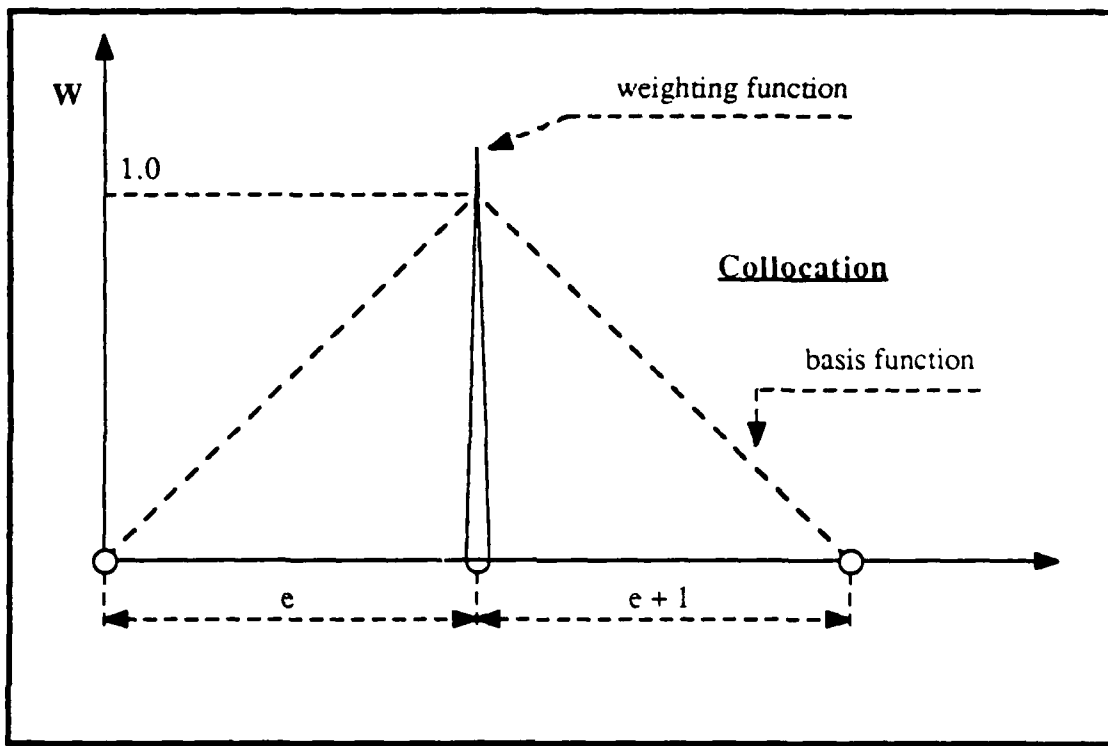


Fig. 2.3 As in Fig. 2.1, except for the collocation method.

any function of a given class, the series of (2-1) is inherently capable of representing the exact solution as the number of terms in the series is increased.

The requirement of completeness allows an alternative interpretation of the Galerkin formulation. A continuous function must be zero if it is orthogonal to every member of a complete set. The Galerkin method can be viewed as a scheme in which the residual is forced to zero in the sense that it is made orthogonal to the complete set of functions $\phi_i(\bullet)$.

In Fig. 2.1 the weighting function (and therefore the basis function) is a hatshaped, piecewise linear function, and because of its hatlike appearance, it is sometimes called a "chapeau" function. It is often encountered in the formulation of the finite element method. The chapeau function is the simplest of the basis functions in common use.

E. TWO-DIMENSIONAL BASIS FUNCTIONS

The extension of the weighted residual method to higher dimensions is relatively straightforward, provided that regular rectangular subspaces are employed. We can easily visualize the two-dimensional case using an elementary example, (Lapidus and Pinder, 1982). The discretized domain is simply illustrated in Fig. 2.4, and the two-dimensional basis function that is linear along each side in Fig. 2.5.

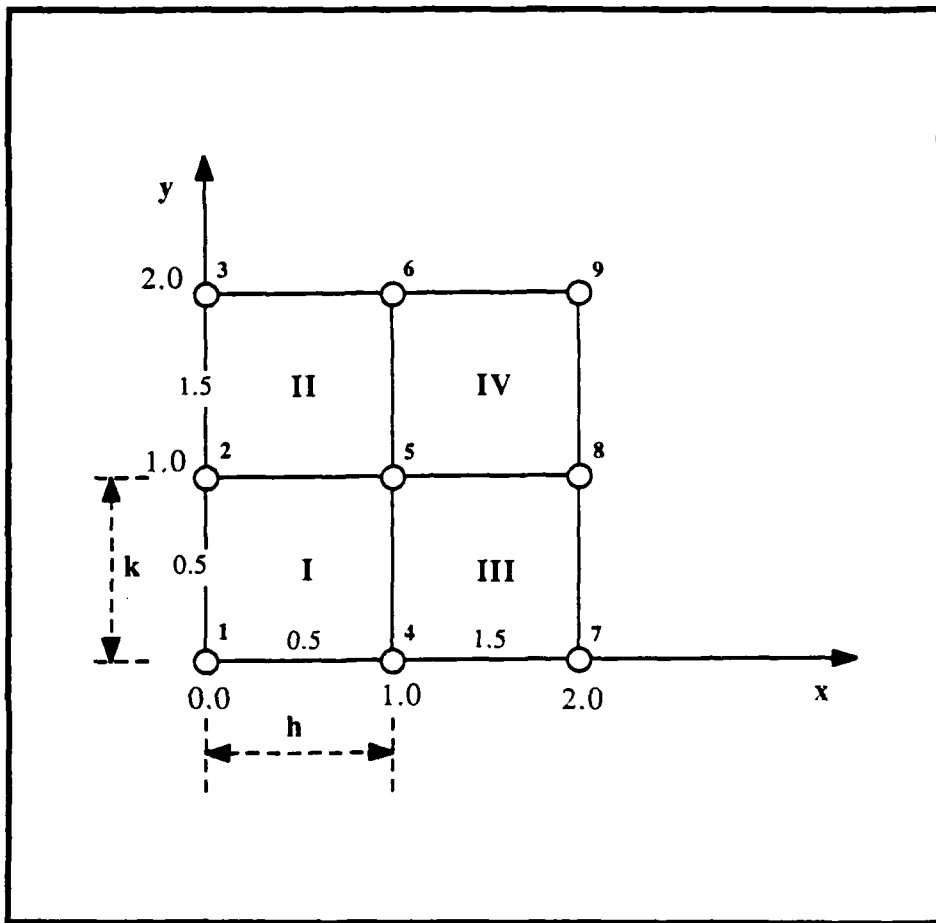


Fig. 2.4 Discretized domain for two-dimensional heat flow.
Finite element nodes are indicated by small circles, and
the elements themselves by Roman numerals.

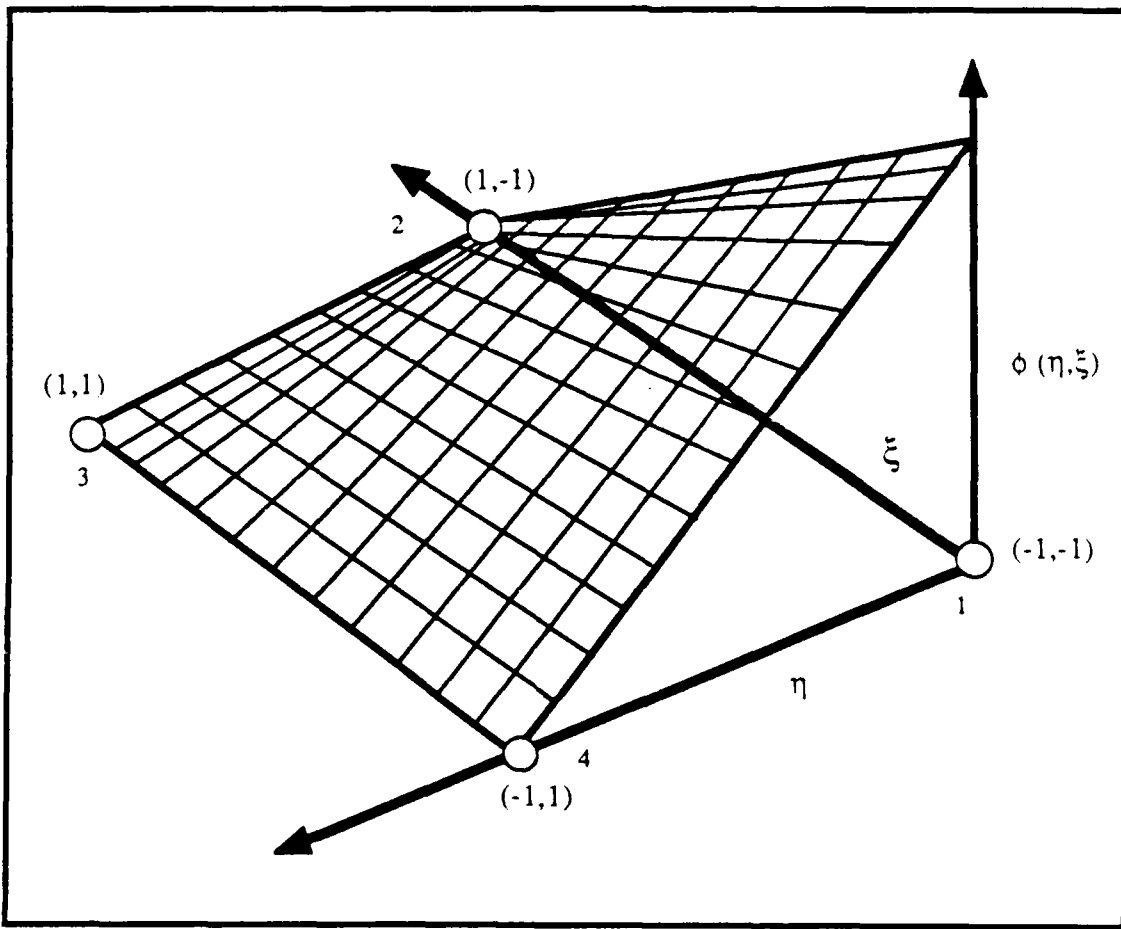


Fig. 2.5 Two-dimensional basis function that is linear along each side.

Consider now the problem of two-dimensional, time-independent heat flow in a rectangular plate with a heat source located at the center of the plate. The governing equations for this problem will be given by

$$f(T) = T_{xx} + T_{yy} = Q \quad (2-7)$$

$$T(x,2) = 1 \quad (2-8)$$

$$T(0,y) = 1 \quad (2-9)$$

$$T_y(x,0) = 0 \quad (2-10)$$

$$T_x(2,y) = 0 \quad (2-11)$$

$$Q(x,y) = Q_w \delta(x-1) \delta(y-1), \quad (2-12)$$

where x and y are Cartesian coordinates, Q_w is the heat source, and δ is the Dirac delta function.

1. Step I

Let us first define the trial functions:

$$T(x,y) = \hat{T}(x,y) = \sum_{j=1}^9 T_j \phi_j(x,y). \quad (2-13)$$

For convenience, it is advantageous to define basis functions in local (ξ, η) coordinates where upon (2-13) becomes, for each element,

$$T(x,y) \approx \hat{T}(x,y) = \sum_{j=1}^4 T_j \phi_j(\xi, \eta) \quad (2-14)$$

and $\phi_j(\xi, \eta)$ are bilinear chapeau functions such as those illustrated in Fig. 2.5.

2. Step II

At this point we can easily formulate the integral equations using Galerkin's procedure. We can visualize the whole procedure as the requirement of orthogonality between the residual R and each basis function, as

$$\int_A R(x,y) \phi_i(x,y) dx dy = 0, \quad i = 1, \dots, 9, \quad (2-15)$$

where

$$R(x,y) \equiv f(T) - Q. \quad (2-16)$$

A is the domain of integration and f is defined by (2-7). Substituting (2-7), and (2-16) into (2-15) yields

$$\int_A (T_{xx} - T_{yy} - Q) \phi_i(x,y) dx dy = 0, \quad i = 1, \dots, 9. \quad (2-17)$$

Applying Green's theorem to (2-17) to incorporate second- and third-type boundary conditions directly into the set of integral equations, equation (2-17) becomes

$$\int_A (T_x \phi_{xi} + T_y \phi_{yi} + Q \phi_i) dx dy - \int_S (\hat{T}_x l_x + \hat{T}_y l_y) \phi_i ds = 0, \\ i = 1, \dots, 9, \quad (2-18)$$

where l_x and l_y are direction cosines with respect to the normal to the curve S , the boundary of the domain A . In this problem, the second term of (2-18) will be used to conveniently define the zero-gradient Neumann boundary conditions of (2-10) and (2-11).

If we now substitute the trial functions, as defined by (2-13) into (2-18) we can obtain the following set of algebraic equations

$$\int_A \left(\sum_{j=1}^9 T_j (\phi_{xj} \phi_{xi} + \phi_{yj} \phi_{yi}) + Q \phi_i \right) dx dy \\ - \int_S (\hat{T}_x l_x + \hat{T}_y l_y) \phi_i ds = 0, \quad i = 1, \dots, 9. \quad (2-19)$$

Because ϕ_i is defined such that it is nonzero only over elements adjacent to mode i (see Fig. 2.4 and 2.5) the integrations of (2-19) may be performed piecewise over each element and subsequently summed. Thus we can write

$$\sum_{e=1}^4 \int_{A_e} \left(\sum_{j=1}^9 T_j (\phi_{xj} \phi_{xi} + \phi_{yj} \phi_{yi}) + Q\phi_i \right) dx dy$$

$$- \int_{S_e} (\hat{T}_x l_x + \hat{T}_y l_y) \phi_i ds = 0, \quad i = 1, \dots, 9, \quad (2-20)$$

where A_e is the area of element e , and S_e is the curve bounding A_e .

3. Step III

It is now time to formulate the matrix equation. In general, the best way is to express (2-20) in terms of the local (ξ, η) coordinate system to facilitate integration (see Fig. 2.6a, Fig. 2.6b). This is easily accomplished provided that the relationship between derivatives of ϕ_j in each coordinate system is readily available. To find this relationship, we have to employ the chain rule to obtain

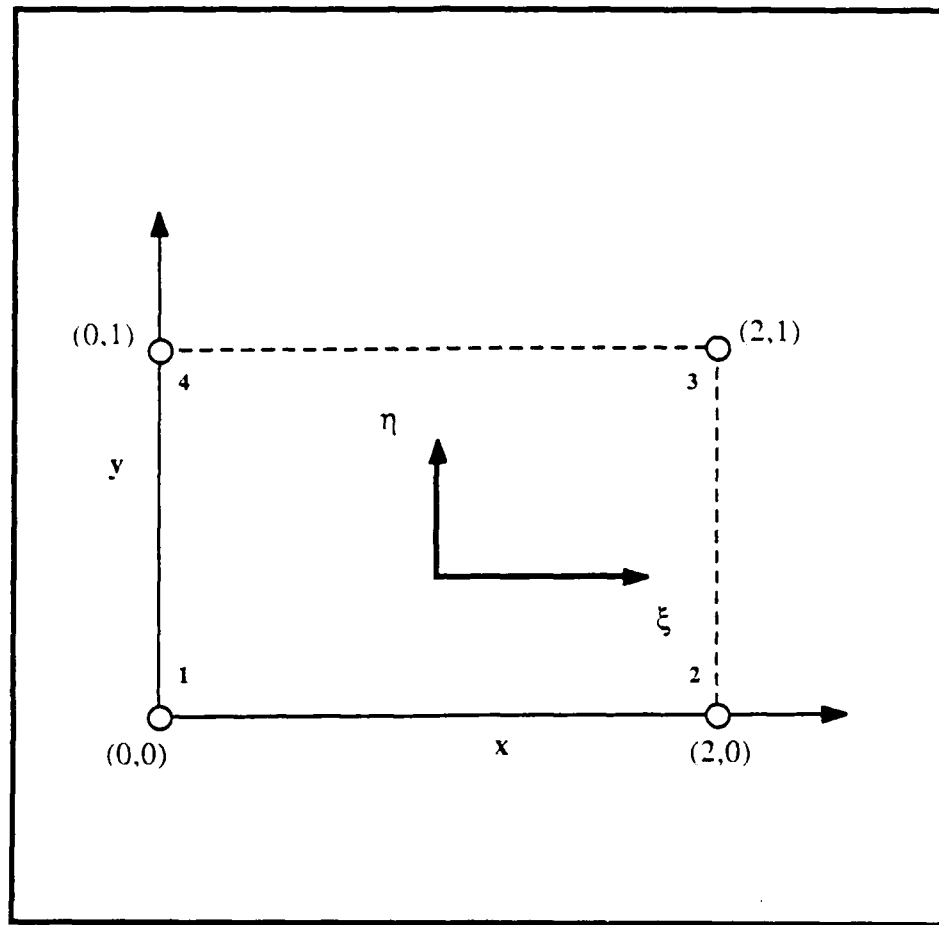


Fig. 2.6a Rectangular element in (x,y) coordinates.

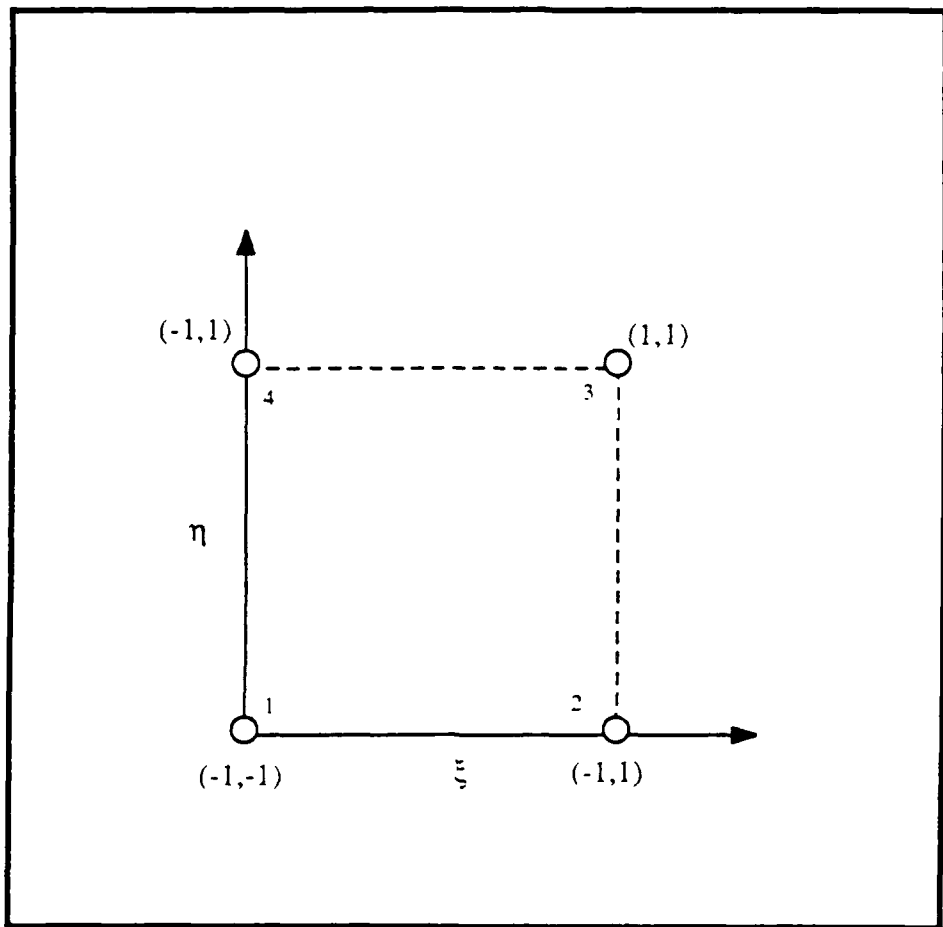


Fig. 2.6b Same element as Fig. 2.6a transformed into the (ξ, η) local coordinate system.

$$\frac{\partial \phi_j}{\partial \xi} = \frac{\partial \phi_j}{\partial x} \frac{\partial x}{\partial \xi} + \frac{\partial \phi_j}{\partial y} \frac{\partial y}{\partial \xi},$$

$$\frac{\partial \phi_j}{\partial \eta} = \frac{\partial \phi_j}{\partial x} \frac{\partial x}{\partial \eta} + \frac{\partial \phi_j}{\partial y} \frac{\partial y}{\partial \eta}.$$

This set of equations can be written as

$$\begin{bmatrix} (\phi_j)_{\xi} \\ (\phi_j)_{\eta} \end{bmatrix} = \begin{bmatrix} (x)_{\xi} & (y)_{\xi} \\ (x)_{\eta} & (y)_{\eta} \end{bmatrix} \begin{bmatrix} (\phi_j)_x \\ (\phi_j)_y \end{bmatrix}$$

or

$$\begin{bmatrix} (\phi_j)_x \\ (\phi_j)_y \end{bmatrix} = [J]^{-1} \begin{bmatrix} (\phi_j)_{\xi} \\ (\phi_j)_{\eta} \end{bmatrix}, \quad (2-21)$$

where $[J]$ is the Jacobian matrix. For our problem we can easily evaluate the $[J]$ as

$$[J] = \begin{bmatrix} 0.5 & 0.0 \\ 0.0 & 0.5 \end{bmatrix}$$

and the $[J]^{-1}$ as

$$[J]^{-1} = \begin{bmatrix} 2.0 & 0.0 \\ 0.0 & 2.0 \end{bmatrix}. \quad (2-22)$$

Equations (2-20) and (2-22) may be combined, which can give us

$$\sum_{e=1}^4 \int_{-1}^{+1} \int_{-1}^{+1} \left(\sum_{j=1}^9 T_j (4 \phi_{\xi j} \phi_{\xi i} + 4 \phi_{\eta j} \phi_{\eta i}) + Q \phi_i \right) \frac{1}{4} d\xi d\eta - \int_{S_e} (\hat{T}_x l_x + \hat{T}_y l_y) \phi_i ds = 0, \quad i = 1, \dots, 9. \quad (2-23)$$

In changing the limits of integration we introduce the following relationship

$$dx dy = \det [J] d\xi d\eta. \quad (2-24)$$

Because in our problem the elements are all of the same size, the four integrals appearing in each element in (2-23) are identical for each element. The assembly process, that is, the transformation from element to global integrations, can be easily visualized using Table I which provides us with the relationship between Local Node Numbers and Global Node Numbers.

The assembly procedure now calls for extracting information concerning the integration at the element level from the Table I. From

Element Nodes (Local Node Numbers)	Global Nodes (Global Node Numbers)			
	I	II	III	IV
1	1	2	4	4
2	4	5	7	8
3	5	6	8	9
4	2	3	5	6

Table I Relationship between Local Node Numbers and Global Node Numbers.

column I we can see that global nodes 4 and 5 correspond to element nodes 2 and 3 in element I. In order to find the contribution to the global integral concerning these nodes, we have to create Table II which evaluates the integrals for one element in local coordinates using equation (2-23). From Table II the seeking contribution is found in row 2, column 3, and it is equal to $-1/6$. This value should be placed in matrix location (4,5) of the global matrix. However, this value is not final, because there is also information to be retrieved from element III. This information is located in the position (1,4) of the element matrix of Table II, and it is equals to $-1/6$. This value has to be summed with the previous integral value and the new value should to be placed in the same global matrix position (4,5). Combination of the two integral values yields the final value of $-1/3$, which can be seen in Table III in row 4, column 5.

In general, the element coefficient matrix (Table III) is different for each element because of changes in either element geometry or parameter values. Moreover, it is often necessary to perform the integrations of (2-23) numerically.

i \ j	1	2	3	4
1	2/3	-1/6	-1/3	-1/6
2	-1/6	2/3	-1/6	-1/3
3	-1/3	-1/6	2/3	-1/6
4	-1/6	-1/3	-1/6	2/3

Table II Evaluated Integrals for One Element in Local Coordinates for equation (2-20).

J I	1	2	3	4	5	6	7	8	9
1	2/3	-1/6	0.0	-1/6	-1/3	0.0	0.0	0.0	0.0
2	-1/6	4/3	-1/6	-1/3	-1/3	-1/3	0.0	0.0	0.0
3	0.0	-1/6	2/3	0.0	-1/3	-1/6	0.0	0.0	0.0
4	-1/6	-1/3	0.0	4/3	-1/3	0.0	-1/6	-1/3	0.0
5	-1/3	-1/3	-1/3	-1/3	8/3	-1/3	-1/3	-1/3	-1/3
6	0.0	-1/3	-1/6	0.0	-1/3	4/3	0.0	-1/3	-1/6
7	0.0	0.0	0.0	-1/6	-1/3	0.0	2/3	-1/6	0.0
8	0.0	0.0	0.0	-1/3	-1/3	-1/3	-1/6	4/3	-1/6
9	0.0	0.0	0.0	0.0	-1/3	-1/6	0.0	-1/6	2/3

Table III Evaluated Integrals for the Four Elements of Fig. 2.4
in Global Coordinates for Equation (2-20).

4. Step IV

We now solve the matrix equation (2-23) using Table III as

$$\left[\begin{array}{cccccccccc} 2/3 & -1/6 & 0.0 & -1/6 & -1/3 & 0.0 & 0.0 & 0.0 & 0.0 \\ -1/6 & 4/3 & -1/6 & -1/3 & -1/3 & -1/3 & 0.0 & 0.0 & 0.0 \\ 0.0 & -1/6 & 2/3 & 0.0 & -1/3 & -1/6 & 0.0 & 0.0 & 0.0 \\ -1/6 & -1/3 & 0.0 & 4/3 & -1/3 & 0.0 & -1/6 & -1/3 & 0.0 \\ -1/3 & -1/3 & -1/3 & -1/3 & 8/3 & -1/3 & -1/3 & -1/3 & -1/3 \\ 0.0 & -1/3 & -1/6 & 0.0 & -1/3 & 4/3 & 0.0 & -1/3 & -1/6 \\ 0.0 & 0.0 & 0.0 & -1/6 & -1/3 & 0.0 & 2/3 & -1/6 & 0.0 \\ 0.0 & 0.0 & 0.0 & -1/3 & -1/3 & -1/3 & -1/6 & 4/3 & -1/6 \\ 0.0 & 0.0 & 0.0 & 0.0 & -1/3 & -1/6 & 0.0 & -1/6 & 2/3 \end{array} \right] \begin{matrix} T_1 \\ T_2 \\ T_3 \\ T_4 \\ * T_5 = \\ T_6 \\ T_7 \\ T_8 \\ T_9 \end{matrix}$$

$$\begin{aligned}
& \left[\int_s (\hat{T}_x l_x + \hat{T}_y l_y) \phi_1 ds \right] \\
& \int_s (\hat{T}_x l_x + \hat{T}_y l_y) \phi_2 ds \\
& \int_s (\hat{T}_x l_x + \hat{T}_y l_y) \phi_3 ds \\
& 0.0 \\
& -Q_w \\
& \int_s (\hat{T}_x l_x + \hat{T}_y l_y) \phi_6 ds \\
& 0.0 \\
& 0.0 \\
& \int_s (\hat{T}_x l_x + \hat{T}_y l_y) \phi_9 ds
\end{aligned}$$

(2 - 25)

The line integrals appearing on the right-hand side of (2-25) represent flux boundary conditions. In general, when Dirichlet boundaries are specified, it is necessary to expand and evaluate the line integrals. However, when we use functions, that have continuous derivatives up to the 0th order as bases, one can condense rows containing the known temperature values out of the matrix equation. The reduced matrix equation is

$$[A] * \{b\} = \{f\}, \quad (6 - 26)$$

where

$$[A] = \begin{bmatrix} 4/3 & -1/3 & -1/6 & -1/3 \\ -1/3 & 8/3 & -1/3 & -1/3 \\ -1/6 & -1/3 & 2/3 & -1/6 \\ -1/3 & -1/3 & -1/6 & 4/3 \end{bmatrix}, \quad (6 - 27)$$

$$\{b\} = \begin{bmatrix} T_4 \\ T_5 \\ T_7 \\ T_8 \end{bmatrix}, \quad (6 - 28)$$

$$\{f\} = \begin{bmatrix} 1/2 \\ -Q_w + 5/3 \\ 0.0 \\ 1/2 \end{bmatrix}. \quad (6-29)$$

Solving (2-26) directly we can easily get

$$\begin{bmatrix} T_4 \\ T_5 \\ T_7 \\ T_8 \end{bmatrix} = \begin{bmatrix} 0.783 \\ 0.525 \\ 0.655 \\ 0.783 \end{bmatrix}. \quad (2-30)$$

The coefficients T_4 , T_5 , T_7 , and T_8 represent the values of the temperature at nodes 4, 5, 7, and 8 because the basis functions are defined such that ϕ_i is unity at node i and zero elsewhere.

At the same time the analytical solution for our problem is

$$T = U + V + W, \quad (2-31)$$

where

$$U = \frac{2}{\pi} \sum_{n=0}^{\infty} \frac{\sin[(n+1/2)\pi(\alpha-y)/\alpha] \cosh[(n+1/2)\pi(\alpha-x)/\alpha]}{(n+1/2) \cosh(n+1/2)\pi} \quad (2-32)$$

$$V = \frac{2}{\pi} \sum_{n=0}^{\infty} \frac{\cosh[(n+1/2)\pi y/\alpha] \sin[(n+1/2)\pi x/\alpha]}{(n+1/2) \cosh(n+1/2)\pi} \quad (2-33)$$

$$W = \frac{2}{\pi} \sum_{n=0}^{\infty} \frac{\sin[(n+1/2)\pi x/\alpha] \sin[(n+1/2)\pi \xi/\alpha] \sinh[(n+1/2)\pi(\alpha-y)] \cosh[(n+1/2)\pi \eta/\alpha]}{(n+1/2) \cosh[(n+1/2)\pi]} \quad (2-34)$$

where α is the length of the side of the square (in our case equals to 2), and ξ, η are the x and y locations of the heat source, respectively. The analytical solution yields

$$\begin{bmatrix} T_1 \\ T_2 \\ T_3 \\ T_4 \end{bmatrix} = \begin{bmatrix} 0.756 \\ 0.127 \\ 0.719 \\ 0.756 \end{bmatrix}. \quad (2-35)$$

It is obvious that the numerical solution at the singular point (1,1), which corresponds to the nodal location 5, is not very accurate. This is not odd since we are attempting to represent a rapidly varying function with only four bilinear elements. As we mentioned before the series of (2-1) is inherently capable of representing the exact solution as the number of terms in the series is increased.

III. THE SHALLOW-WATER MODEL AND THE TOPOGRAPHIC ROSSBY WAVE

A. GENERAL

In order to study motions of atmospheric and oceanic relevance, we can use a shallow, rotating layer of homogeneous fluid which is incompressible, and inviscid. This model (Shallow-Water Model) ignores completely the presence of stratification, but experience has shown that it is capable of describing important aspects of atmospheric and oceanic motions. Because of this, it is useful to deal with shallow fluid systems in trying to determine general principles of hydrodynamical behavior of the atmosphere.

The major physical characteristics concerning the shallow-water model, are found to apply well for more complex systems. If we were to analyze the types of wave motions associated with more complex forms of the primitive atmospheric equations, (e.g., with vertical stratification, compressibility, etc.), we would find essentially the same types, namely gravity-inertia waves and Rossby waves, and deep and shallow motions would exist simultaneously.

B. THE SHALLOW-WATER MODEL

Let us consider a sheet of fluid with constant and uniform density as illustrated in Fig. 3.1. The height of the surface of the fluid is given by

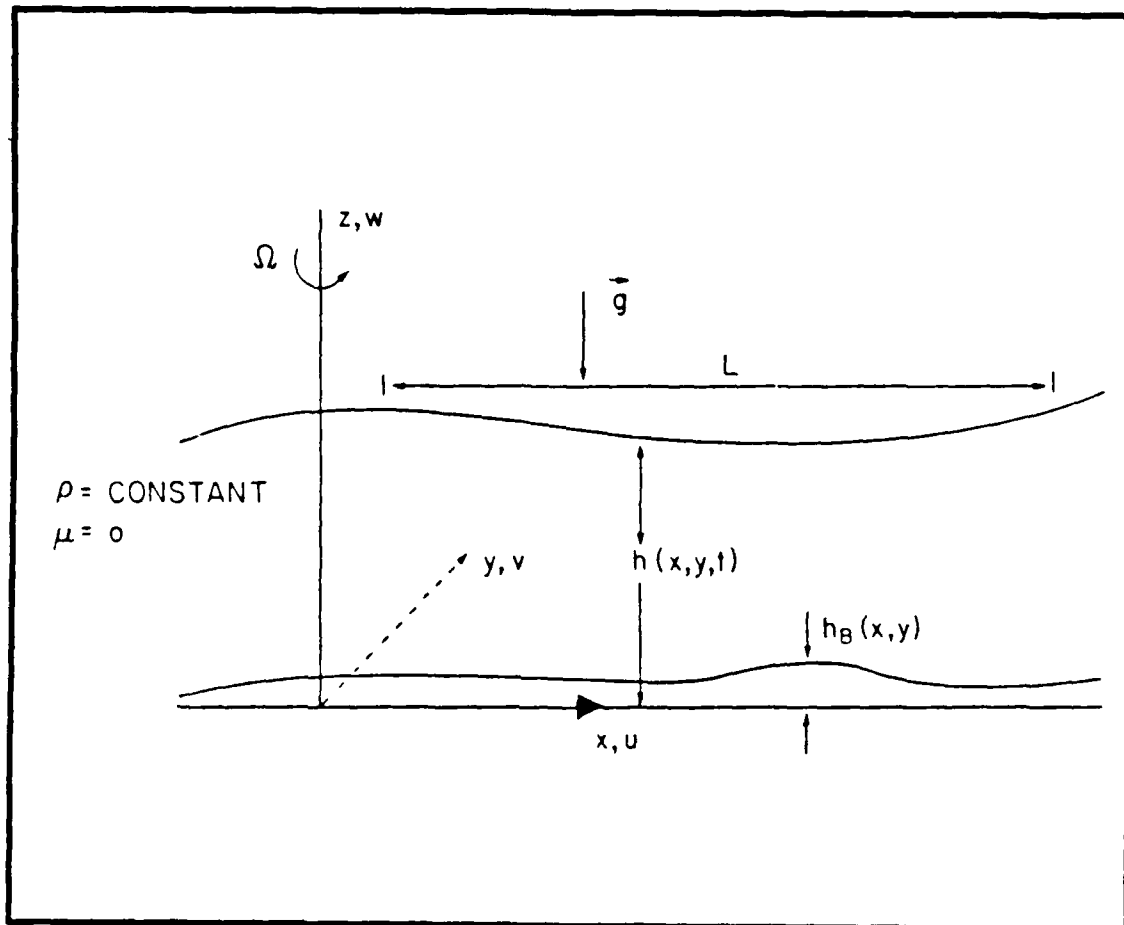


Fig. 3.1 The Shallow-Water Model.

$h(x, y, t)$. We also model the body force arising from the potential ϕ as a vector, g , normal to the $z = 0$ surface. The z -axis coincides with the rotation axis of the fluid, so that in this particular case the Coriolis parameter f is simply given by 2Ω . The rigid bottom topography is defined by the surface $z = h_B(x, y)$, which is not a function of time (t). Finally, we assume that the fluid is inviscid ($\mu=0$), that is, only motions for which viscosity is unimportant are considered.

Also we suppose that a characteristic value for the depth can be sensibly chosen, say D , and D also characterizes the vertical scale of the motion as well. In the same way we consider that a characteristic horizontal length scale for the motion exists, which we call L . The fundamental relationship which characterizes the shallow-water theory is given by

$$\delta = \frac{D}{L} \ll 1. \quad (3 - 1)$$

Here, it is important to note that the fluid is rotating, so that Coriolis accelerations can be important. The fluid layer is flat rather than forming a spherical shell, and its major physical deficiency as mentioned above is the absence of the density stratification which is present in the real atmosphere.

C. SMALL-AMPLITUDE MOTIONS

Dealing with the Shallow-Water Model, and since by hypothesis $\delta \ll 1$, we are able to express the hydrostatic approximation in the following form:

$$\frac{\partial p}{\partial z} = -\rho g. \quad (3-2)$$

We can integrate equation (3.2) resulting in

$$p = -\rho g z + A(x, y, t). \quad (3-3)$$

Applying now the obvious boundary condition

$$p(x, y, h) = p_0, \quad (3-4)$$

where p_0 is a constant, we can easily get

$$p = \rho g (h - z) + p_0. \quad (3-5)$$

At this stage, we can clearly see that the horizontal pressure gradient is independent of z , i.e.

$$\frac{\partial p}{\partial x} = \rho g \frac{\partial h}{\partial x}, \quad (3-6)$$

$$\frac{\partial p}{\partial y} = \rho g \frac{\partial h}{\partial y}, \quad (3-7)$$

in such way that the horizontal accelerations must be independent of z . That is why we can also assume that the horizontal velocities themselves remain independent of z , if they are so initially. Applying now the Taylor-Proudman theorem we are able to write the horizontal momentum equation as

$$\frac{\partial u}{\partial t} + u \frac{\partial u}{\partial x} + v \frac{\partial u}{\partial y} - fv = - g \frac{\partial h}{\partial x}, \quad (3-8)$$

$$\frac{\partial v}{\partial t} + u \frac{\partial v}{\partial x} + v \frac{\partial v}{\partial y} + fu = - g \frac{\partial h}{\partial y}. \quad (3-9)$$

The specification of incompressibility for the Shallow-Water Model, decouples the dynamics from the thermodynamics and reduces the equation of mass conservation to the condition of incompressibility given in the following form:

$$\frac{\partial u}{\partial x} + \frac{\partial v}{\partial y} + \frac{\partial w}{\partial z} = 0. \quad (3-10)$$

Having in mind that u and v are independent of z , equation (3-10) can be integrated in z as

$$w(x,y,t) = -z\left(\frac{\partial u}{\partial x} + \frac{\partial v}{\partial y}\right) + \tilde{\omega}(x,y,t). \quad (3-11)$$

Equation (3-11) can be further manipulated using the condition of no normal flow at the rigid surface $z = h_B$ resulting in

$$\frac{\partial h}{\partial t} + \frac{\partial}{\partial x} \{(h - h_B)u\} + \frac{\partial}{\partial y} \{(h - h_B)v\} = 0. \quad (3-12)$$

If we now consider the total depth (H) is given by

$$H = h - h_B, \quad (3-13)$$

then the equation of mass conservation (3-12) becomes

$$\frac{\partial H}{\partial t} + \frac{\partial}{\partial x} (uH) + \frac{\partial}{\partial y} (vH) = 0. \quad (3-15)$$

Our next step now should be to linearize the set of equations (3-8), (3-9), and (3-15), by studying small-amplitude motions. This is very important because the presence of solutions representing free oscillations often demonstrates fundamental mechanisms which occur in more complicated situations as we mentioned before.

Let us now consider the thickness of the fluid layer in absence of motion to be given as

$$H(x,y,t) = H_0(x,y) + \eta(x,y,t), \quad (3 - 16)$$

where $\eta \ll H_0$. Furthermore

$$\frac{\partial u_H}{\partial t} \gg u_H \cdot \nabla u_H, \quad (3 - 17)$$

or in other words u and v are considered small enough. Linearizing now the equations (3-8), (3-9), and (3-15), we can obtain

$$\frac{\partial u}{\partial t} - fv = -g \frac{\partial \eta}{\partial x}, \quad (3 - 18)$$

$$\frac{\partial v}{\partial t} + fu = -g \frac{\partial \eta}{\partial y}, \quad (3 - 19)$$

$$\frac{\partial \eta}{\partial t} + \frac{\partial}{\partial x} (uH_0) + \frac{\partial}{\partial y} (vH_0) = 0, \quad (3 - 20)$$

where all the quadratic terms in the dynamical variables u , v , η with respect to the linear terms are ignored. If we now define the linearized mass flux vector given by

$$\mathbf{U} = iU + jV, \quad (3 - 21)$$

where

$$U = u H_0, \quad (3-22)$$

$$V = v H_0, \quad (3-23)$$

equations (3-18), (3-19), and (3-20) become

$$\frac{\partial U}{\partial t} - fV = -gH_0 \frac{\partial \eta}{\partial x}, \quad (3-24)$$

$$\frac{\partial V}{\partial t} + fU = -gH_0 \frac{\partial \eta}{\partial y}, \quad (3-25)$$

$$\frac{\partial \eta}{\partial t} + \frac{\partial U}{\partial x} + \frac{\partial V}{\partial y} = 0. \quad (3-26)$$

At this point it is possible for us to obtain an equation in the single variable η as

$$\frac{\partial}{\partial t} \left[\left(\frac{\partial^2}{\partial t^2} + f^2 \right) \eta - \nabla \cdot (C_0^2 \nabla \eta) \right] - g f J(H_0, \eta) = 0, \quad (3-27)$$

where

$$C_0^2 = g H_0, \quad (3-28)$$

$$J(H_0, \eta) = \frac{\partial H_0}{\partial x} \frac{\partial \eta}{\partial y} - \frac{\partial H_0}{\partial y} \frac{\partial \eta}{\partial x}. \quad (3 - 29)$$

It can be seen that the Jacobian term is the effect of the geostrophic wind blowing across isobaths. For low frequency motion and small variation in H_0 , the first term in (3-27) represents the time rate of change of the quasigeostrophic vorticity. The motion that results from this kind of balance is a topographic Rossby wave which we examine in more detail in the next sections. The velocities components u and v can be also found in terms of η , given as

$$\left(\frac{\partial^2}{\partial t^2} + f^2 \right) u = -g \left(\frac{\partial^2 \eta}{\partial x \partial t} + f \frac{\partial \eta}{\partial y} \right), \quad (3 - 30)$$

$$\left(\frac{\partial^2}{\partial t^2} + f^2 \right) v = -g \left(\frac{\partial^2 \eta}{\partial y \partial t} - f \frac{\partial \eta}{\partial x} \right). \quad (3 - 31)$$

D. THE TOPOGRAPHIC ROSSBY WAVE

Following Pedlosky (1987), let us consider that H_0 in equation (3-27) varies slightly in the y -direction given by

$$H_0 = D - D s \frac{y}{L}, \quad (3 - 32)$$

where D is a constant,

s is the slope of H_0 in the y -direction, and

L is the width of the channel.

In this particular case (Fig. 3.2), pure geostrophic motion is possible only if v is zero. Also, lines of constant H_0 are parallel to the x -axis. Motion across the isobaths of fluid columns will cause them to stretch or contract. Therefore, there is a possibility of a different mode of motion to exist depending on the combined effect of rotation and bottom slope.

Assuming

$$s \ll 1, \quad (3 - 33)$$

and η to be of the following form

$$\eta = \text{Re} \{ \eta^*(y) \exp[i(kx - \sigma t)] \}, \quad (3 - 34)$$

substitution in (3-27) yields

$$(1 - s \frac{y}{L}) \frac{d^2 \eta^*}{dy^2} - \frac{s}{L} \frac{d\eta^*}{dy} + \eta^* \left[\frac{\sigma^2 - f^2}{g D} - k^2 \left(1 - s \frac{y}{L}\right) - \frac{f s}{L \sigma} k \right] = 0, \quad (3 - 35)$$

with the following boundary conditions:

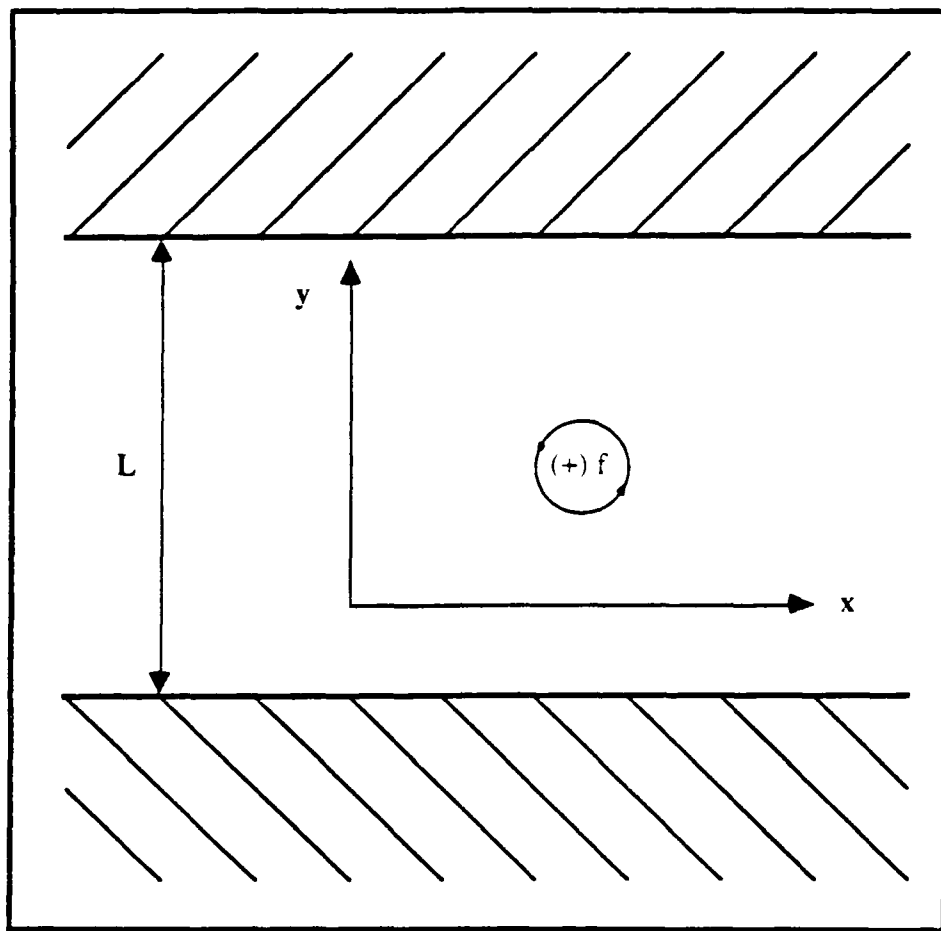


Fig. 3.2 The infinite channel of width L , rotating with angular velocity $f/2$.

$$\frac{d\eta^*}{dy} + \frac{fk}{\sigma} \eta^* = 0, \quad (3 - 36)$$

on $y = 0, L$.

If we now assume that

$$(1 - s \frac{y}{L}) \approx 1, \quad (3 - 37)$$

which appears to be a very realistic approximation, then (3-35) becomes

$$\frac{d^2\eta^*}{dy^2} - \frac{s}{L} \frac{d\eta^*}{dy} + [\frac{\sigma^2 - f^2}{C_0^2} - k^2 - \frac{f}{L} \frac{s}{\sigma} k] \eta^* = 0. \quad (3 - 38)$$

Here only in terms where s can be compared with quantities of order unity has it been neglected. Solving (3-38) we can get

$$\eta^* = \exp(\frac{sy}{2L}) [A \sin(ay) + B \cos(ay)], \quad (3 - 39)$$

where a is given by

$$a = \sqrt{\frac{\sigma^2 - f^2}{C_0^2} - (k^2 + \frac{s^2}{4L^2}) - \frac{fks}{\sigma L}}. \quad (3 - 40)$$

Applying now the boundary conditions given by (3-36) we can get the following eigenvalue problem

$$(\sigma^2 - f^2)(\sigma^2 - k^2 C_0^2) \sin(aL) = 0. \quad (3-41)$$

It is obvious, that to the lowest order in s , the slope does not alter the Kelvin mode (that is, because the factors multiplying $\sin(aL)$ are the same as for the case of a flat bottom). The roots corresponding to the zeros of $\sin(aL)$ are given by

$$\sigma^2 - \frac{fksC_0^2}{L\sigma} - C_0^2 \left(k^2 + \frac{n^2\pi^2}{L^2} + \frac{f^2}{C_0^2} \right) = 0. \quad (3-42)$$

There are two separate classes of solutions to (3-42)

a. The first class has frequencies each of which exceeds f . In this class the term in s is negligible, and to $O(s)$ we obtain the Poincare modes, i.e.,

$$\sigma^2 = f^2 + C_0^2 \left(k^2 + \frac{n^2\pi^2}{L^2} \right) + O(s), \quad n = 1, 2, \dots \quad (3-43)$$

Equation (3-43) shows that the high-frequency Poincare waves are also essentially unaffected by the small bottom slope.

b. The class having frequencies $\sigma = O(s)$, for which the first term in (3-42) is negligible, while the second is of $O(1)$.

The other solution leads us to the dispersion relation for the topographic Rossby wave, i.e.,

$$\sigma = -s \left(\frac{f}{L}\right) \frac{k}{k^2 + \frac{n^2\pi^2}{L^2} + \frac{f^2}{C_0^2}}, \quad n = 1, 2, \dots, \quad (3-44)$$

obtained by neglecting the first term of (3-41).

The maximum Rossby-wave frequency should be given by setting

$$k = k_n = \left(\frac{n^2\pi^2}{L^2} + \frac{f^2}{C_0^2} \right)^{1/2}, \quad (3-45)$$

for which we get

$$\sigma = \sigma_{\max} = -\frac{s}{2} \frac{f}{\left[n^2\pi^2 + \frac{f^2 L^2}{C_0^2} \right]^{1/2}}. \quad (3-46)$$

From equation (3-46) it is clearly seen that the Rossby-wave frequency is always less than f . Another important feature of the Rossby wave is that its phase speed in the x -direction, which is given by

$$C_x = \frac{\sigma}{k} = - \frac{\frac{sf}{L}}{\frac{k^2 + \frac{n^2\pi^2}{L^2} + \frac{f^2}{C_0^2}}{L^2}}, \quad (3-47)$$

is negative for $s > 0$, and positive for $s < 0$. Therefore, the wave propagates (in the Northern Hemisphere) parallel to the topography, with the shallowest water on its right. Also, for high wave number, i.e., small scale, the frequency σ decreases with increasing wave number as shown in Fig. 3.3.

The dynamical fields for the Rossby-wave to lowest order are given by

$$\eta = \eta_0 \sin\left(\frac{n\pi y}{L}\right) \cos(kx - \sigma t + \phi) + O(s), \quad (3-48)$$

$$u = - \frac{g}{f} \frac{n\pi}{L} \eta_0 \cos\left(\frac{n\pi y}{L}\right) \cos(kx - \sigma t + \phi) + O(s), \quad (3-49)$$

$$v = - \frac{g}{f} k \eta_0 \sin\left(\frac{n\pi y}{L}\right) \sin(kx - \sigma t + \phi) + O(s), \quad (3-50)$$

where small terms of $O(s)$ have been neglected consistently.

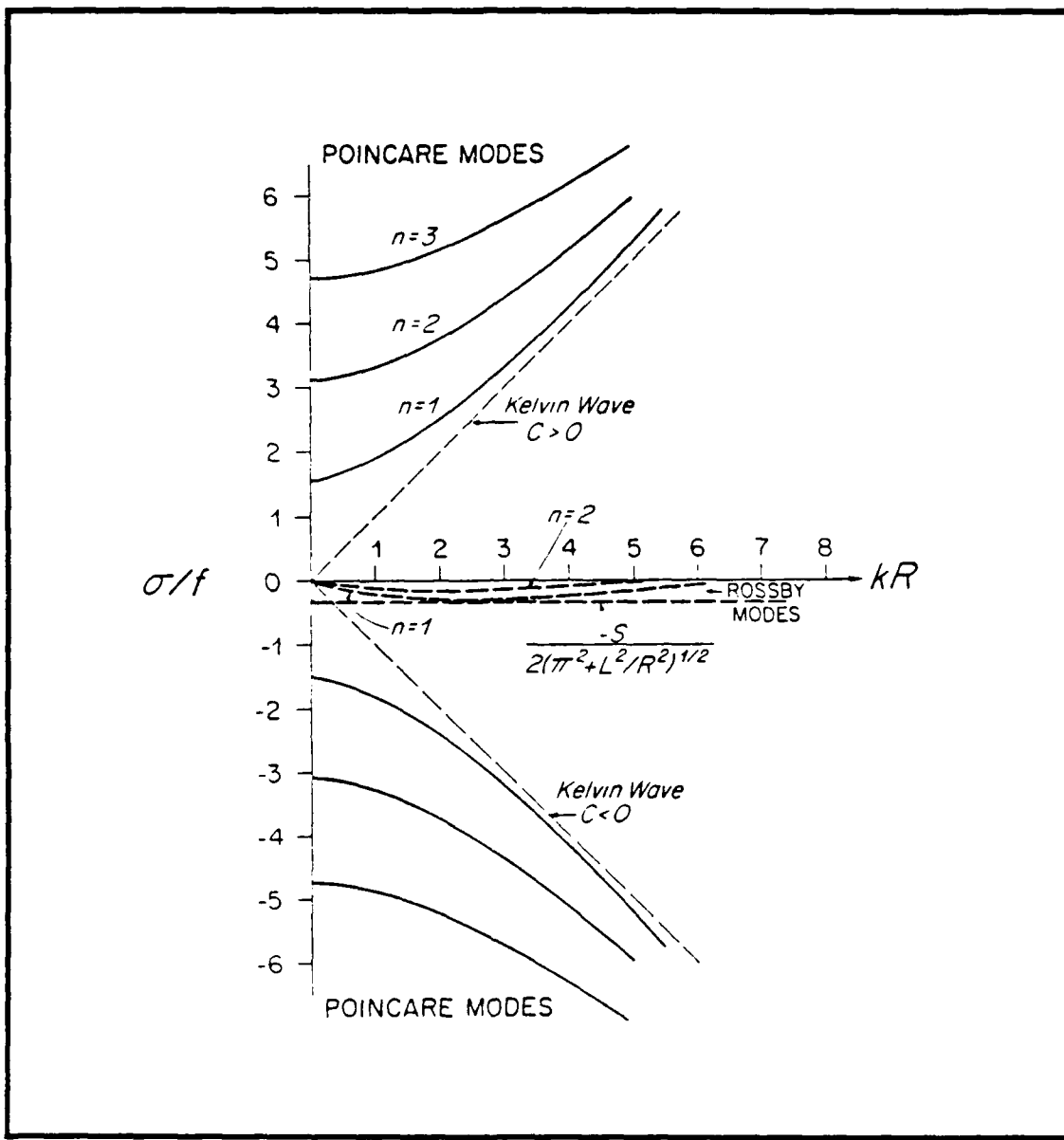


Fig. 3.3 A schematic representation of the dispersion diagram for Poincare, Kelvin, and topographic Rossby waves in a channel.

From equations (3-48), (3-49), and (3-50), it follows that to lowest order in s , and therefore σ/f , the fields of motion in the Rossby wave satisfy

$$u = -\frac{g}{f} \frac{\partial \eta}{\partial y}, \quad (3-51)$$

$$v = \frac{g}{f} \frac{\partial \eta}{\partial x}, \quad (3-52)$$

which are the time-independent forms of (3-31) and (3-32). Because of the close relationship between η , and the pressure field, equations (3-51) and (3-52) represent the geostrophic relation for the horizontal motions.

At this stage, it is clearly seen that to lowest order in σ/f , which plays the role of the Rossby number here, the velocity fields, though changing with time, remain continuously in geostrophic balance with the pressure field. However, the flow is not exactly geostrophic, for then the flow would be restricted to travel parallel to the isobaths, i.e., v would vanish. Even though the velocity fields are geostrophic to lowest order, it is the very small departures from geostrophy that give rise to the wave. It is the small cross-isobath flow, which is a nongeostrophic effect, which produces the oscillation. The Rossby-wave, whose existence requires both s and f to be non zero, is a low-frequency wave oscillation; its period is greater than a rotation period.

IV. HYDRAULIC JUMPS IN ROTATING AND NONROTATING SYSTEMS

A. GENERAL

A strong and relatively warm wind known as chinook occurs from time to time in areas along the eastern slope of the Rocky Mountains. Similar phenomena are often observed in the Owens valley on the eastern side of the Sierra Nevada. Also cold fronts, approaching the area of Alps, moving from north or west, many times undergo severe deformation. This deformation may result in a number of important weather events including blocking and splitting of air flow on the upstream side or even triggering of lee cyclogenesis in the downstream flow.

Tepper (1952) has proposed that squall lines are modified hydraulic jumps, but the idea that there is a certain link between downslope winds and hydraulic jumps was proposed by Long (1953). Long suggested that the mechanism that produces the hydraulic jump may be similar to one that produces strong waves and downslope winds in the atmosphere. Houghton and Kasahara (1968) have also proposed other mesoscale hydraulic analogies. Williams and Hori (1970) observed a delay in the formation of hydraulic jumps in case the Rossby number was less than 0.1 in a rotating system.

However, it has been difficult to confirm this hypothesis about jump formation, because there are significant differences between the atmosphere

and the simple fluid systems used in the hydraulic theory. One of the major reasons for this uncertainty appears to be the vertical propagation of the wave energy, which may occur in the real atmosphere but not in fluids bounded by a rigid or a free surface.

B. HYDRAULIC JUMPS IN A NONROTATING SYSTEM

Let us first consider the one-dimensional Shallow-Water Model. Let us also consider a mean flow over an isolated rigid orographic ridge as shown in Fig. 4.1. The horizontal momentum equation is given by

$$\frac{\partial u}{\partial t} + u \frac{\partial u}{\partial x} + g \frac{\partial}{\partial x} (h + h_M) = 0. \quad (4 - 1)$$

The continuity equation also, is given by

$$\frac{\partial h}{\partial t} + u \frac{\partial h}{\partial x} + h \frac{\partial u}{\partial x} = 0, \quad (4 - 2)$$

where h denotes the depth of the fluid, and

h_M is the height of the rigid ridge, which is a function of x .

At time $t = 0$, the fluid is set in motion from rest so that for infinite x , it has a constant zonal flow u_0 . After sufficient time has elapsed, the solution in the neighborhood of the rigid ridge would be given by the steady state solutions of equations (4-1) and (4-2).

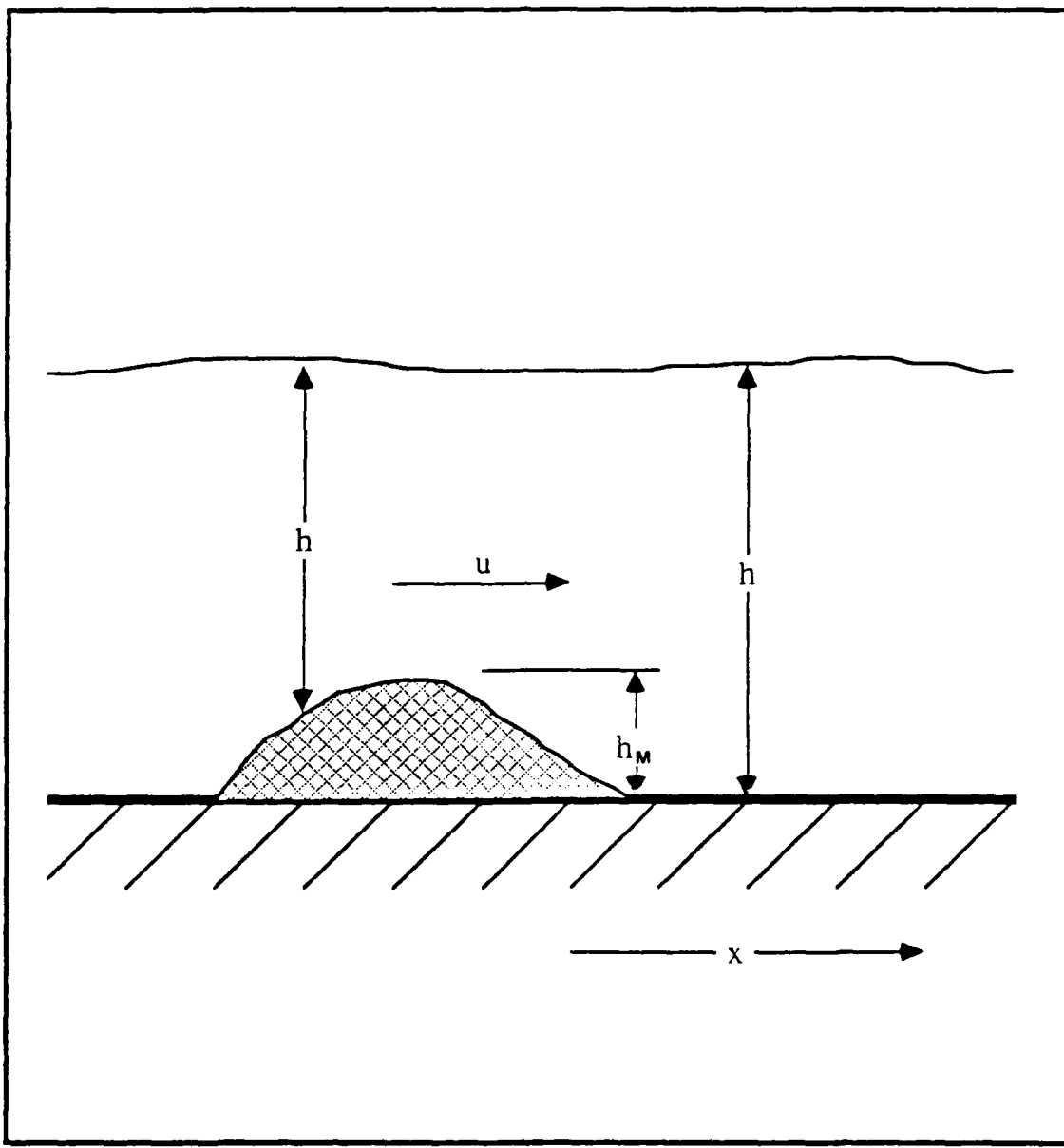


Fig. 4.1 A cross section view of the one-dimensional Shallow-Water Model with a mean flow u .

Following Houghton and Kasahara (1968), the steady state solutions for the variables u and h are given by

$$u^2 + 2gh + 2gh_M = C_1, \quad (4 - 3)$$

$$hu = C_2, \quad (4 - 4)$$

where C_1 and C_2 are constants. If a flow without a hydraulic jump is considered, both C_1 and C_2 are determined by the velocity u_0 , and the height h_0 of the flow in the region far from the ridge, so that

$$C_1 = u_0^2 + 2gh_0, \quad (4 - 5)$$

$$C_2 = h_0u_0. \quad (4 - 6)$$

At this stage we define the following dimensionless parameters F_0 , F , R , and U^* as

$$F_0 = \frac{u_0}{\sqrt{gh_0}}, \quad (4 - 7)$$

$$F^2 = \frac{F_0^2}{2} + 1, \quad (4 - 8)$$

$$R = \frac{h_M}{h_0}, \quad (4-9)$$

$$U_* = \frac{u}{u_0}. \quad (4-10)$$

If we eliminate h from equation (4-3) by using equation (4-4), we are able to obtain

$$(F^2 - 1) U_*^3 + (R - F^2) U_* + 1 = 0. \quad (4-11)$$

Assuming that the mean flow u_0 is always positive, then $F > 1$. Dividing equation (4-11) by $(F^2 - 1)$ we can get

$$U_*^3 + \frac{R - F^2}{F^2 - 1} U_* + \frac{1}{F^2 - 1} = 0. \quad (4-12)$$

Equation (4-12) is a very important relation among the variables U_* , R , and F . We can easily plot the solution U_* to equation (4-12) for given values of F^2 . For instance if F^2 equals to 1.02 ($F_0 = 0.2$), equation (4-12) becomes

$$U_*^3 + (50R - 51) U_* + 50 = 0. \quad (4-13)$$

We can consider equation (4-13) as determining the values of R that are possible with a given value of U_* , as shown in Fig. 4.2. It is interesting here to note the singular behavior near $R = 0$. In case of $F = 1.125$ ($F_0 = 0.5$), equation (4-12) becomes

$$U_*^3 + (8R - 9) U_* + 8 = 0, \quad (4 - 14)$$

which leads to Fig. 4.3. Also, if $F = 3.0$ ($F_0 = 2.0$), equation (4-12) can be written in the following simple form

$$U_*^3 + (0.5R - 1.5) U_* + 0.5 = 0, \quad (4 - 15)$$

which gives Fig. 4.4.

It is very important here to note, that if R has values lower than $R_{critical}$, where $R_{critical}$ is given by

$$R_{critical} = F^2 - 1.8899 (F^2 - 1)^{1/3}, \quad (4 - 16)$$

then three real roots exist, as we clearly see in Figs. 4.2, 4.3, and 4.4. In the case where R is greater than $R_{critical}$, no physically meaningful solution exists (no real roots). In other words, in this particular case we expect the occurrence of a hydraulic jump.

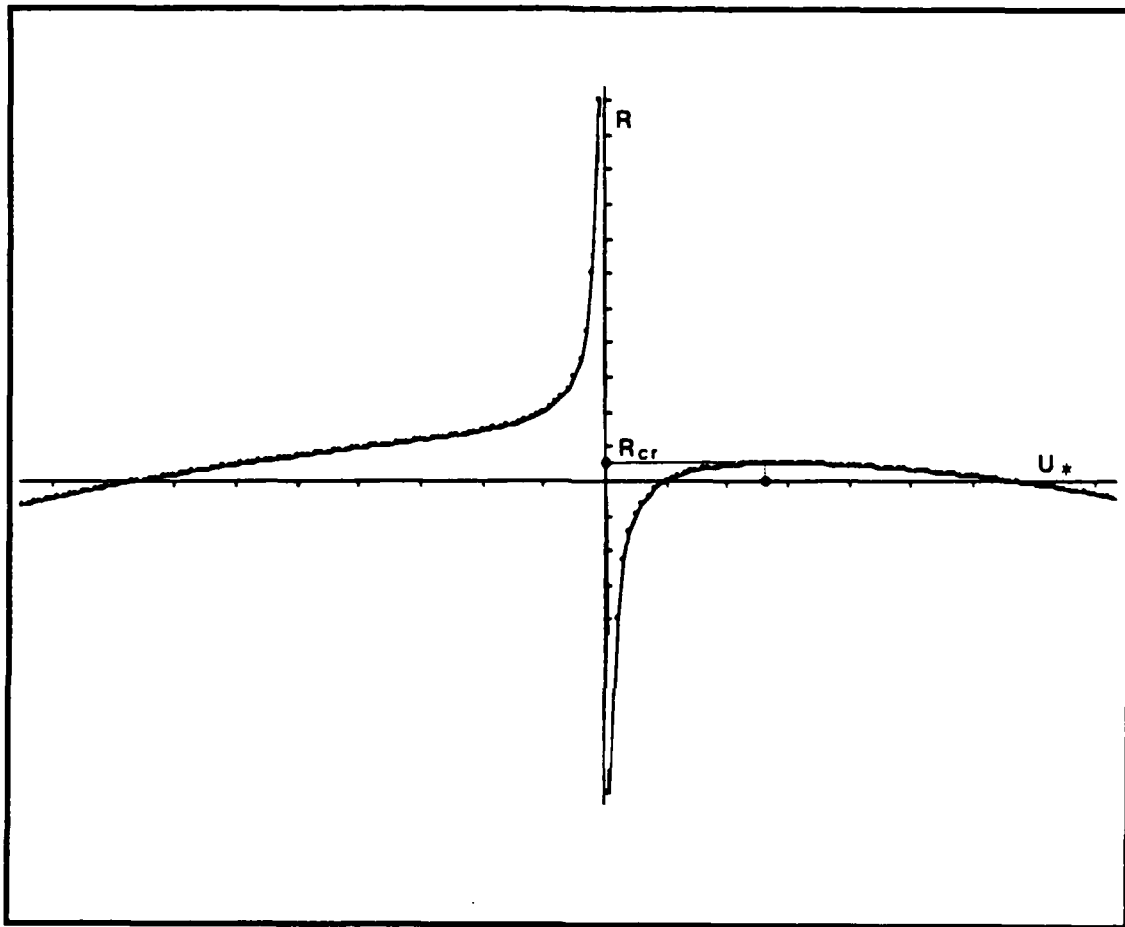


Fig. 4.2 Parameter R as a function of solution U_* , as given by equation (4-12) for $F^2 = 1.02$.

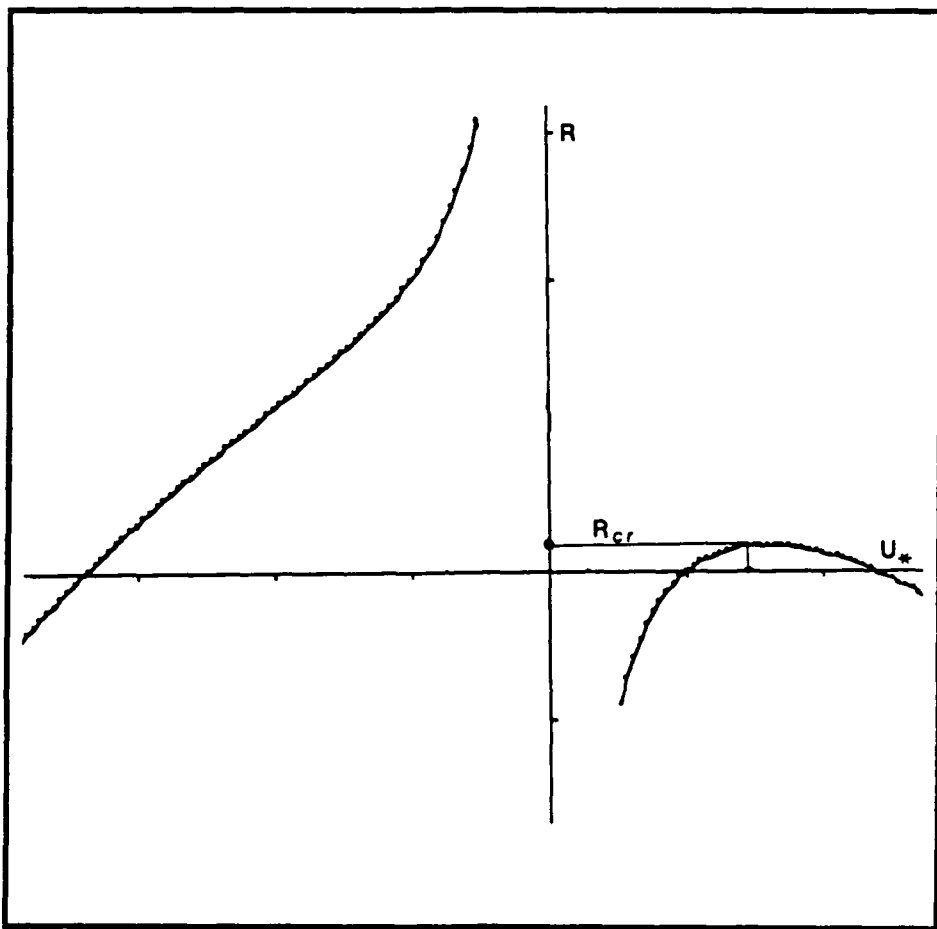


Fig. 4.3 As in Fig. 4.2, except for $F^2 = 1.125$.

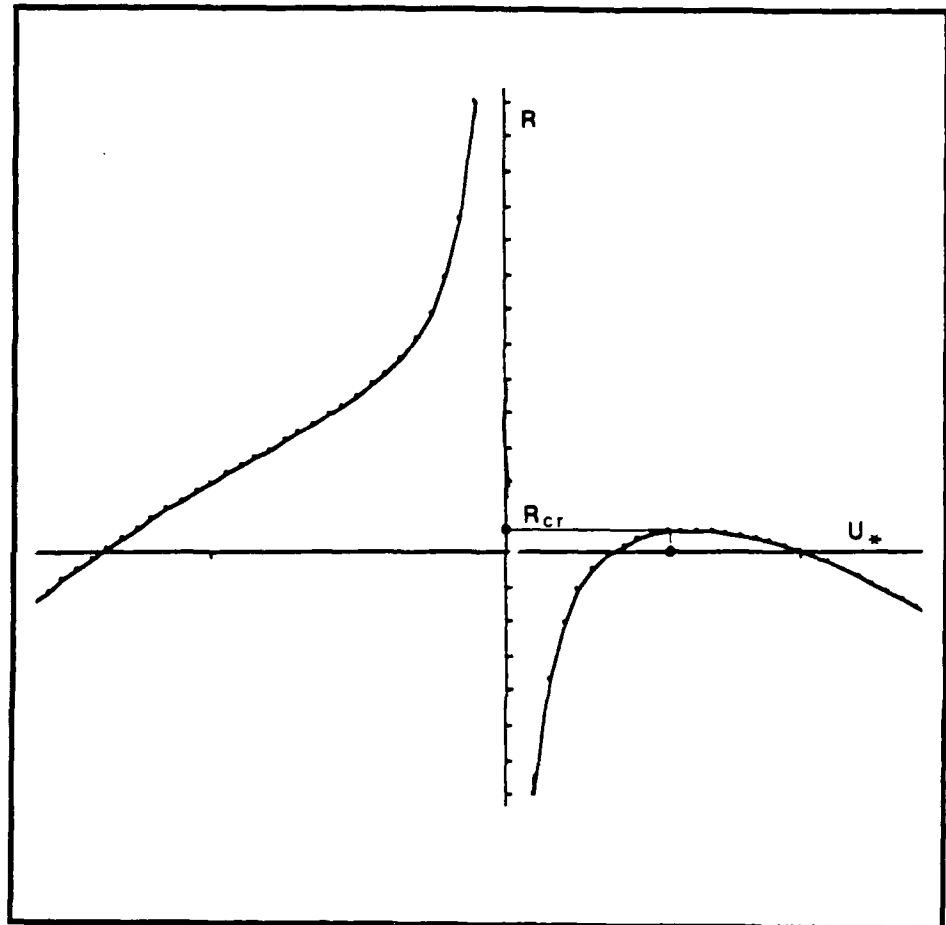


Fig. 4.4 As in Fig. 4.2, except for $F^2 = 3.0$.

If we plot equation (4-16), as shown in Fig. 4.5, we are able to find three distinct domains. In both domains I and III, the parameter R (function of x), has values lower than $R_{critical}$. In this case, a real solution of equation (4-16) there exists, which is physically meaningful. On the other hand in domain II, the parameter R is greater than $R_{critical}$, so no physical solution exists.

C. HYDRAULIC JUMPS IN A ROTATING SYSTEM

Although none of the numerical experiments concerning hydraulic jumps (results section), involves rotation, it is useful to explore the particular effects of rotation on the formation of hydraulic jumps. The basic equations for a homogeneous, one-layer, inviscid fluid (Williams and Hori, 1970), are given by

$$\frac{\partial u}{\partial t} + u \frac{\partial u}{\partial x} + g \frac{\partial h}{\partial x} - fv = 0, \quad (4 - 17)$$

$$\frac{\partial v}{\partial t} + u \frac{\partial v}{\partial x} + fu = 0, \quad (4 - 18)$$

$$\frac{\partial h}{\partial t} + u \frac{\partial h}{\partial x} + h \frac{\partial u}{\partial x} = 0, \quad (4 - 19)$$

where h is the depth of the fluid.

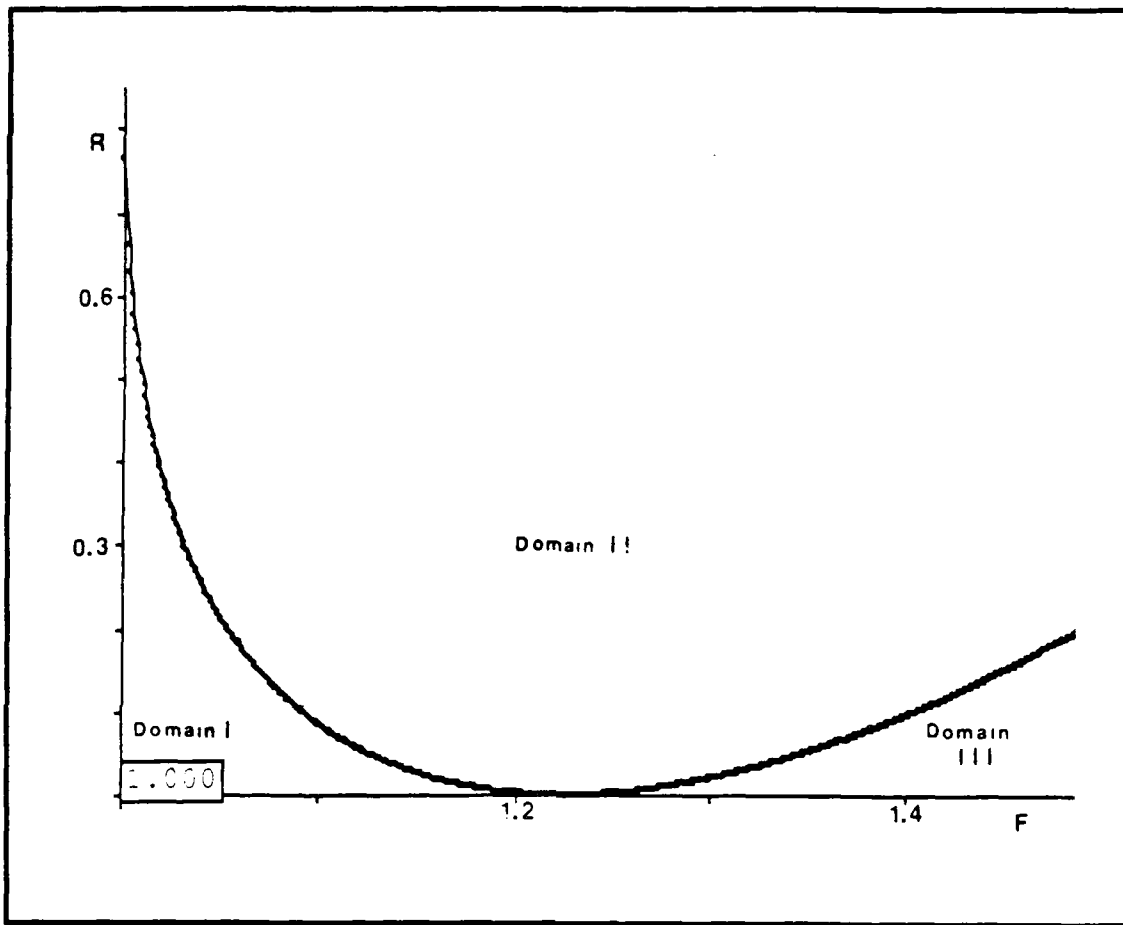


Fig. 4.5 Classification of asymptotic flow conditions as a function of the maximum height of the topographic ridge, R_{critical} , and initial flow speed parameter F .

We perform a scale analysis by expressing the independent variables as

$$t = T t', \quad (4 - 20)$$

$$x = L x'. \quad (4 - 21)$$

The dependent variables are also broken up and scaled as

$$u = U u', \quad (4 - 22)$$

$$v = V v', \quad (4 - 23)$$

$$h = h_m + \sqrt{\frac{h_m}{g}} h', \quad (4 - 24)$$

where h_m represents the mean depth of the fluid. Also, the Rossby number and the Froude number are defined as

$$R_0 = \frac{U}{f L} \quad (4 - 25)$$

and

$$F_0 = \frac{U}{(gh_m)^{1/2}}. \quad (4 - 26)$$

In order to include the results obtained by the previous analysis which are valid for a nonrotating system, we examine the case where $F_0 \leq 1$ and $F_0 \leq R_0$. The appropriate time scale for doing this is

$$T = \frac{L}{(gh_m)^{1/2}}, \quad (4 - 27)$$

and the appropriate v scale

$$V = \frac{F_0}{R_0} U. \quad (4 - 28)$$

The nondimensional equations for this case are given by

$$\frac{\partial u'}{\partial t'} + F_0 u' \frac{\partial u'}{\partial x'} + \frac{\partial h'}{\partial x'} - \frac{F_0^2}{R_0^2} v' = 0, \quad (4 - 29)$$

$$\frac{\partial v'}{\partial t'} + F_0 u' \frac{\partial v'}{\partial x'} + u' = 0, \quad (4 - 30)$$

$$\frac{\partial h'}{\partial t'} + F_0 (u' \frac{\partial h'}{\partial x'} + h' \frac{\partial u'}{\partial x'}) + \frac{\partial u'}{\partial x'} = 0. \quad (4 - 31)$$

It is obvious that hydraulic jumps can be formed through the action of the nonlinear terms in equations (4-29) and (4-31). Even when F_0 is small ($\ll 1$), they can produce a jump in a nonrotating system. If the Coriolis

term in equation (4-29) dominates then a hydraulic jump may be prevented.

This implies that

$$\frac{F_0^2}{R_0^2} \gg F. \quad (4 - 32)$$

The form of the curve dividing the jump region from the nonjump region should be given by

$$F_0 = A R_0^2, \quad (4 - 33)$$

where A is a constant. The numerical solutions show that the range for A is from 6.0 to 7.5, which appears to be in agreement with Houghton's analytical curve corresponding to $A = 6.5$. For $F_0 \sim 1$, the above scale analysis does not apply, since F_0 is then greater than R_0 .

When both $F_0 \sim 1$, and $R_0 \sim 1$, all terms in the equations (4-29), (4-30), and (4-31) are of the same order. In this case, jumps are expected to form. On the other hand, if $R_0 \ll 1$, the proper time scale is $1/f$, while the proper v scale should be $V = U$. The nondimensional equations can be then rewritten as

$$\frac{\partial u'}{\partial t'} + R_0[u' \frac{\partial u'}{\partial x'} + \frac{1}{F_0} \frac{\partial h'}{\partial x'}] - v' = 0, \quad (4 - 34)$$

$$\frac{\partial v'}{\partial t'} + R_0 u' \frac{\partial v'}{\partial x'} + u' = 0, \quad (4 - 35)$$

$$\frac{\partial u'}{\partial t'} + R_0 [u' \frac{\partial u'}{\partial x'} + h' \frac{\partial u'}{\partial x'} + \frac{1}{F_0} \frac{\partial u'}{\partial x'}] = 0. \quad (4 - 36)$$

If we now neglect all terms in R_0 , the resulting equations describe an inertial oscillation in u and v . We do not expect a hydraulic jump to form in this case except perhaps after a very long time.

V. MODEL DESCRIPTION

A. GENERAL

There are two possible choices of increasing resolution, where desired or required, concerning a triangular subdivision. We can use near-equilateral triangles (Cullen, 1974b) or equilateral triangles (Hinsman, 1975). Both have the advantage of almost perfect wave propagation characteristics. For the same problem we can also use rectangular subdivisions, although it is not obvious which subdivision is most suitable. However, a major advantage of the rectangular subdivision (shown in Fig. 5.1) is that it allows algorithms to be developed which take full advantage of vector processors. The interesting point here is that the Galerkin method has to utilize efficient numerical techniques to be considered as a viable option for numerical weather prediction.

There are several solution procedures available for the Galerkin method. No particular attempt is made to optimize computational efficiency in this research model. A direct solver is employed using a Gaussian elimination procedure. The matrices from the Galerkin procedure are decomposed into upper and lower block tri-diagonal matrices. A preprocessing, representing the forward substitution stage, can be done once. Any time a solution is desired, a back substitution has to be performed. That is why the required coefficients for the backward step must be stored in a very efficient manner. This particular algorithm

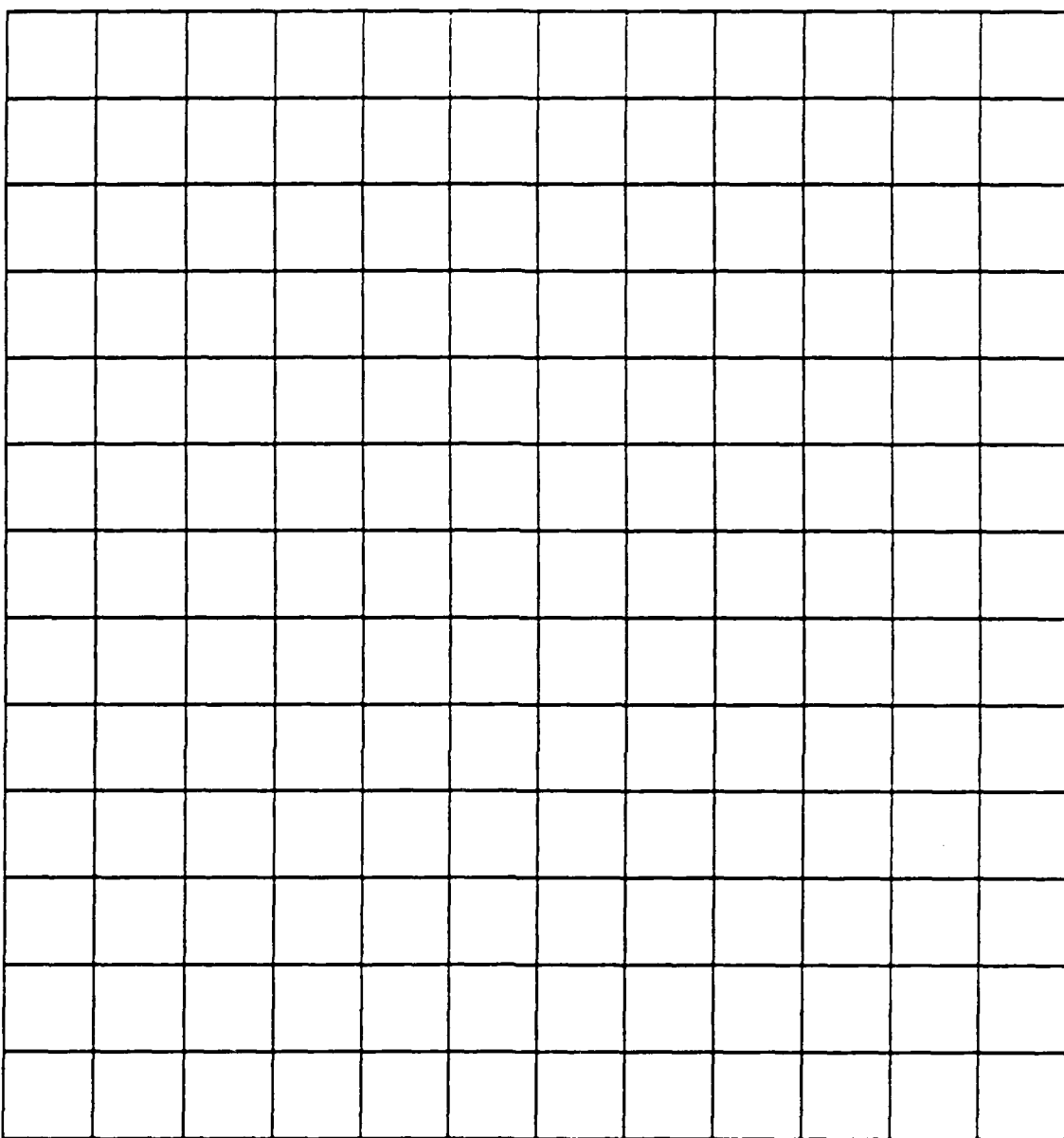


Fig. 5.1 Rectangular uniform subdivision for a channel in
Cartesian coordinates.

represents a 'skyline' solver, referring to the compact method of storing only those coefficients required. This method has both the desired level of accuracy and a high degree of computational efficiency.

B. EQUATION FORMULATION

In order to integrate the equations governing the free-surface height and velocity of an inviscid hydrostatic incompressible fluid we can write

$$\frac{\partial \phi}{\partial t} + u \frac{\partial \phi}{\partial x} + v \frac{\partial \phi}{\partial y} + \phi \left(\frac{\partial u}{\partial x} + \frac{\partial v}{\partial y} \right) = 0 \quad (5-1)$$

$$\frac{\partial u}{\partial t} + u \frac{\partial u}{\partial x} + v \frac{\partial u}{\partial y} - fv + \frac{\partial \phi}{\partial x} = 0 \quad (5-2)$$

$$\frac{\partial v}{\partial t} + u \frac{\partial v}{\partial x} + v \frac{\partial v}{\partial y} + fu + \frac{\partial \phi}{\partial y} = 0 \quad (5-3)$$

where ϕ is the geopotential height,

u is the east/west component of the wind,

v is the north/south component of the wind, and

f is the coriolis parameter.

We now assume that the geopotential height ϕ , in absence of motion is Φ . Then, in general

$$\phi(x, y, t) = \Phi(x, y) + \phi'(x, y, t), \quad (5 - 4)$$

where Φ is the mean, and

ϕ' is a perturbation from the mean. The governing equations now can be written

$$\phi'_t + \Phi D + (u\phi')_x + (v\phi')_y = 0, \quad (5 - 5)$$

$$u_t + \phi'_x + K_x - vQ = 0, \quad (5 - 6)$$

$$v_t + \phi'_y + K_y + uQ = 0, \quad (5 - 7)$$

where

$$D = \frac{\partial u}{\partial x} + \frac{\partial v}{\partial y}, \quad (5 - 8)$$

$$K = \frac{1}{2} (u^2 + v^2), \quad (5 - 9)$$

$$Q = \frac{\partial v}{\partial x} - \frac{\partial u}{\partial y} + f. \quad (5 - 10)$$

Because of the rapidly moving gravity waves, the stability condition for a numerical integration normally requires a much smaller time step than for the simple advection equation since $\Phi^{1/2} \gg U$. Similar results may be

expected with the more complete equations actually used in numerical weather prediction. Since the gravity waves are usually relatively unimportant in large-scale weather forecasting, the small time step required for computational stability increases the computing time considerably with little or no compensation by way of increased accuracy, perhaps even a loss. On the other hand, implicit differencing schemes, which may have no restriction on the size of the time step, have the serious disadvantage of requiring the inversion of a large matrix.

A semi-implicit scheme has the great advantage of permitting a relatively large time step without unduly increasing computation time. In other words the semi-implicit scheme slows artificially the propagation speed of the fastest gravity waves, which allows a much larger time step than the normal Courant-Fredrich-Lowy (CFL) stability criterion and also offsets some of the extra computational expense required to solve the system of equations assembled at each step. For this reason it is now necessary for the implementation of the semi-implicit time discretization to rewrite our equations in terms of a velocity potential χ and a streamfunction ψ defined by

$$u = \chi_x - \psi_y, \quad (5-11)$$

$$v = \chi_y + \psi_x, \quad (5-12)$$

with the following diagnostic relations

$$\chi_{xx} + \chi_{yy} = u_x + v_y, \quad (5 - 13)$$

$$\psi_{xx} + \psi_{yy} = v_x - u_y. \quad (5 - 14)$$

In other words, we can use vorticity and divergence or velocity potential and streamfunction as variables instead of velocity components. This means that second-order derivatives appear in the equations and Poisson equations have to be solved. Using linear elements, the scheme obtained for the Poisson equation is very similar to the finite difference scheme and can be inverted by the same technique. Cullen and Hall (1979) showed that the accuracy of the Galerkin finite element method solution was more accurate for the vorticity-divergence formulation of the shallow-water equations than for an increase in resolution with the primitive formulation. This unstaggered vorticity-divergence together with staggered variable formulation gives the best treatment of geostrophic adjustment for small-scale features (Williams and Schoenstadt, 1980).

Following the vorticity-divergence approach and dropping the primes for the rest of the chapter, the equations become

$$\phi_t + \phi D + (u\phi)_x + (v\phi)_y = 0, \quad (5 - 15)$$

$$\zeta_t + \nabla^2 \phi + (uQ)_x + (vQ)_y = 0, \quad (5 - 16)$$

$$D_t + \nabla^2 \phi + \nabla^2 K - (vQ)_x + (uQ)_y = 0. \quad (5 - 17)$$

where ∇^2 is the Laplacian operator and ζ is the relative vorticity given by

$$\zeta = \frac{\partial v}{\partial x} - \frac{\partial u}{\partial y}. \quad (5 - 18)$$

Now we express the velocity as the sum of the rotational and irrotational components

$$\mathbf{V} = \mathbf{V}_\psi + \mathbf{V}_\chi, \quad (5 - 19)$$

where

$$\mathbf{V}_\psi = \mathbf{k} \times \nabla \psi, \quad (5 - 20)$$

$$\mathbf{V}_\chi = \nabla \chi, \quad (5 - 21)$$

and then we are able to rewrite the equations using

$$D = \frac{\partial u}{\partial x} + \frac{\partial v}{\partial y} = \nabla^2 \chi, \quad (5 - 22)$$

$$\zeta = \frac{\partial v}{\partial x} - \frac{\partial u}{\partial y} = \nabla^2 \psi, \quad (5-23)$$

obtaining the following

$$\phi_t + \Phi \nabla^2 \chi = - (u\phi)_x - (v\phi)_y, \quad (5-24)$$

$$(\nabla^2 \psi)_t = - (uQ)_x - (vQ)_y, \quad (5-25)$$

$$(\nabla^2 \chi)_t + \nabla^2 \phi = (vQ)_x - (uQ)_y - (K_x)_x - (K_y)_y. \quad (5-26)$$

Manipulating now the last equation (5-26) and taking care of the bottom topography (assumed to be not a function of time), we can easily obtain

$$\phi_t + \Phi \nabla^2 \chi = - [u(\phi - \phi_B)]_x - [v(\phi - \phi_B)]_y, \quad (5-27)$$

$$(\nabla^2 \psi)_t = - (uQ)_x - (vQ)_y, \quad (5-28)$$

$$\nabla^2 (\chi_t + \phi) = (vQ - K_x)_x - (uQ + K_y)_y, \quad (5-29)$$

where ϕ_B is the bottom topography defined by the rigid surface $z = h_B(x, y)$ not a function of time (t).

We now define the domain of integration to be a channel encompassed by solid north-south walls with east-west cyclic boundary conditions. The boundary condition at the walls should be

$$\mathbf{V} \cdot \mathbf{n} = 0, \quad (5 - 30)$$

where \mathbf{n} is the outward pointing normal vector.

Here it is interesting to note that, in rewriting the equations in this form, we have increased their order in x and in y from first to second order and should expect that it may be necessary to impose further boundary conditions. However, since we have sufficient boundary conditions, already, any further specification must not be arbitrary but should be a consequence of the previous formulations. Along the walls, the v component of the velocity has to be equal to zero, resulting in

$$\phi_y = -fu. \quad (5 - 31)$$

The zonal and meridional components of the wind can be written now as

$$u = -\psi_y + \chi_x, \quad (5 - 32)$$

$$v = \psi_x + \chi_y. \quad (5 - 33)$$

Since the v component of the velocity has to be zero along the north and south walls then the obvious boundary condition should be

$$\psi_x + \chi_y = 0, \quad (5 - 34)$$

and we can satisfy the above condition by simply setting

$$\psi = 0, \quad (5 - 35)$$

when solving the vorticity equation, and

$$\chi_y = 0, \quad (5 - 36)$$

when solving the divergence equation. As a matter of fact this is an overspecification but equation (5-34) would be difficult to apply. Our initial conditions of course, must be specifically selected to satisfy both equations (5-35) and (5-36).

As we mentioned before we use a semi-implicit time discretization scheme for reasons of computational efficiency. Basically, this semi-implicit scheme is simply a modified leapfrog scheme giving a net saving in the computational time required to make a forecast for a given time. The way in which this is accomplished is to evaluate certain terms implicitly as a mean over times $(t - \Delta t)$ and $(t + \Delta t)$ rather than at time t .

Following this approach we evaluate all the terms on the left hand side of the equations as an average at times $(t - \Delta t)$ and $(t + \Delta t)$, and all the right hand side at time t . The prognostic equations then become

$$\phi_t + \Phi[\nabla^2 \chi(t - \Delta t) + \nabla^2 \chi(t + \Delta t)] = -[u(\phi - \phi_B)]_x - [v(\phi - \phi_B)]_y, \quad (5 - 37)$$

$$\nabla^2(\psi_t) = -(uQ)_x - (vQ)_y, \quad (5 - 38)$$

$$\nabla^2[\chi_t + \phi(t + \Delta t) + \phi(t - \Delta t)] = [(vQ) - K_x]_x - [(uQ) + K_y]_y. \quad (5 - 39)$$

If we now solve equation (5-39) for $\chi(t + \Delta t)$ and substitute into equation (5-37) we can finally get the following set of equations

$$\begin{aligned} \nabla^2\phi^* - \frac{\phi^*}{\Phi(\Delta t)^2} &= [(vQ) - K_x]_x - [(uQ) + K_y]_y - \frac{\phi(t - \Delta t)}{\Phi(\Delta t)^2} \\ &+ \frac{\nabla^2\chi(t - \Delta t)}{\Delta t} + \frac{1}{\Phi\Delta t} \{[u(\phi - \phi_B)]_x + [v(\phi - \phi_B)]_y\}, \end{aligned} \quad (5 - 40)$$

$$\nabla^2(\phi^* + \chi_t) = [(vQ) - K_x]_x - [(uQ) + K_y]_y, \quad (5 - 41)$$

$$\nabla^2(\psi_t) = -(uQ)_x - (vQ)_y, \quad (5 - 42)$$

where ϕ^* is given by

$$\phi^* = [\phi(t - \Delta t) - \phi(t + \Delta t)] / 2. \quad (5 - 43)$$

At this stage our initial system of three equations in three unknowns has been reduced to two Poisson equations and one Helmholtz equation to be solved at each time step. Our first step concerning the solution procedure should involve solving the ϕ equation (5-40) for a new value of ϕ^* . The second step should be then to solve equation (5-41) for $(\phi^* + \chi_t)$ and after substitution for χ_t . At last we solve equation (5-42) for ψ_t . Our history variables are ϕ , u , and v and they are updated after each time step as

$$\phi(t + \Delta t) = 2\phi^* - \phi(t - \Delta t), \quad (5 - 44)$$

$$u(t + \Delta t) = 2\Delta t [(\chi_t)_x - (\psi_t)_y] + u(t - \Delta t), \quad (5 - 45)$$

$$v(t + \Delta t) = 2\Delta t [(\chi_t)_y + (\psi_t)_x] + v(t - \Delta t). \quad (5 - 46)$$

In other words, numerical integration of the three forecast equations involves

- a. solve first a Helmholtz equation for ϕ ,
- b. solve a Poisson problem for ψ , and finally
- c. solve a Poisson problem for χ .

The space discretization consists of expanding the dependent variables in terms of basis functions defined on a variable mesh, and then orthogonalizing the error to the basis using the Galerkin procedure described in Chapter II. An appropriate approximating function for the rectangular subdivision should be a bilinear function (f). In this case the forecast set of equations in Galerkin form become

$$\begin{aligned} \int [\nabla^2 \phi_j^* f_j - \frac{\phi_j^* f_j}{\Phi(\Delta t)^2}] f_i = & \int \left\{ \frac{\partial}{\partial x} [(vQ)_j f_j - \frac{\partial}{\partial x} (K_j f_j)] \right\} f_i \\ & - \int \left\{ \frac{\partial}{\partial y} [(uQ)_j f_j + \frac{\partial}{\partial y} (K_j f_j)] \right\} f_i + \int \frac{1}{\Phi \Delta t} \left[\frac{\partial}{\partial x} (u(\phi - \phi_B)_j f_j + \frac{\partial}{\partial y} (v(\phi - \phi_B)_j f_j) \right] f_i \\ & - \int \frac{\phi_j}{\Phi(\Delta t)^2} (t - \Delta t) f_j f_i + \int \frac{1}{\Delta t} \nabla^2 \chi_j (t - \Delta t) f_j f_i, \end{aligned} \quad (5-47)$$

$$\int \nabla^2 \left(\frac{\partial v}{\partial t} \right)_j f_j f_i = - \int \left[\frac{\partial}{\partial x} (uQ)_j f_j \right] f_i - \int \left[\frac{\partial}{\partial y} (vQ)_j f_j \right] f_i, \quad (5-48)$$

$$\begin{aligned} \int \nabla^2 \left[\frac{\partial}{\partial t} (\chi)_j f_j + \phi_j^* f_j \right] f_i = & \int \left\{ \frac{\partial}{\partial x} [(vQ)_j f_j - \frac{\partial K}{\partial x}_j f_j] \right\} f_i \\ & - \int \left\{ \frac{\partial}{\partial y} [(uQ)_j f_j + \frac{\partial K}{\partial y}_j f_j] \right\} f_i. \end{aligned} \quad (5-49)$$

The integral sign here means an area integral over the domain, the j subscript refers to Einstein summation for the dependent variables and the i subscript is the i th nodal equation. Following the integration-by-parts procedure the final form of the forecast equations is given by

$$\begin{aligned}
 & - \int [\phi_j^* (\frac{\partial f}{\partial x})_j (\frac{\partial f}{\partial x})_i + \phi_j (\frac{\partial f}{\partial y})_j (\frac{\partial f}{\partial y})_i + \frac{\phi_j^* f_j f_i}{\Phi (\Delta t)^2}] = \int \left\{ \frac{\partial}{\partial x} [(vQ)_j - K_j (\frac{\partial f}{\partial x})_j] \right\} f_i \\
 & - \int \left\{ \frac{\partial}{\partial y} [(uQ)_j f_j + K_j (\frac{\partial K}{\partial y})_j] \right\} f_i + \int \frac{1}{\Phi \Delta t} \left\{ [u(\phi - \phi_B)]_j (\frac{\partial f}{\partial x})_j \right. \\
 & \quad \left. + [v(\phi - \phi_B)]_j (\frac{\partial f}{\partial y})_j \right\} f_i - \int \frac{\phi_j}{\Phi (\Delta t)^2} (t - \Delta t) f_j f_i + \int \frac{1}{\Delta t} [u_j (t - \Delta t) (\frac{\partial f}{\partial x})_j \\
 & \quad + v_j (t - \Delta t) (\frac{\partial f}{\partial y})_j] f_i - \int f_0 u_j f_j f_i, \tag{5-50}
 \end{aligned}$$

$$\begin{aligned}
 & \int [(\frac{\partial \psi}{\partial t})_j (\frac{\partial f}{\partial x})_j (\frac{\partial f}{\partial x})_i + (\frac{\partial \psi}{\partial t})_j (\frac{\partial f}{\partial y})_j (\frac{\partial f}{\partial y})_i] = - \int [(uQ)_j (\frac{\partial f}{\partial x})_j] f_i \\
 & - \int [(vQ)_j (\frac{\partial f}{\partial y})_j] f_i, \tag{5-51}
 \end{aligned}$$

$$- \int [(\frac{\partial \chi}{\partial t})_j (\frac{\partial f}{\partial x})_j (\frac{\partial f}{\partial x})_i + (\frac{\partial \chi}{\partial t})_j (\frac{\partial f}{\partial y})_j (\frac{\partial f}{\partial y})_i + \phi_j^* f_j f_i] =$$

$$\int \left\{ \frac{\partial}{\partial x} [(vQ)_j f_j - K_j (\frac{\partial f}{\partial x})_j] \right\} f_i - \int \left\{ \frac{\partial}{\partial x} [(uQ)_j f_j + K_j (\frac{\partial f}{\partial y})_j] \right\} f_i. \quad (5-52)$$

The line integral along the north and south walls has been dropped from the vorticity equation (5-51), since the value of $\partial\psi/\partial t$ is zero on the boundaries ($\psi = \text{constant}$). Also, the line integral along the north and south walls has been dropped from the divergence equation (5-52), because the value of the normal derivative along the north/south boundaries is zero. As we mentioned before the initial conditions should also satisfy the condition that the normal derivative of χ along the north/south boundaries is zero.

C. STABILITY ANALYSIS

Here we analyze the primitive form of the forecast equations and a semi-implicit time scheme, since the results will be identical for the vorticity-divergence form, (Hinsman, 1983). The one-dimensional equations with a mean flow, U , are given by

$$\frac{\partial u}{\partial t} + \frac{\partial \phi}{\partial x} = -U \frac{\partial u}{\partial x} + f v, \quad (5-53)$$

$$\frac{\partial v}{\partial t} = -U \frac{\partial v}{\partial x} - f u, \quad (5-54)$$

$$\frac{\partial \phi}{\partial t} + \Phi \frac{\partial u}{\partial x} = -U \frac{\partial \phi}{\partial x}. \quad (5-55)$$

Evaluating the time derivatives with a centered time differencing, and averaging the other terms on the left-hand side between time levels ($t + \Delta t$), and ($t - \Delta t$), equations (5-53), (5-54), and (5-55) become

$$\begin{aligned} & \frac{u(x, t + \Delta t) - u(x, t - \Delta t)}{2 \Delta t} + \frac{1}{2} \left[\frac{\phi(x + \Delta x, t + \Delta t) - \phi(x - \Delta x, t + \Delta t)}{2 \Delta x} \right. \\ & \quad \left. + \frac{\phi(x + \Delta x, t - \Delta t) - \phi(x - \Delta x, t - \Delta t)}{2 \Delta x} \right] = -U \left[\frac{u(x + \Delta x, t) - u(x - \Delta x, t)}{2 \Delta x} \right] \\ & \quad + f v(x, t), \end{aligned} \quad (5 - 56)$$

$$\frac{v(x, t + \Delta t) - v(x, t - \Delta t)}{2 \Delta t} = -U \left[\frac{v(x + \Delta x, t) - v(x - \Delta x, t)}{2 \Delta x} \right] - f u(x, t), \quad (5 - 57)$$

$$\begin{aligned} & \frac{\phi(x, t + \Delta t) - \phi(x, t - \Delta t)}{2 \Delta t} + \frac{\Phi}{2} \left[\frac{u(x + \Delta x, t + \Delta t) - u(x - \Delta x, t + \Delta t)}{2 \Delta x} \right. \\ & \quad \left. + \frac{u(x + \Delta x, t - \Delta t) - u(x - \Delta x, t - \Delta t)}{2 \Delta x} \right] = -U \left(\frac{\phi(x + \Delta x, t) - \phi(x - \Delta x, t)}{2 \Delta x} \right). \end{aligned} \quad (5 - 58)$$

Assuming now a function, F , given as

$$F(x, t) = F' \exp[i(kx + \omega t)], \quad (5 - 59)$$

and substituting into (5-56), (5-57), and (5-58), we can get

$$\frac{s}{\Delta t} \left\{ \frac{s^2}{\Delta t^2} - [f^2 + (k')^2 c^2 \Phi] \right\} = 0, \quad (5-60)$$

where

$$s = \sin(\omega \Delta t) + (k') u \Delta t, \quad (6-61)$$

$$c = \cos(\omega \Delta t), \quad (5-62)$$

$$(k') = \sin\left(\frac{k \Delta x}{\Delta x}\right). \quad (5-63)$$

The roots of equation (5-60) are given by

$$s = 0, \quad (5-64)$$

$$s^2 = (f \Delta t)^2 + c^2 (k \Delta t)^2 \Phi. \quad (5-65)$$

Requiring ω to be real, the roots of (5-65) yield the following stability criterion

$$\Delta t \leq \frac{1}{\left| \frac{U}{\Delta x} \right| + f}. \quad (5-66)$$

VI. INITIAL CONDITIONS

A. TOPOGRAPHIC ROSSBY WAVE

Let us first consider the horizontal momentum equations (3-8), and (3-9). If we cross differentiate (3-8) with respect to y , and (3-9) with respect to x , we obtain

$$\frac{\partial^2 u}{\partial y \partial t} + \frac{\partial u}{\partial y} \frac{\partial u}{\partial x} + u \frac{\partial^2 u}{\partial y^2} + \frac{\partial v}{\partial y} \frac{\partial u}{\partial y} + v \frac{\partial^2 u}{\partial y^2} - f \frac{\partial v}{\partial y} = -g \frac{\partial^2 h}{\partial y \partial x}, \quad (6-1)$$

$$\frac{\partial^2 v}{\partial x \partial t} + \frac{\partial u}{\partial x} \frac{\partial v}{\partial x} + u \frac{\partial^2 v}{\partial x^2} + \frac{\partial v}{\partial x} \frac{\partial v}{\partial y} + v \frac{\partial^2 v}{\partial x \partial y} + f \frac{\partial u}{\partial x} = -g \frac{\partial^2 h}{\partial x \partial y}. \quad (6-2)$$

If h is eliminated from (6-1), and (6-2), then

$$\begin{aligned} \frac{\partial}{\partial t} \left(\frac{\partial v}{\partial x} - \frac{\partial u}{\partial y} \right) + u \frac{\partial}{\partial x} \left(\frac{\partial v}{\partial x} - \frac{\partial u}{\partial y} \right) + v \frac{\partial}{\partial y} \left(\frac{\partial v}{\partial x} - \frac{\partial u}{\partial y} \right) = \\ -f \left(\frac{\partial u}{\partial x} + \frac{\partial u}{\partial y} \right) - \left(\frac{\partial v}{\partial x} - \frac{\partial u}{\partial y} \right) \left(\frac{\partial u}{\partial x} + \frac{\partial v}{\partial y} \right). \end{aligned} \quad (6-3)$$

Using now the following definition:

$$\zeta \equiv \omega_x = \frac{\partial v}{\partial x} - \frac{\partial u}{\partial y}, \quad (6-4)$$

where ζ is the vertical component of the vorticity, equation (6-3) yields

$$\frac{d\zeta}{dt} = \frac{\partial\zeta}{\partial t} + u \frac{\partial\zeta}{\partial x} + v \frac{\partial\zeta}{\partial y} = -(\zeta + f) \left(\frac{\partial u}{\partial x} + \frac{\partial v}{\partial y} \right). \quad (6-5)$$

If we now use equation (3-15), equation (6-4) can be written in the following form

$$\frac{d\zeta}{dt} = \frac{\zeta + f}{H} \frac{dH}{dt} \quad (6-6)$$

or

$$\frac{d}{dt} \left(\frac{\zeta + f}{H} \right) = 0, \quad (6-7)$$

where f is assumed to be constant.

At this stage, in order to find the proper initial conditions for the particular case of the topographic Rossby wave, we can work out a simplified theory for Rossby waves (Phillips, 1965).

Let us use cartesian coordinates and simplify the H variation, since H is a function of y , as

$$H = D(1 - sy), \quad (6-8)$$

where D is a constant, and

s is the slope of H in the y-direction.

Expanding the $(\zeta + f) / H$ term as

$$\frac{\zeta + f}{H} = \frac{\zeta + f}{D(1 - sy)} \approx \frac{(\zeta + f)(1 + sy)}{D} = \frac{\zeta + f + \zeta sy + f sy}{D}, \quad (6-9)$$

and considering the term (ζsy) to be very small, equation (6-7) becomes

$$\frac{d}{dt} (\zeta + f sy) = 0. \quad (6-10)$$

Equation (6-10) can be also written as

$$\frac{d\zeta}{dt} + f s \frac{dy}{dt} = 0 \quad (6-11)$$

or

$$\frac{d\zeta}{dt} + f sv = 0. \quad (6-12)$$

Assuming small amplitude motion, and no mean flow, equation (6-12) becomes

$$\frac{\partial \zeta}{\partial t} + f s v = 0. \quad (6 - 13)$$

In the case of a small Rossby number, we can also use the following relationships:

$$\zeta = \nabla^2 \psi \quad (6 - 14)$$

and

$$v = \frac{\partial \psi}{\partial x}, \quad (6 - 15)$$

where $\psi = P / (\rho f)$. Equation (6-13) then becomes

$$\frac{\partial}{\partial t} (\nabla^2 \psi) + f s \left(\frac{\partial \psi}{\partial x} \right) = 0 \quad (6 - 16)$$

or

$$\frac{\partial}{\partial t} (\nabla^2 \psi) + \beta \left(\frac{\partial \psi}{\partial x} \right) = 0, \quad (6 - 17)$$

where $\beta = f s$.

Assuming a solution of the form

$$\psi = \psi(y) \exp[i\mu(x - ct)], \quad (6 - 18)$$

substitution into equation (6-18) yields the following problem for $\psi(y)$

$$\left(\frac{d^2\psi}{dy^2} - \mu^2 \right) (-i\mu c) \exp[i\mu(x - ct)] + \beta \psi(i\mu) \exp[i\mu(x - ct)] = 0 \quad (6 - 19)$$

or

$$\frac{d^2\psi}{dy^2} - \left(\mu^2 + \frac{\beta}{c} \right) \psi = 0. \quad (6 - 20)$$

Nondimensionalizing the domain of integration (as shown in Fig. 6.1), our boundary problem for $\psi(y)$ becomes

$$\frac{d^2\psi_1}{dy^2} - \left(\mu_1^2 + \frac{\beta_1}{c} \right) \psi_1 = 0, \quad (6 - 21)$$

with

$$\psi_1(0) = 0, \quad (6 - 22)$$

$$\psi_1(a) = \psi_2(a), \quad (6 - 23)$$

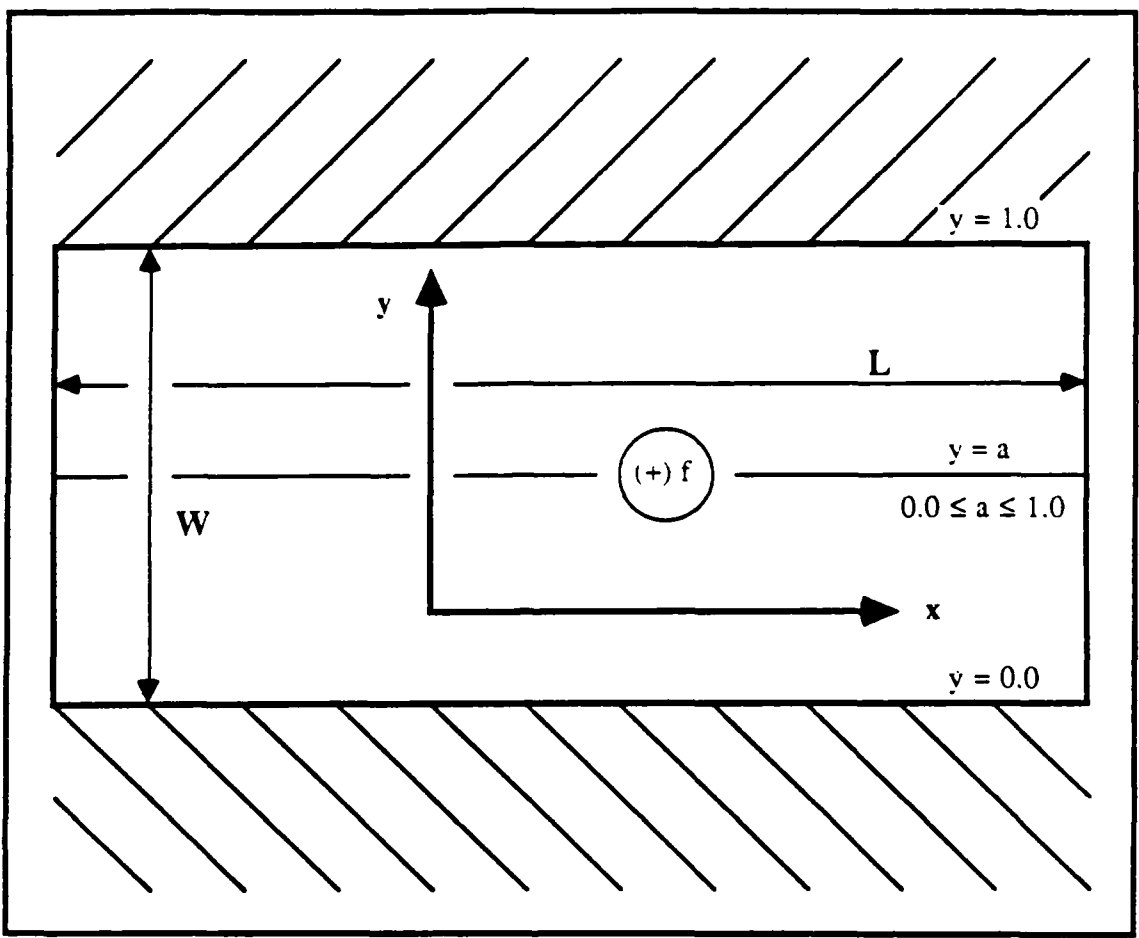


Fig. 6.1 Schematic representation of the non-dimensional domain of integration.

$$\frac{d\psi_1(a)}{dy} = \frac{d\psi_2(a)}{dy}, \quad (6-24)$$

for the lower part of the channel, and

$$\frac{d^2\psi_2}{dy^2} - (\mu_2^2 + \frac{\beta_2}{c}) \psi_2 = 0, \quad (6-25)$$

with

$$\psi_2(1) = 0, \quad (6-26)$$

$$\psi_2(a) = \psi_1(a), \quad (6-27)$$

$$\frac{d\psi_1(a)}{dy} = \frac{d\psi_2(a)}{dy}, \quad (6-28)$$

for the upper part of the channel. Here μ_1 , and μ_2 are the corresponding wavenumbers. Also

$$\beta_1 = s_1 f, \quad (6-29)$$

$$\beta_2 = s_2 f, \quad (6-30)$$

where s_1 is the slope of H in the y -direction for the lower part, and
 s_2 is the slope of H in the y -direction for the upper part.

There are two distinct cases. In the first case, the lower part of the channel controls the phase speed c . The solutions to this case are

$$\psi_1 = A \sin(\lambda_1 y), \quad (6 - 31)$$

for the lower part, and

$$\psi_1 = B \sinh[\lambda_2^*(1 - y)], \quad (6 - 32)$$

for the upper part. For the particular case where $a = 0.5$

$$\beta_1 = -\beta_2, \quad (6 - 33)$$

$$-\lambda_1^2 = \mu_1^2 + \frac{\beta_1}{c}, \quad (6 - 34)$$

$$-(\lambda_2^*)^2 = -2\mu_1^2 - \lambda_1^2. \quad (6 - 35)$$

Furthermore, the coefficients A , and B are to be determined. In the second distinct case, the upper part controls the phase speed c . The solutions to this case are

$$\psi_2 = C \sin[\lambda_2(1 - y)], \quad (6 - 36)$$

for the upper part, and

$$\psi_2 = D \sinh(\lambda_1^* y), \quad (6 - 37)$$

for the lower part. For the particular case where $a = 0.5$

$$\beta_2 = -\beta_1, \quad (6 - 38)$$

$$-\lambda_2^2 = \mu_2^2 + \frac{\beta_2}{c}, \quad (6 - 39)$$

$$-(\lambda_1^*)^2 = -2\mu_2^2 - \lambda_2^2. \quad (6 - 40)$$

Once more, the coefficients C and D are to be determined.

Let us now consider the second case, where the upper part controls the phase speed c . Boundary conditions (6-23), and (6-27) yield

$$\sin[\lambda_2(1 - a)] C - [\exp(\lambda_1^* a) - \exp(-\lambda_1^* a)] D = 0. \quad (6 - 41)$$

In the same way, the boundary conditions (6-24) and (6-28) also yield

$$- \lambda_2 \cos[\lambda_2(1-a)] C - \lambda_1^* [\exp(\lambda_1^* a) + \exp(-\lambda_1^* a)] D. \quad (6-42)$$

Equations (6-41) and (6-42) lead us to the following eigenvalue problem

$$\begin{aligned} & \lambda_1^* [\exp(\lambda_1^* a) + \exp(-\lambda_1^* a)] \sin[\lambda_2(1-a)] \\ & + \lambda_2 [\exp(\lambda_1^* a) - \exp(-\lambda_1^* a)] \cos[\lambda_2(1-a)] = 0. \end{aligned} \quad (6-43)$$

Using relationship (6-40), equation (6-43) becomes

$$\begin{aligned} & \lambda_1^* [\exp(\lambda_1^* a) + \exp(-\lambda_1^* a)] \sin\{[(\lambda_1^*)^2 - 2\mu_2^2]^{1/2} (1-a)\} \\ & + [(\lambda_1^*)^2 - 2\mu_2^2]^{1/2} [\exp(\lambda_1^* a) - \exp(-\lambda_1^* a)] \\ & \cos\{[(\lambda_1^*)^2 - 2\mu_2^2]^{1/2} (1-a)\} = 0, \end{aligned} \quad (6-44)$$

where

$$\mu_2 = \frac{2\pi}{L} W. \quad (6-45)$$

Here L is the horizontal length scale, and W represents the width of the channel. For our case we choose a channel $30^\circ \times 30^\circ$ longitude by latitude, which gives

$L = 5653510.75 \text{ m},$

$W = 4896083.93 \text{ m},$

so μ_2 equals to 5.4413981

We are able to solve (6-44) numerically (see Table IV) using Newton's method. Using Table IV, we can determine coefficients C, and D for any particular mode. For instance if

$$\lambda_1^* = 9.3191,$$

$$\lambda_2 = 5.2562,$$

then in order to determine the relation between C, and D, the following set of equations has to be solved

$$0.4912 C - 105.5791 D = 0, \quad (6-46)$$

$$4.5787 C - 984.0783 D = 0, \quad (6-47)$$

resulting in

λ_2	λ_1^*
5.2562	9.3191
11.1881	13.5791
17.3683	18.9967
23.6124	24.8347
29.8772	30.8523

Table IV Numerical solutions of equation (6-44), obtained using
Newton's method.

$$D = \frac{0.4912}{105.5791} C \quad (6 - 47)$$

or

$$C = 1.0,$$

$$D = 0.004652.$$

Here C is chosen to be 1. Finally, the solution to the case where the upper part controls c, should be given by

$$\psi_2 = \sin [5.2562 (1 - y)], \quad 0.5 \leq y \leq 1.0, \quad (6 - 48)$$

for the upper part and

$$\psi_2 = 0.004652 [\exp (9.3191 y) - \exp (-9.3191 y)], \\ 0.0 \leq y \leq 0.5, \quad (6 - 49)$$

for the lower part. The graph of this solution is shown in Fig. 6.2.

Following the same approach, with the use of Table IV, we are able to obtain

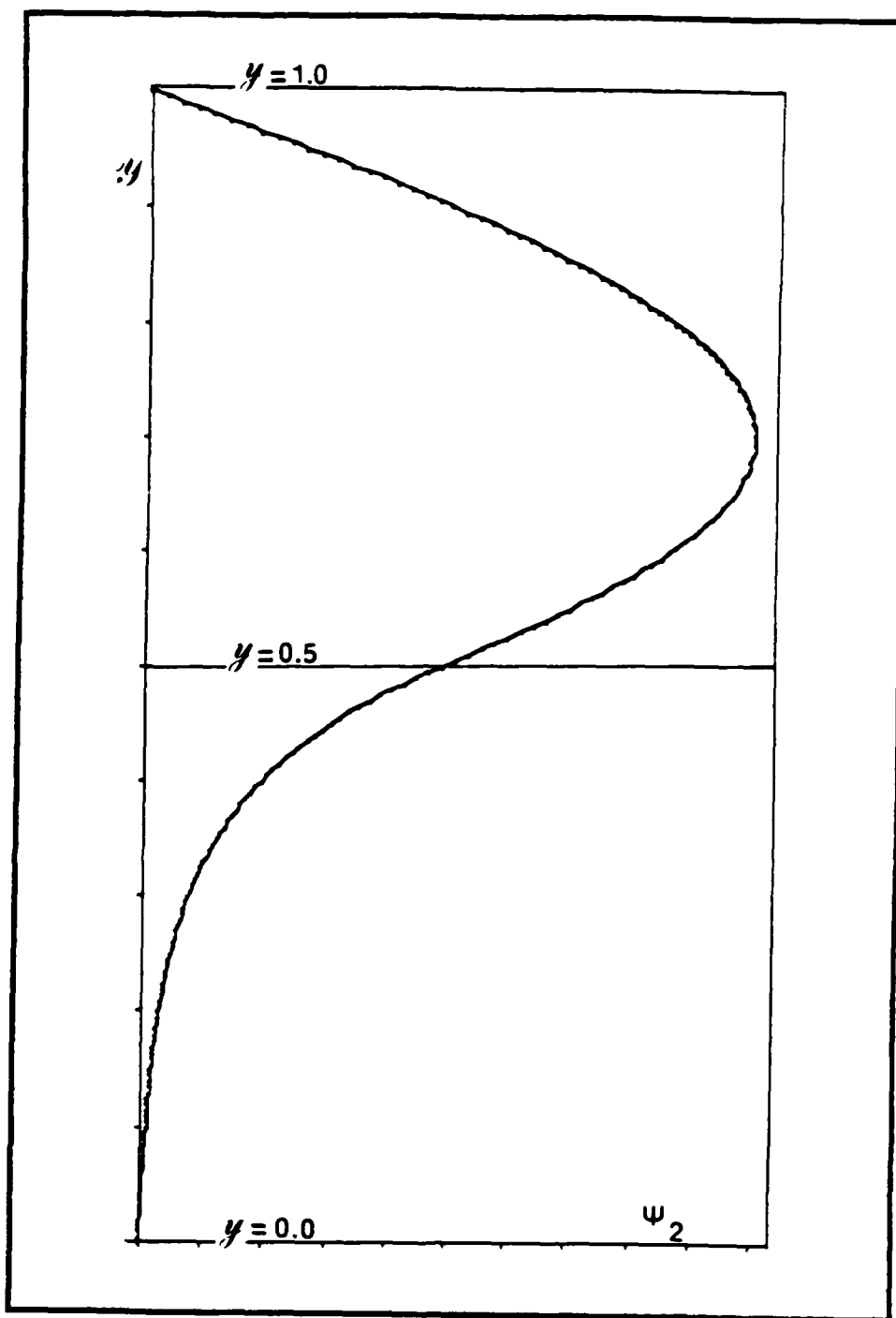


Fig. 6.2 Graph of the solution $\psi_2(y)$ where the upper part of the channel controls c , obtained from equations (6-48), and (6-49).

$$\psi_2(\text{upper}) = \sin [11.1881(1-y)], \quad 0.5 \leq y \leq 1.0, \quad (6-50)$$

$$\psi_2(\text{lower}) = -0.000716 [\exp(13.5791y) - \exp(-13.5791y)],$$

$$0.0 \leq y \leq 0.5, \quad (6-51)$$

for the case where

$$\lambda_1^* = 13.5791,$$

$$\lambda_2 = 11.1881,$$

shown in Fig. 6.3, and

$$\psi_2(\text{upper}) = \sin [17.3683(1-y)], \quad 0.5 \leq y \leq 1.0, \quad (6-52)$$

$$\psi_2(\text{lower}) = 0.0000506 [\exp(18.9967y) - \exp(-18.9967y)],$$

$$0.0 \leq y \leq 0.5, \quad (6-53)$$

for the case where

$$\lambda_1^* = 18.9967,$$

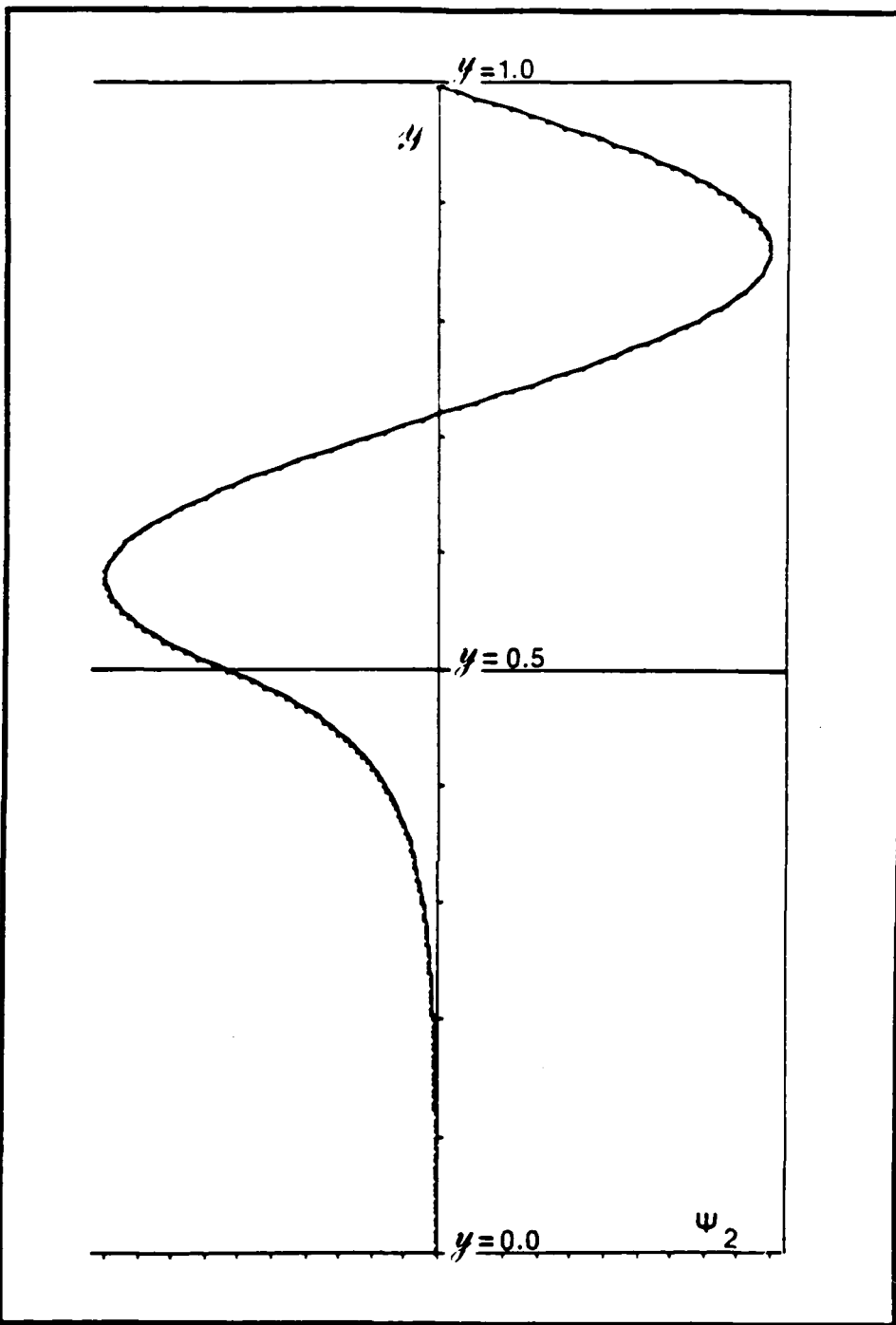


Fig. 6.3 As in Fig. 6.2, except for equations (6-50), and (6-51).

$$\lambda_2 = 17.3683,$$

shown in Fig. 6.4.

The corresponding solutions for the case where the lower part controls the phase speed c , are given below

$$\psi_1 (\text{lower}) = \sin (5.2562 y), \quad 0.0 \leq y \leq 0.5, \quad (6-54)$$

$$\psi_1 (\text{upper}) = 0.004652 \{\exp[9.3191(1-y)] - \exp[-9.3191(1-y)]\},$$

$$0.5 \leq y \leq 1.0, \quad (6-55)$$

for the case where

$$\lambda_2^* = 9.3191,$$

$$\lambda_1 = 5.2562,$$

shown in Fig. 6.5,

$$\psi_1 (\text{lower}) = \sin (11.1881 y), \quad 0.0 \leq y \leq 0.5, \quad (6-56)$$

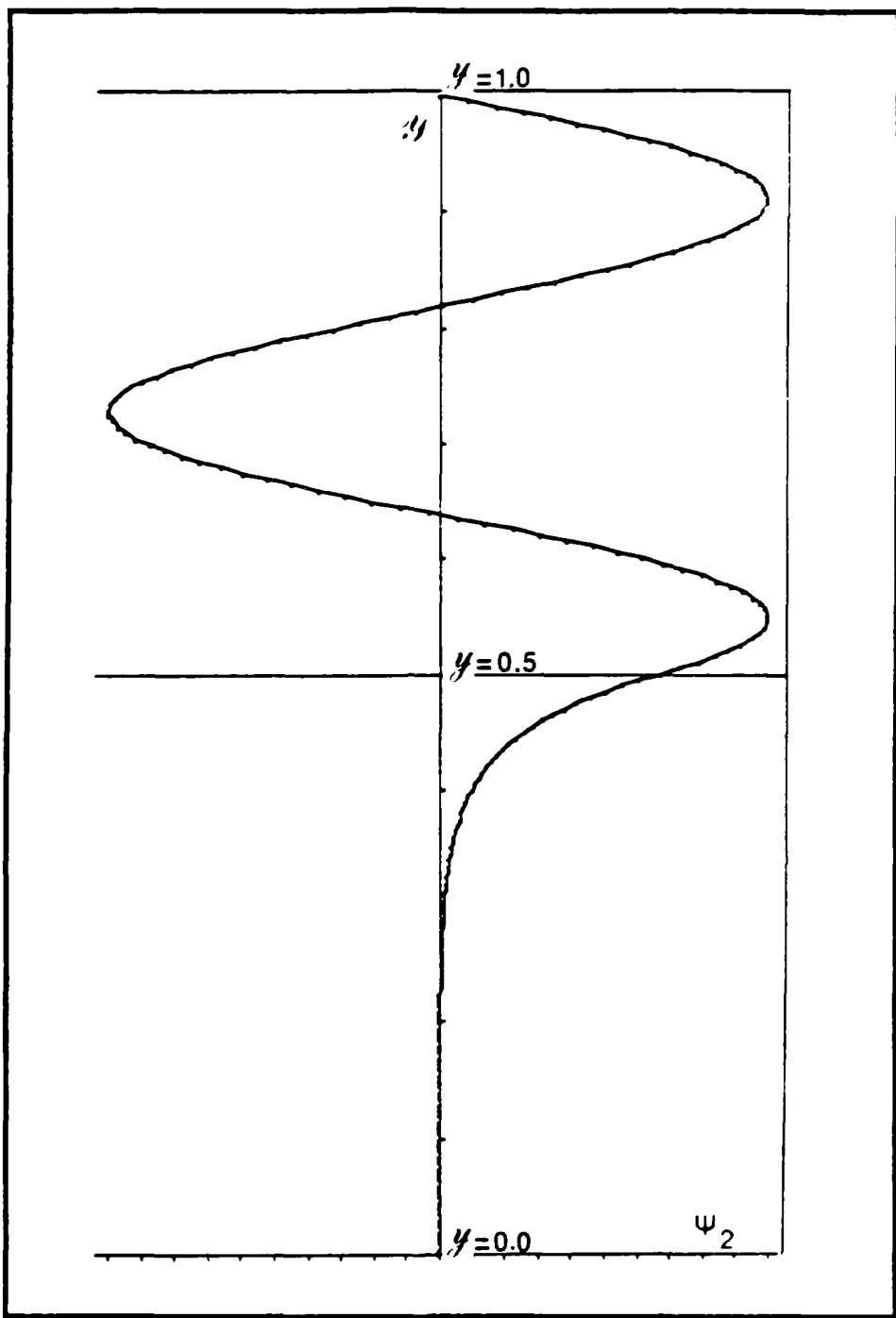


Fig. 6.4 As in Fig. 6.2, except for equations (6-52), and (6-53).

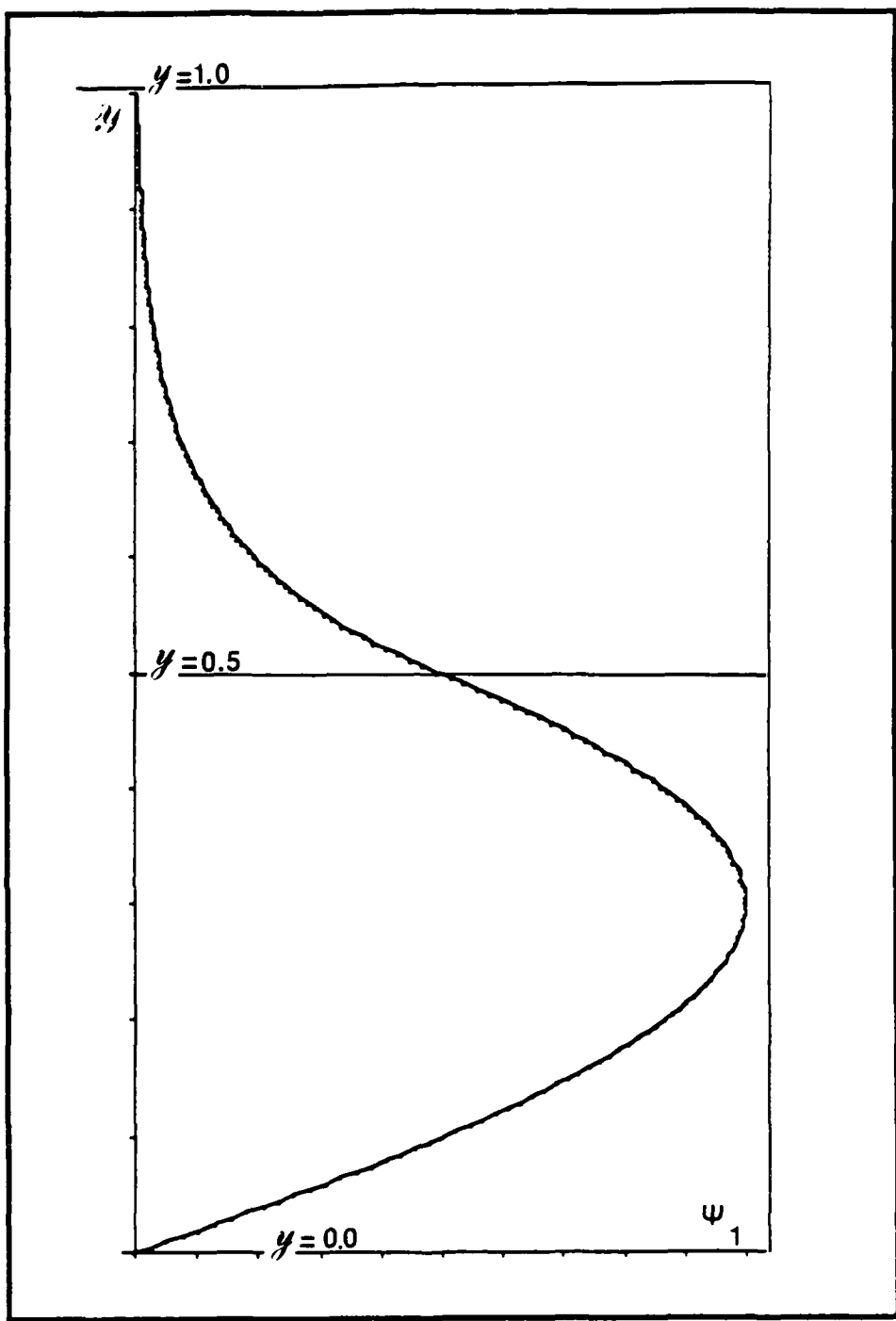


Fig. 6.5 Graph of the solution $\psi_1(y)$ where the lower part of the channel controls c , obtained from equations (6-54), and (6-55).

$$\psi_1 \text{ (upper)} = -0.000716 \{\exp[13.5791(1 - y)] - \exp[-13.5791(1 - y)]\},$$

$$0.5 \leq y \leq 1.0, \quad (6 - 57)$$

for the case where

$$\lambda_2^* = 13.5791,$$

$$\lambda_1 = 11.1881,$$

shown in Fig. 6.6, and

$$\psi_1 \text{ (lower)} = \sin (17.3683 y), \quad 0.0 \leq y \leq 0.5, \quad (6 - 58)$$

$$\psi_1 \text{ (upper)} = 0.0000506 \{\exp[18.9967(1 - y)] - \exp[-18.9967(1 - y)]\},$$

$$0.5 \leq y \leq 1.0, \quad (6 - 59)$$

for the case where

$$\lambda_2^* = 18.9967,$$

$$\lambda_1 = 17.3683,$$

shown in Fig. 6.7.

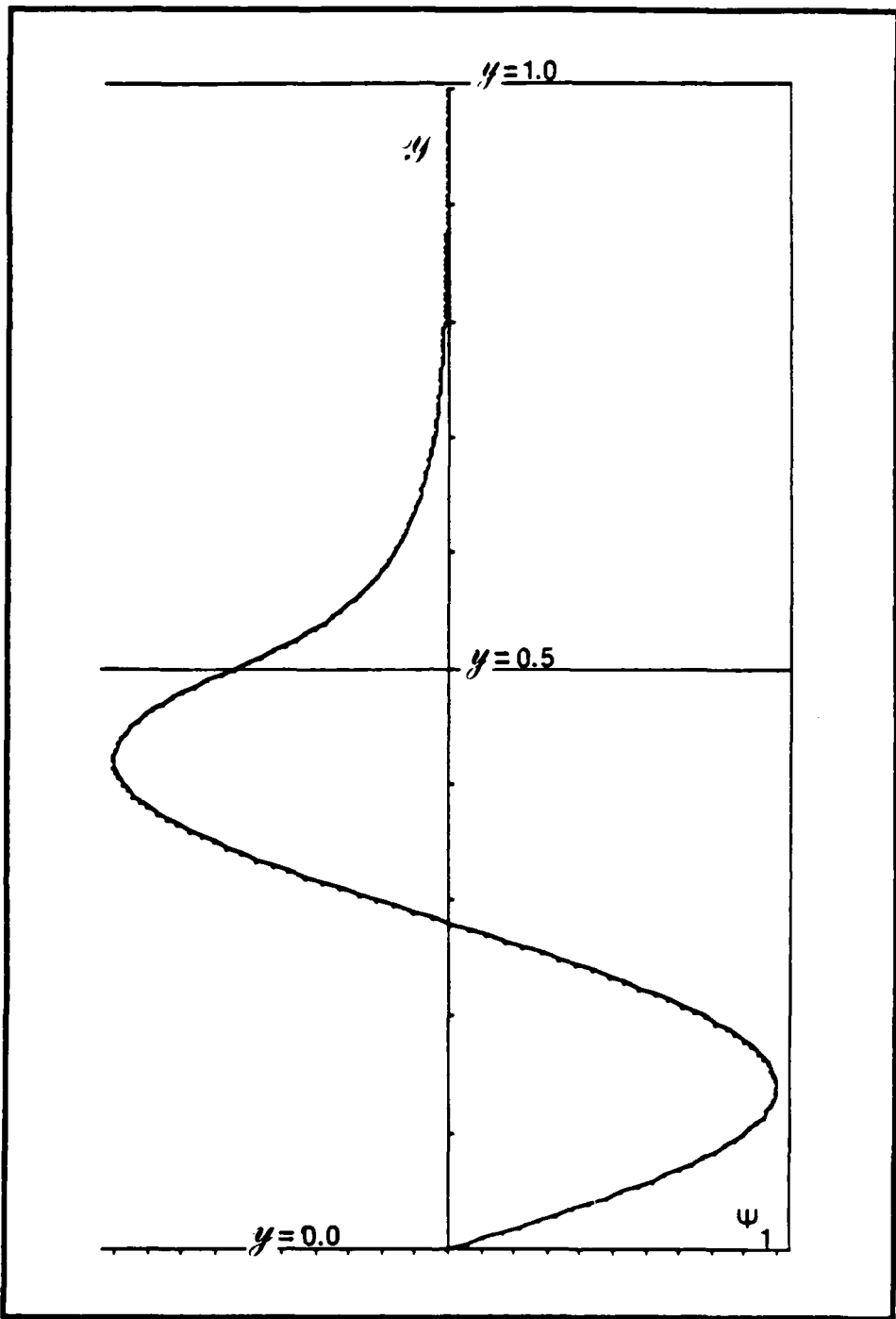


Fig. 6.6 As in Fig. 6.5, except for equations (6-56), and (6-57).

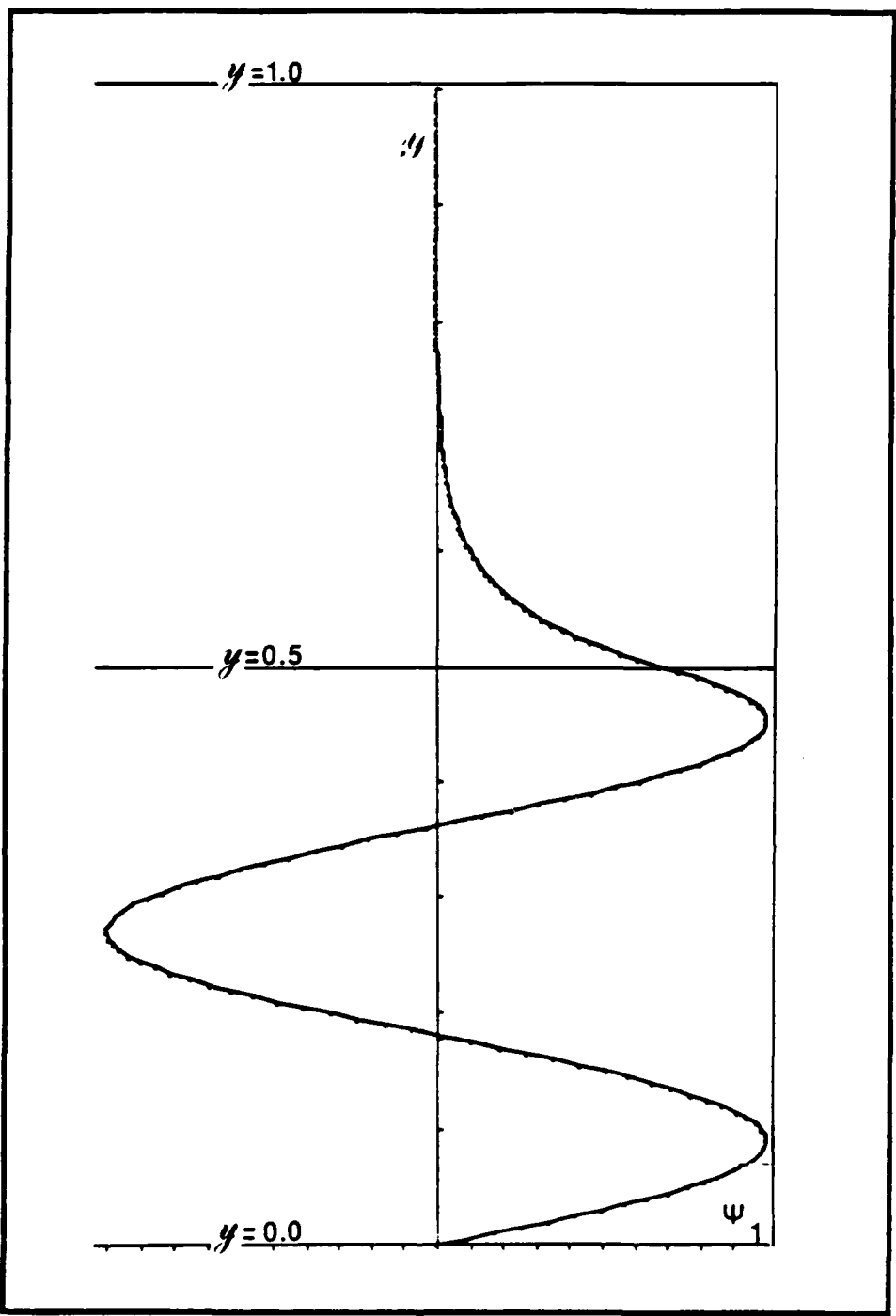


Fig. 6.7 As in Fig. 6.5, except for equations (6-58), and (6-59).

In our experiments we select initial conditions in the form described by equations (6-54) and (6-55). That choice appears to be an excellent one, providing us with the most proper modes to observe the topographic Rossby wave. It is desired that the initial conditions allow a relative amount of control for the input parameters as well as satisfying the boundary conditions.

The next logical step is to determine the analytic expression for the streamfunction ψ . Following closely equations (6-54) and (6-55), the exact expression for ψ , is given by

$$\psi = \frac{A}{2} [\sin(\frac{\lambda_1}{w} y)] [\sin(\frac{2\pi n}{L} x)] - U_m (y - y_{mid}) + \frac{\Phi}{f_0}, \quad (6 - 60)$$

for the lower part ($0.0 \leq y \leq 0.5$), and

$$\begin{aligned} \psi = 0.004652 \frac{A}{2} & [\exp(\lambda_2^* y) - \exp(-\lambda_2^* y)] [\sin(\frac{2\pi n}{L} x)] \\ & - U_m (y - y_{mid}) + \frac{\Phi}{f_0}, \end{aligned} \quad (6 - 61)$$

for the upper part ($0.5 \leq y \leq 1.0$), where

A = amplitude of perturbation,

w = width of the channel (4896083.93m),

L = length of the channel (5653510.75m),

n = wave number,

U_m = mean flow speed,

y_{mid} = middle point of the channel,

$\lambda_1 = 5.2562$, and

$\lambda_2^* = 9.3191$

The first term in the expressions (6-60) and (6-61) represents the perturbation part. The second term is the north/south slope necessary to support a mean flow of U_m . The last term plays the role of the mean depth term. The geopotential height, ϕ , is related geostrophically to the streamfunction, ψ , by the following relationship

$$\phi = f_0 \psi, \quad (6-62)$$

resulting in

$$\phi = \frac{f_0 A}{2} \sin(a_1 y) \sin(a_2 x) - f_0 U_m (y - y_{mid}) + \Phi, \quad (6-63)$$

for the lower part ($0.0 \leq y \leq 0.5$), and

$$\phi = 0.004652 \frac{f_0 A}{2} [\exp(a_3 y) - \exp(-a_3 y)] \sin(a_2 x) - f_0 U_m (y - y_{mid}) + \Phi, \quad (6-64)$$

for the upper part ($0.5 \leq y \leq 1.0$), where

$$a_1 = \frac{\lambda_1}{W}, \quad (6-65)$$

$$a_2 = \frac{2\pi n}{L}, \quad (6-66)$$

$$a_3 = \lambda_2^*. \quad (6-67)$$

The u , and v components of velocity can be derived using the following geostrophic expressions

$$u = - \frac{1}{f} \frac{\partial \phi}{\partial y}, \quad (6-68)$$

$$v = \frac{1}{f} \frac{\partial \phi}{\partial x}, \quad (6-69)$$

resulting in

$$u(\text{lower}) = U_m - \frac{A a_1}{2} \cos(a_1 y) \sin(a_2 x), \quad 0.0 \leq y \leq 0.5, \quad (6-70)$$

$$v(\text{lower}) = \frac{A a_2}{2} \sin(a_1 y) \cos(a_2 x), \quad 0.0 \leq y \leq 0.5, \quad (6-71)$$

and

$$u(\text{upper}) = U_m - 0.043352 \frac{A}{2} [\exp(a_3 y) + \exp(-a_3 y)] \sin(a_2 x), \\ 0.5 \leq y \leq 1.0, \quad (6-72)$$

$$v(\text{upper}) = \frac{A a_2}{2} [\exp(a_3 y) - \exp(-a_3 y)] \cos(a_2 x), \quad 0.5 \leq y \leq 1.0. \quad (6-73)$$

The initial vorticity can be also derived, using the following relationship

$$\zeta = \nabla^2 \psi, \quad (6-74)$$

resulting in

$$\zeta = -\frac{A}{2} [(a_1)^2 + (a_2)^2] \sin(a_1 y) \sin(a_2 x), \quad (6-75)$$

for the lower part ($0.0 \leq y \leq 0.5$), and

$$\zeta = 0.004652 \frac{A}{2} [(a_3)^2 - (a_2)^2] [\exp(a_3 y) - \exp(-a_3 y)] \sin(a_2 x), \quad (6 - 76)$$

for the upper part ($0.5 \leq y \leq 1.0$).

We set the initial divergence equal to zero, assuming the initial fields to be almost geostrophic. The initial fields of geopotential, u-component, v-component, vorticity, and divergence for the case where the lower part of the channel controls the phase speed, c, and no topography effect is involved (Equations 6-60 through 6-76), are illustrated in Fig. 6.8.

B. HYDRAULIC JUMPS

The stationary theory predicts the formation of jumps in pairs, one upstream and one downstream of the rigid ridge (Houghton and Kasahara, 1968). The classification shown in Fig. 4.5, is strictly valid for non-rotating flows. No equivalent theory exists for flows over mountains in a rotating system. Houghton (1969) and Williams and Hori (1970) consider the transient motion of a shallow water layer on an f-plane without mountains starting from an initial velocity disturbance of magnitude U over a length L.

For our case we consider a nonrotating Shallow-Water system ($f = 0$). It is desired once more, that the initial conditions allow a relative amount of control for the input parameters as well as satisfying the boundary conditions. The forecast model history-carrying variables are ϕ , u , and v . The analytic expression for the streamfunction, ψ , is given by

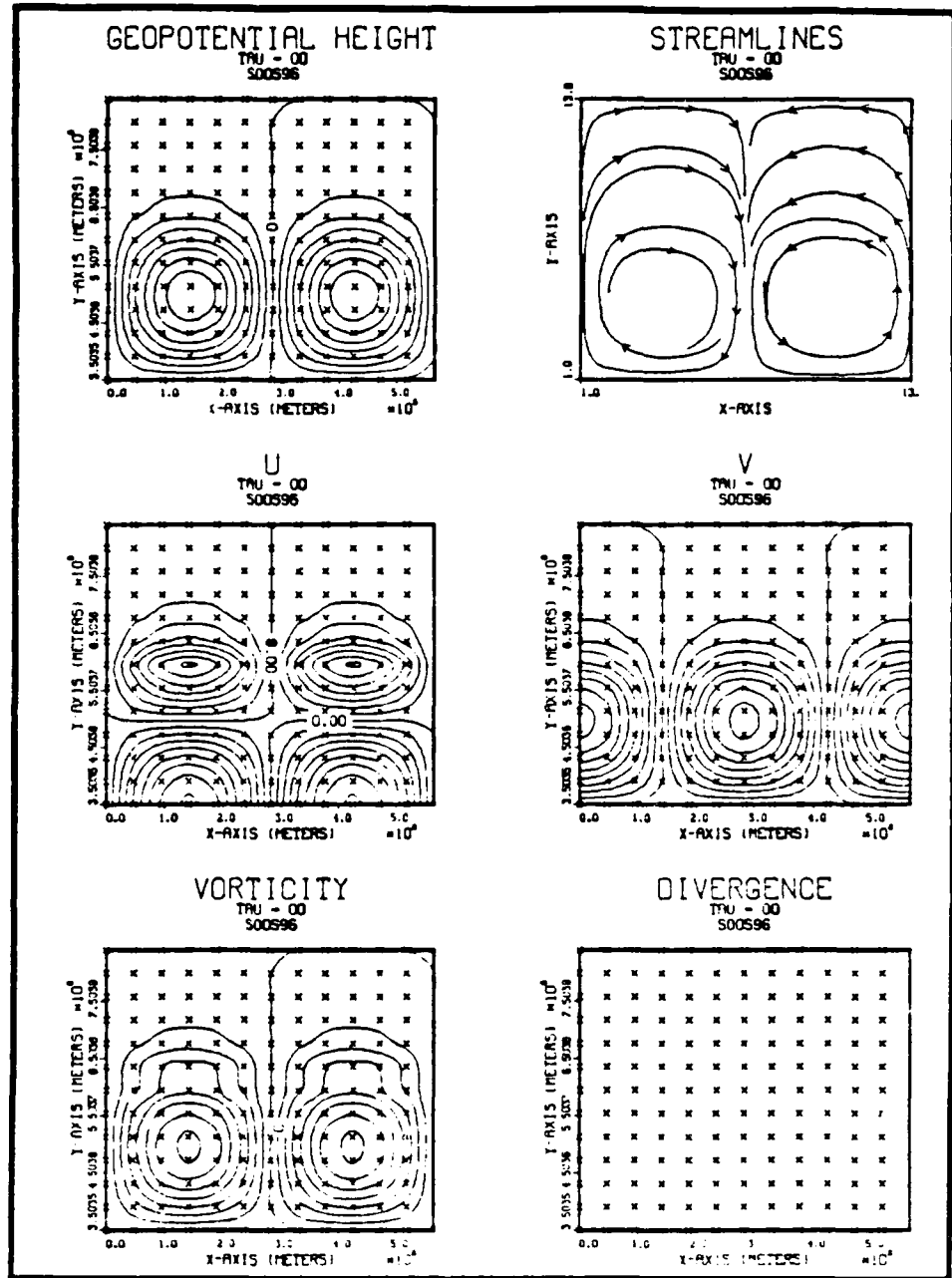


Fig. 6.8 Initial conditions for the GFEM model with a rectangular subdivision, and wave number one. Contour intervals are $600 \text{ m}^2/\text{s}^2$ for geopotential height, 0.2 m/s for u and v , $0.6 \times 10^{-6} \text{ s}^{-1}$ for vorticity. Nodal points are denoted by an x.

$$\psi = -U y, \quad 0.0 \leq y \leq W, \quad (6-77)$$

where U is the velocity of the flow in the region far from the ridge. Also the initial geopotential height, ϕ_0 , is set equal to the mean depth, gH .

Finally, the initial u - and v - components of the velocity are given by

$$u_0 = U, \quad (6-78)$$

$$v_0 = 0. \quad (6-79)$$

VII. EXPERIMENTS AND RESULTS

Our first experiment involves bottom topography which is composed of two regions. These two regions can provide us with either an east-west oriented ridge or valley. We consider conditions with no mean flow, the objective being to examine how well our model simulates the topographic Rossby wave, by comparison with the theoretical phase speed values.

Our second experiment is to investigate the ability of the same model to create hydraulic jumps analogous to that predicted from the analytical approach (Chapter IV). In this case we consider a mean flow forced to pass over a topographic ridge which extends north-south across the channel. In this experiment we will consider several distinct cases corresponding to different discrete domains obtained by the theory (Fig. 4.5).

A. EXPERIMENT I

We perform experiment I using the GFEM rectangular model described in Chapter VI. The basic difference between the rectangular and triangular models is in the approximating polynomials. The rectangular polynomials are bilinear while the triangular polynomials are linear. Many integrals require evaluation during the integration process. We could use numerical quadrature, however, a more efficient method is available through the use

of natural coordinates. We can accomplish quadrature with no error by formula with this method. A description of the natural coordinate method is given in Appendix A for the rectangular discretization.

The diagram for the grids for the rectangular subdivision is shown in Fig. 5.1. The domain of integration is 5,653.5 km in the x-direction and 4,896.1 km in the y-direction. The model has 12 increments in the x- and y- directions, which gives the model 156 degrees of freedom. The Δx is 471.1 km, and the Δy is 408.0 km. The value of the Coriolis parameter is taken to be 0.00010284, corresponding to 45.0° N latitude.

The initial conditions for the case of the topographic Rossby wave are described in Chapter VI. A small wave perturbation is added to the geopotential field which includes the mean height and the required north/south slope in case of non zero mean flow. It consists of a wave with a wavenumber one, confined primarily to the south part of the channel domain. In our case, we choose a mean depth of 1,000 meters, and no mean flow. The motion is confined in a channel with cyclic boundary conditions as shown in Fig. 7.1. We examine small amplitude wave motion encountering different slopes of the bottom topography in the y-direction as illustrated in Fig. 7.2, and 7.3. We can visualize the whole setting as if we placed a long triangular mountain with its peak centered in the middle of the width of the channel. It is obvious that the slope of the lower part of the channel, s_1 , corresponds to the south slope of the mountain, while the slope of the upper part, s_2 , corresponds to the north slope. No matter what

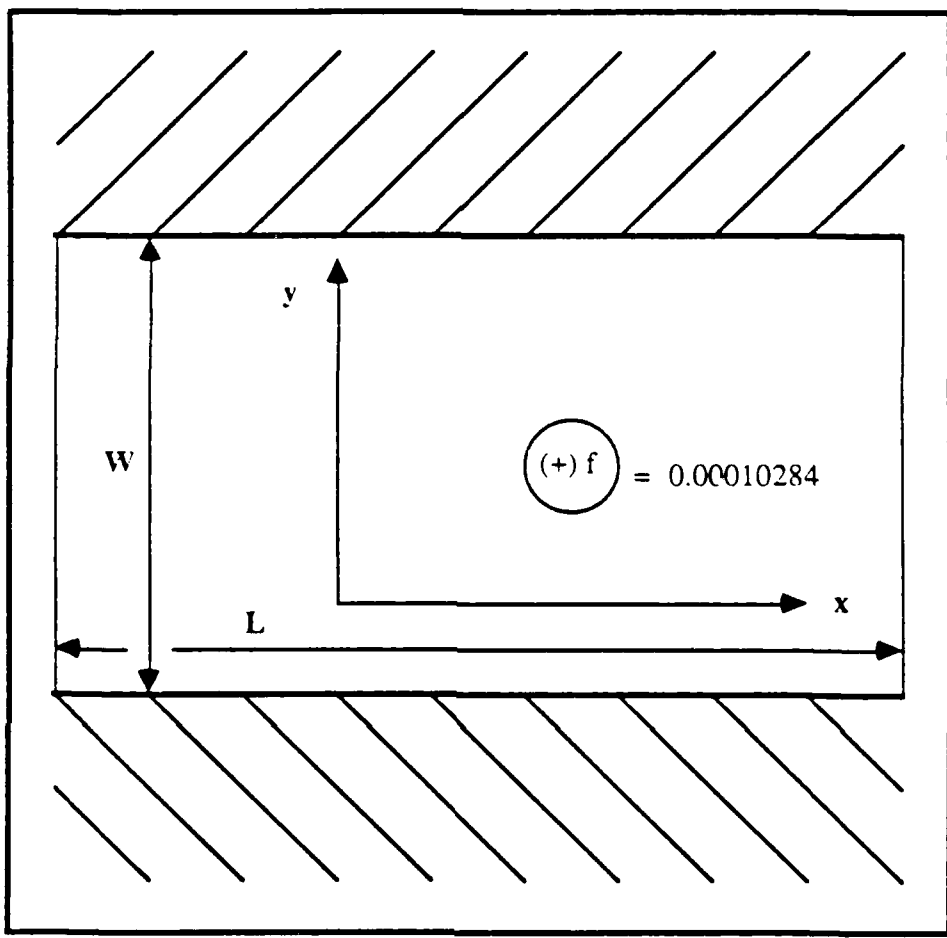


Fig. 7.1 Schematic representation of the domain of integration.

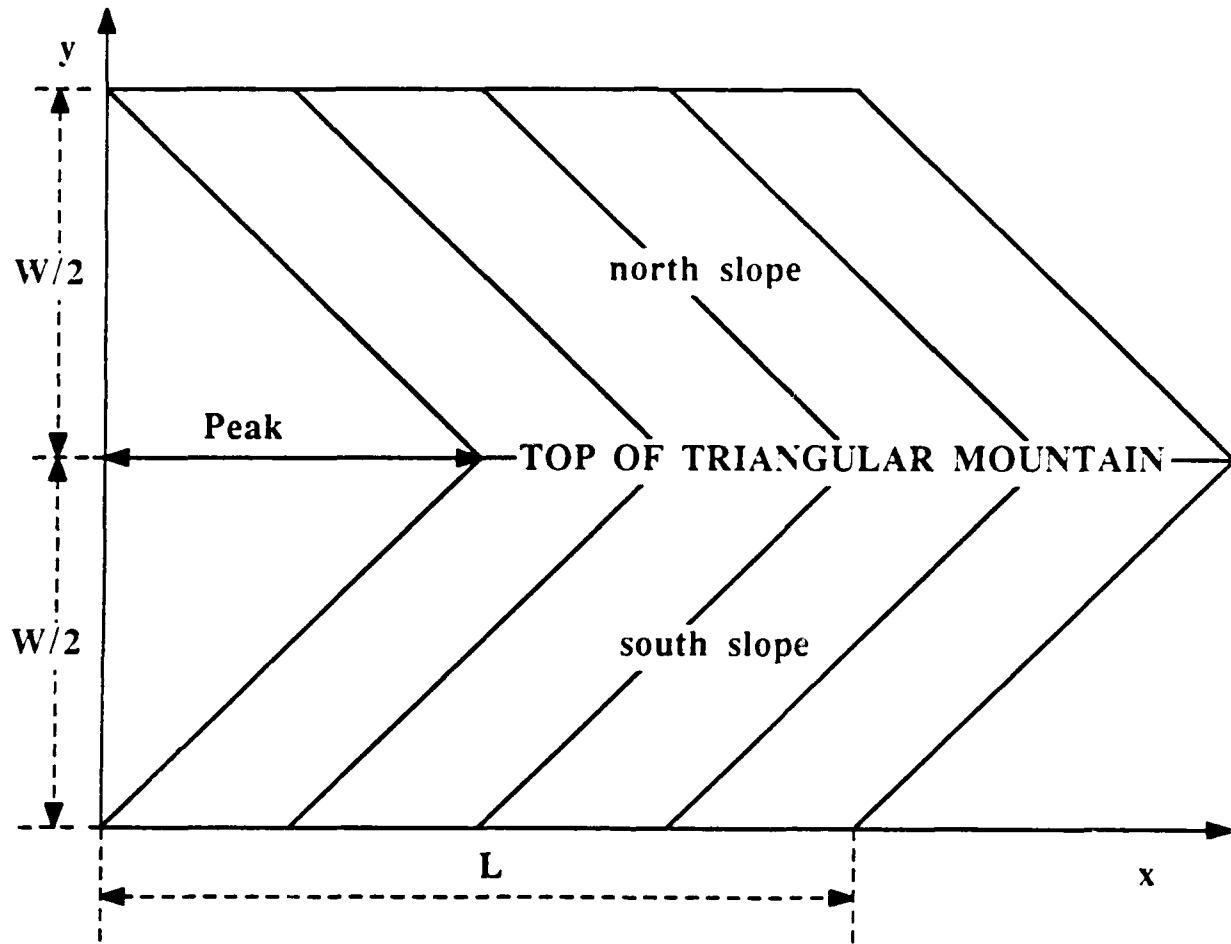


Fig. 7.2 Schematic representation of the bottom topography for the case of triangular mountain.

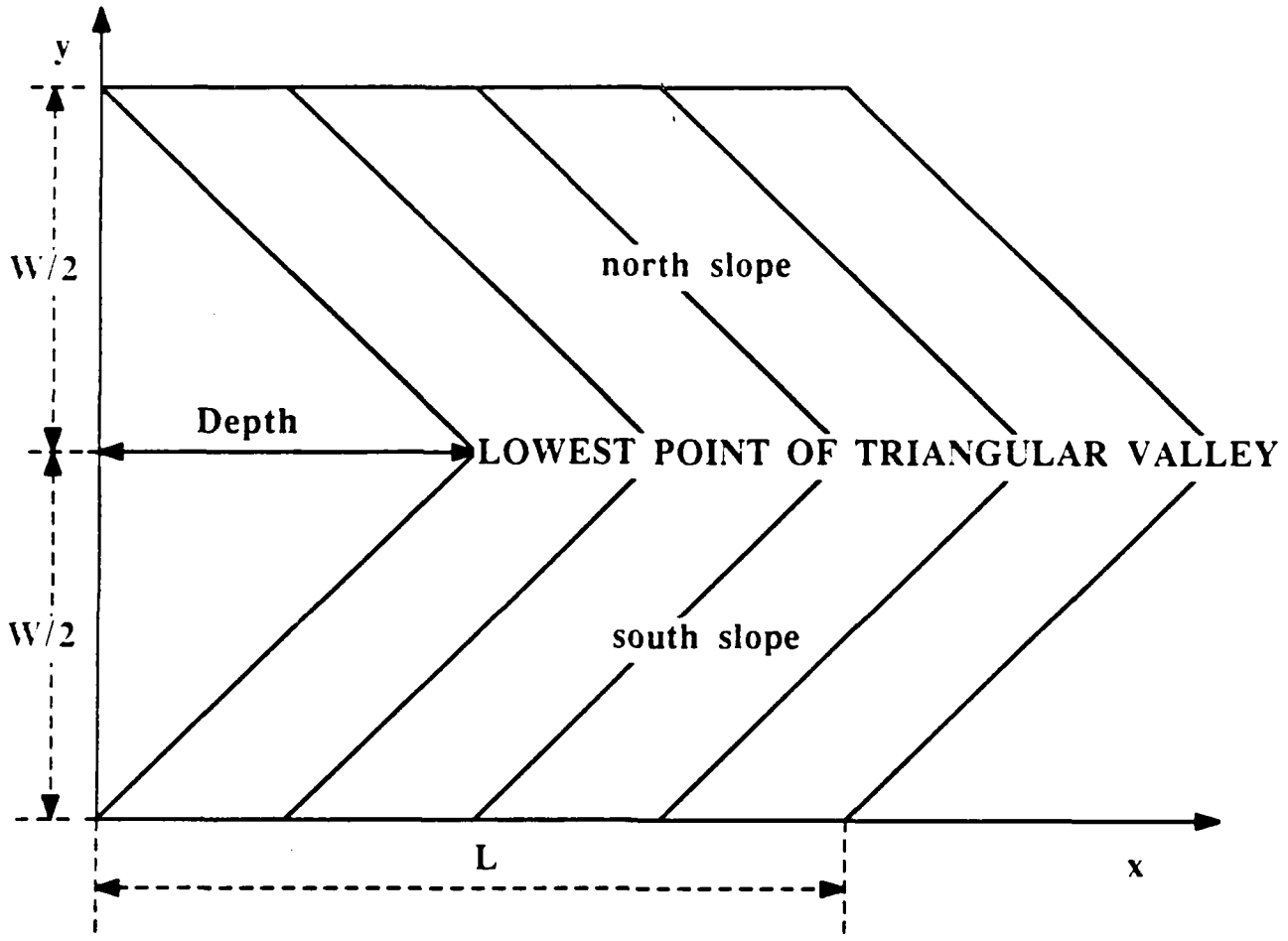


Fig. 7.3 As in Fig. 7.2, except for the case of triangular valley.

the case is, the following relationship holds:

$$s_1 = -s_2, \quad (7-1)$$

where s_1 is assumed to be greater than or equal to zero for most of the cases.

B. RESULTS I

We integrate the forecast equations over a time interval of 96 hours, and we plot the results every 48 hours. Our first concern is to examine the case of no topography. In this particular case I, the peak of the triangular mountain is zero, and both slopes, s_1 and s_2 , are equal to zero as we can see from Table V. The initial conditions are almost purely geostrophic as clearly illustrated in Fig. 7.4. The integration produces forecast fields almost identical to the initial fields, as shown in Figs. 7.5, and 7.6. That is expected, since no topographic or beta effect is involved. If we now increase slightly the magnitude both of s_1 and s_2 , as shown in Table V for case II, the 48 hour integration does not show any significant change in the forecast fields, as we can see in Fig. 7.7. However, the 96 hour integration yields a very small tendency for a westward shifting valid for all the forecast fields, and for the lower part of the channel.

Our next step, case III, is to increase the peak of the mountain to 163.1 m. In both the 48, and 96 hour integrations, a tendency for the lower

	Peak (ϕ)	Peak (z)	Slope (south)
case I	0.0	0.0	0.0
case II	400.0	40.8	0.0000167
case III	1600.0	163.1	0.0000666
case IV	4800.0	489.3	0.0001999
case V	- 400.0	- 40.8	- 0.0000167
case VI	- 1600.0	- 163.1	- 0.0000666
case VII	- 4800.0	- 489.3	- 0.0001999

Table V Peak (in geopotential meters and in meters), and south slope values for cases I through VII.

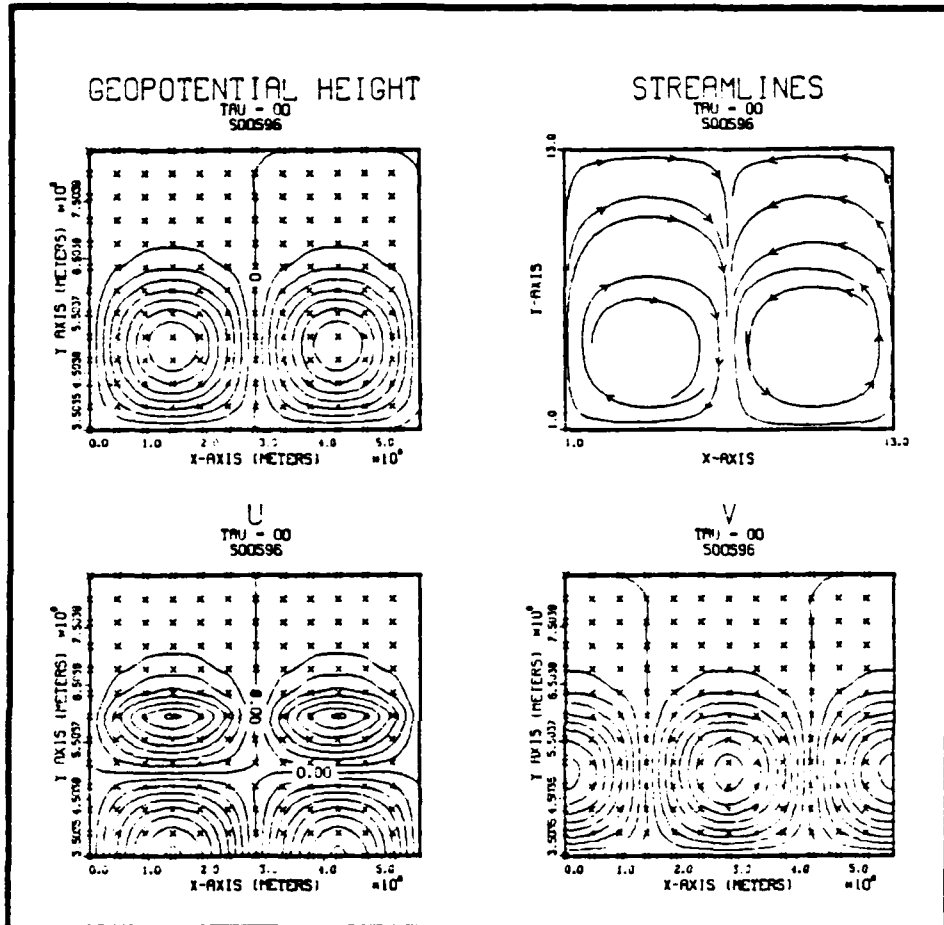


Fig. 7.4 Initial conditions for experiment I (cases I through VII). Contour intervals are $600 \text{ m}^2/\text{s}^2$ for geopotential height, and 0.2 m/s for u and v . Nodal points are denoted by an x.

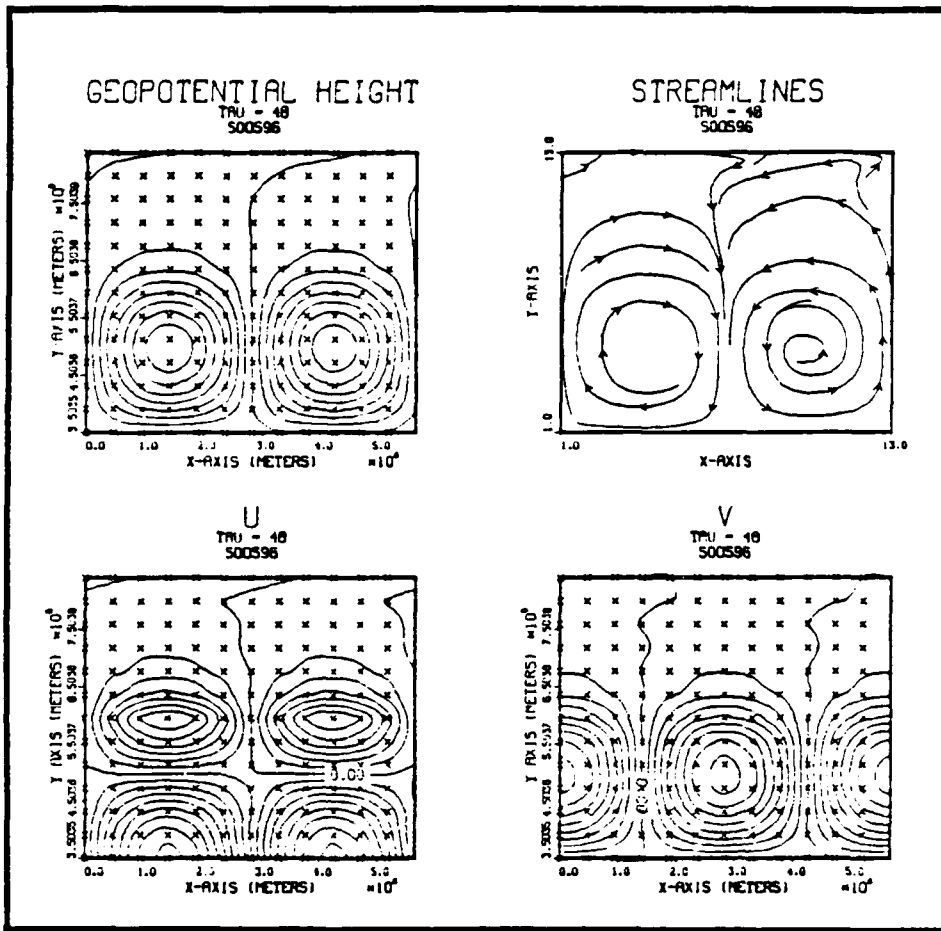


Fig. 7.5 As in Fig. 7.4, except for case I, and a 48 hour integration.

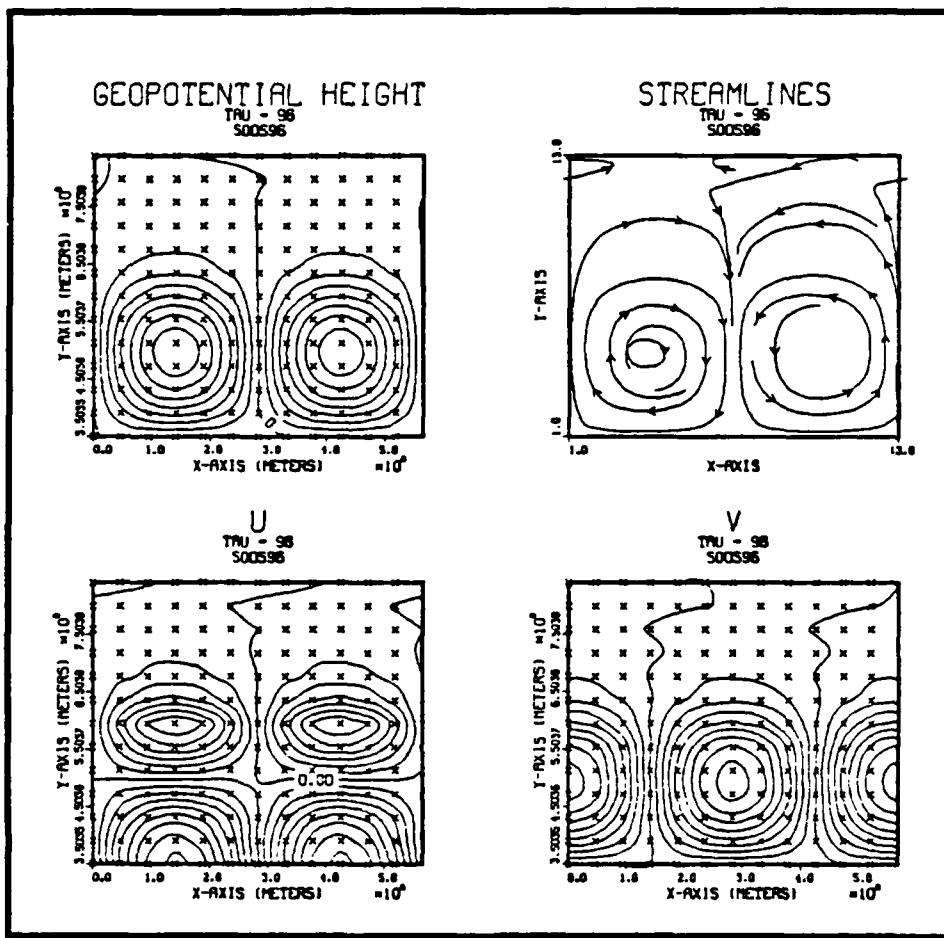


Fig. 7.6 As in Fig. 7.5, except for a 96 hour integration.

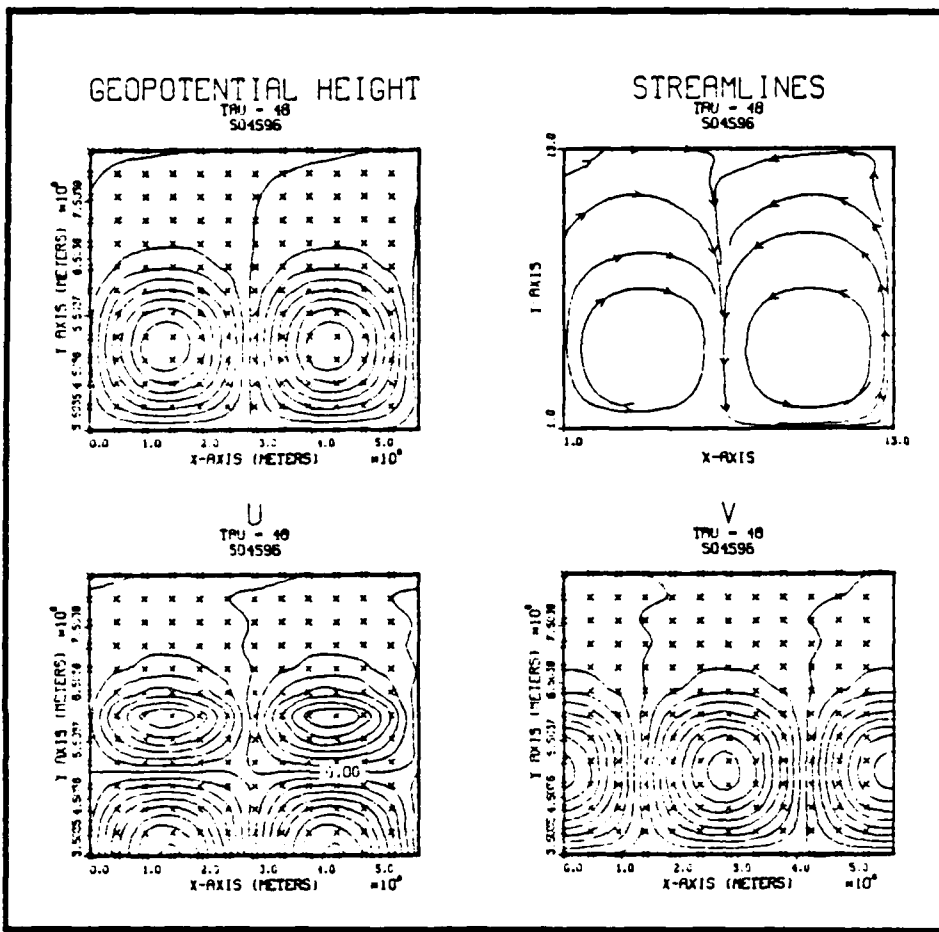


Fig. 7.7 As in Fig. 7.5, except for case II.

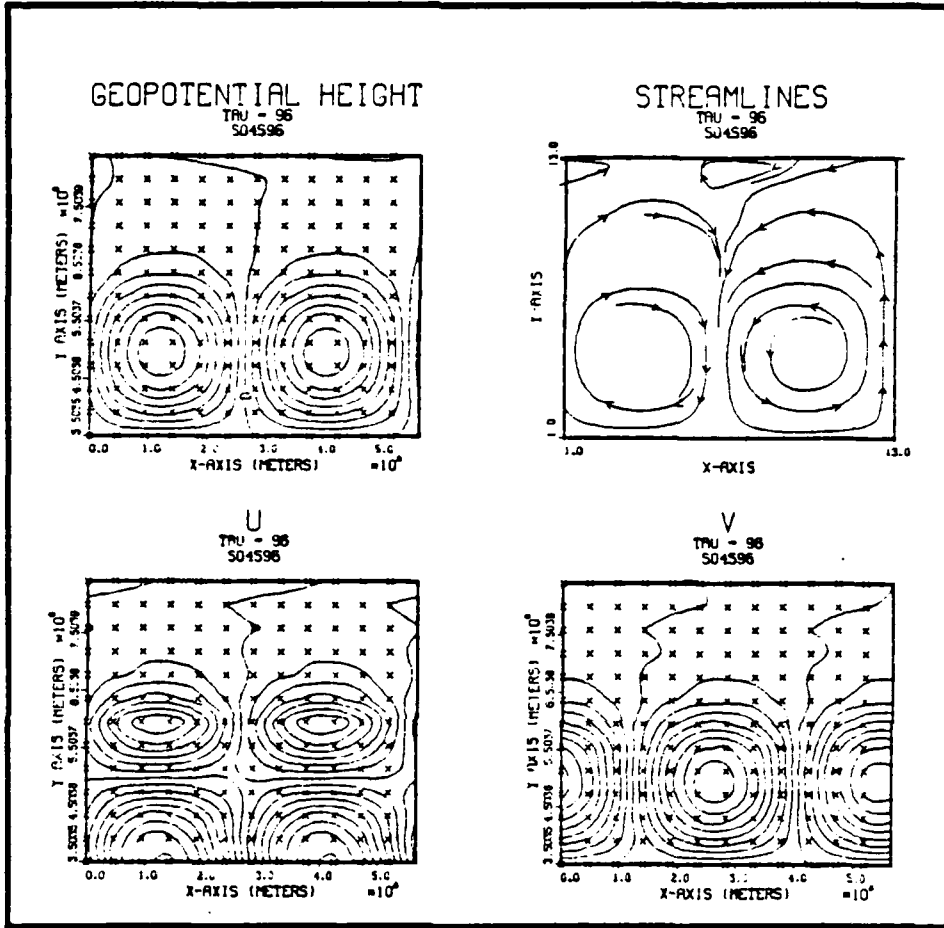


Fig. 7.8 As in Fig. 7.6, except for case II.

part forecast fields for a westward shifting is clearly noticed, as well as a small tendency for eastward shifting corresponding to the upper part fields (Figs. 7.9, and 7.10). In case IV, which is our last case of positive south slope s_1 , we increase the peak of the mountain to 489.3 m. This value corresponds to almost the half of the mean depth value considered for our shallow water approximations. In both the 48, and 96 hour integration it is very evident the significant westward sifting of the forecast fields for the lower part of the channel, and the eastward shifting of the same fields, characterizing the upper part, as we can see in Figs. 7.11, and 7.12. The results obtained here, will be compared quantitatively with the corresponding analytical values.

At this stage we wish to examine cases V, VI, and VII, all having negative south slopes. The above mentioned cases correspond to cases II, III, and IV, but with exactly opposite sign slopes. We can visualize the whole setting here as if we placed reverse triangular mountains (valleys) of different heights with their lowest points centered in the middle of the width of the channel, and their peak values always to be given by negative values. The 48 hour integration results for case V do not show any significant change in the forecast fields, as we can see in Fig. 7.13, while the 96 hour integration yield a very small tendency for a eastward shifting valid for all the forecast fields, and for the lower part of the channel (Fig. 7.14). In case VI, the valley is 163.1 m deep in the center. In both the 48, and 96 hour integrations, a tendency in the lower part forecast fields

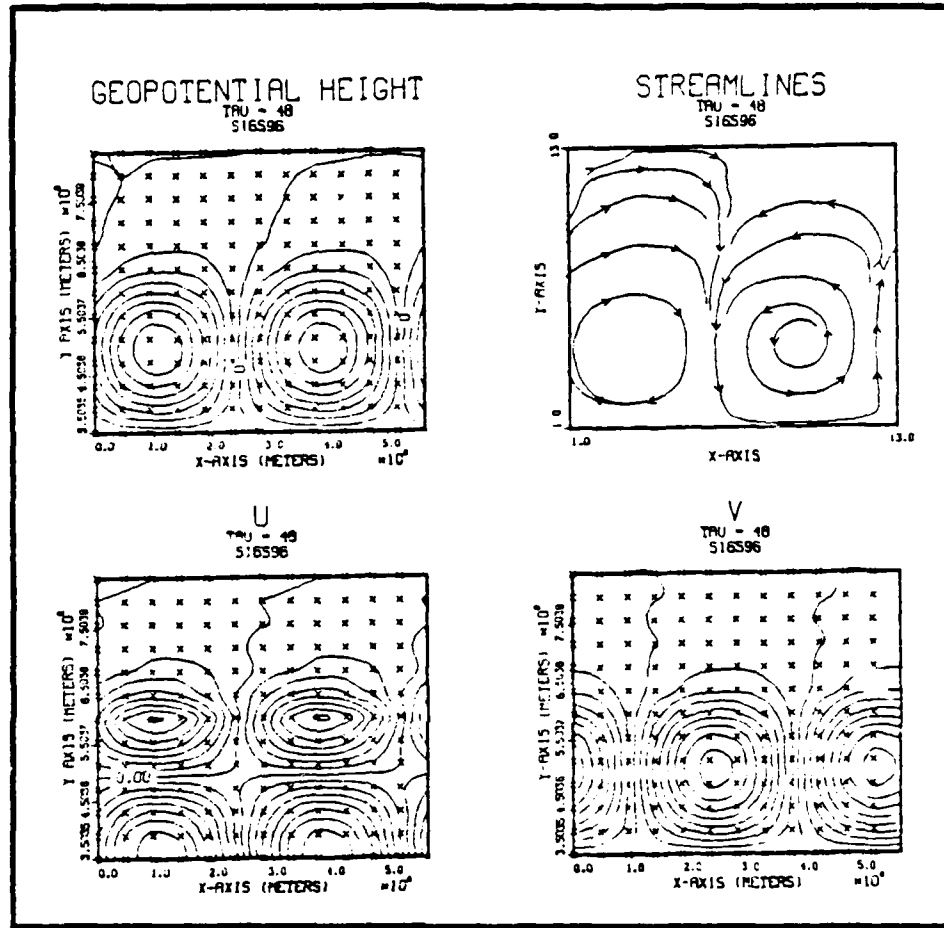


Fig. 7.9 As in Fig. 7.5, except for case III.

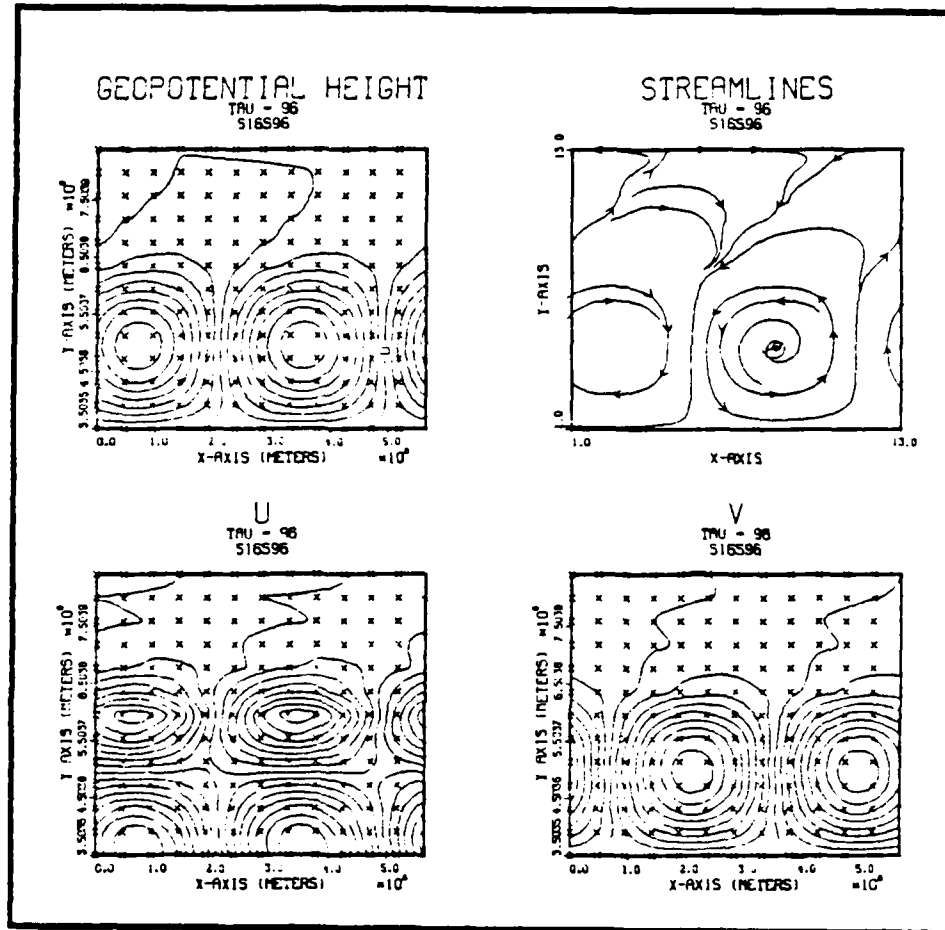


Fig. 7.10 As in Fig. 7.6, except for case III.

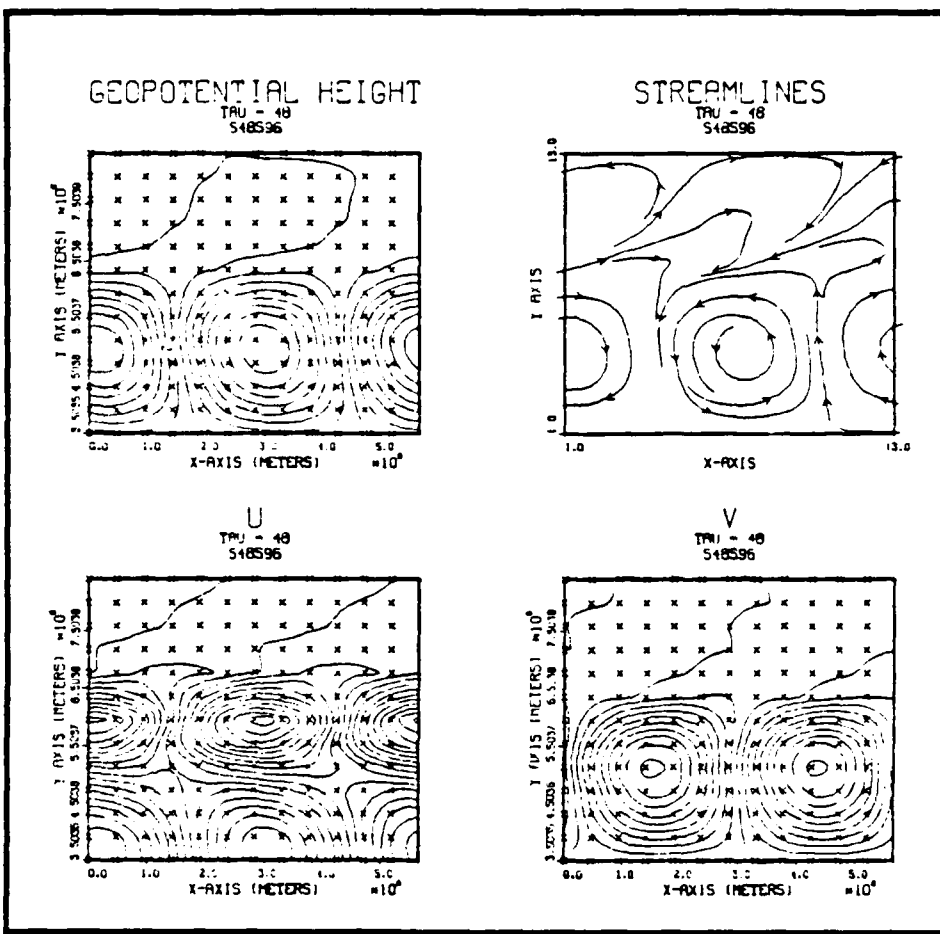


Fig. 7.11 As in Fig. 7.5, except for case IV.

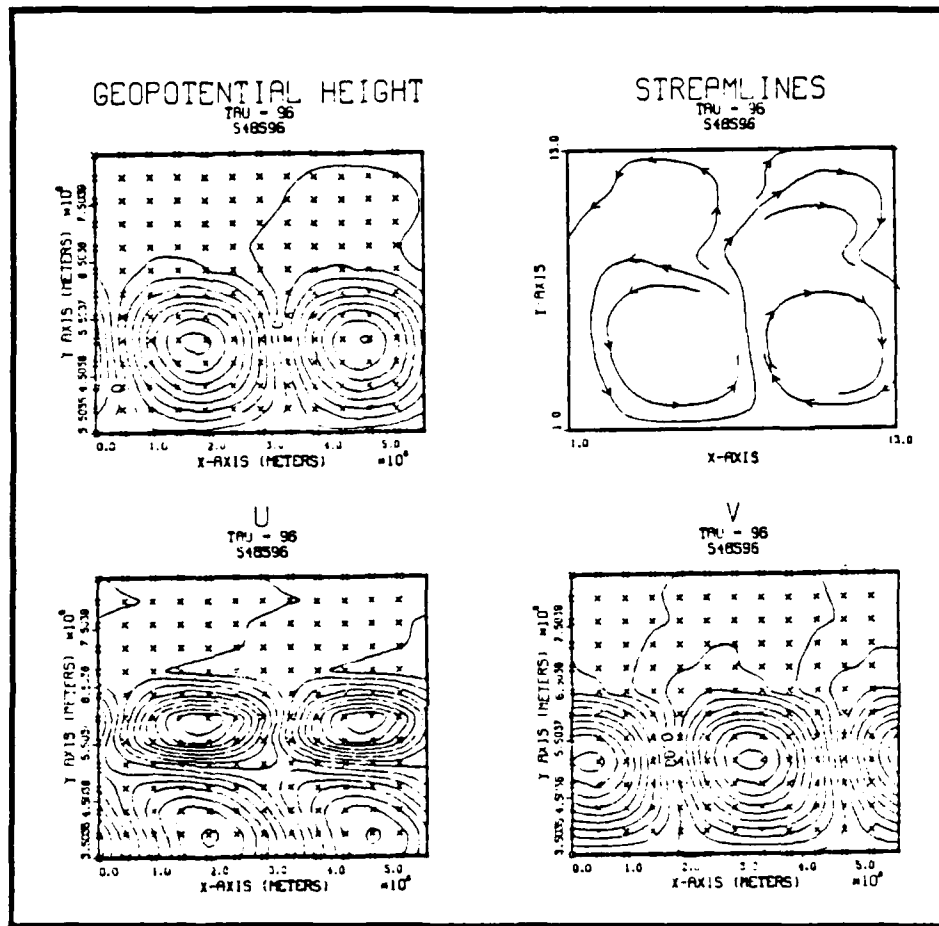


Fig. 7.12 As in Fig. 7.6, except for case IV.

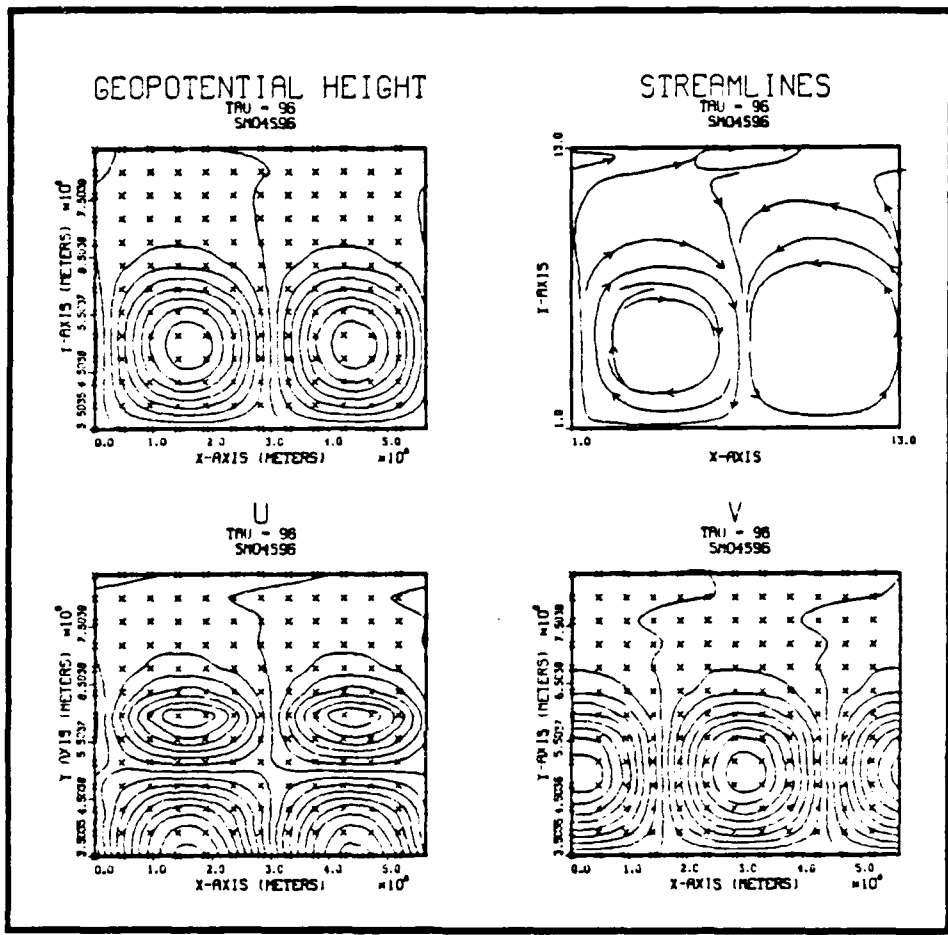


Fig. 7.13 As in Fig. 7.5, except for case V.

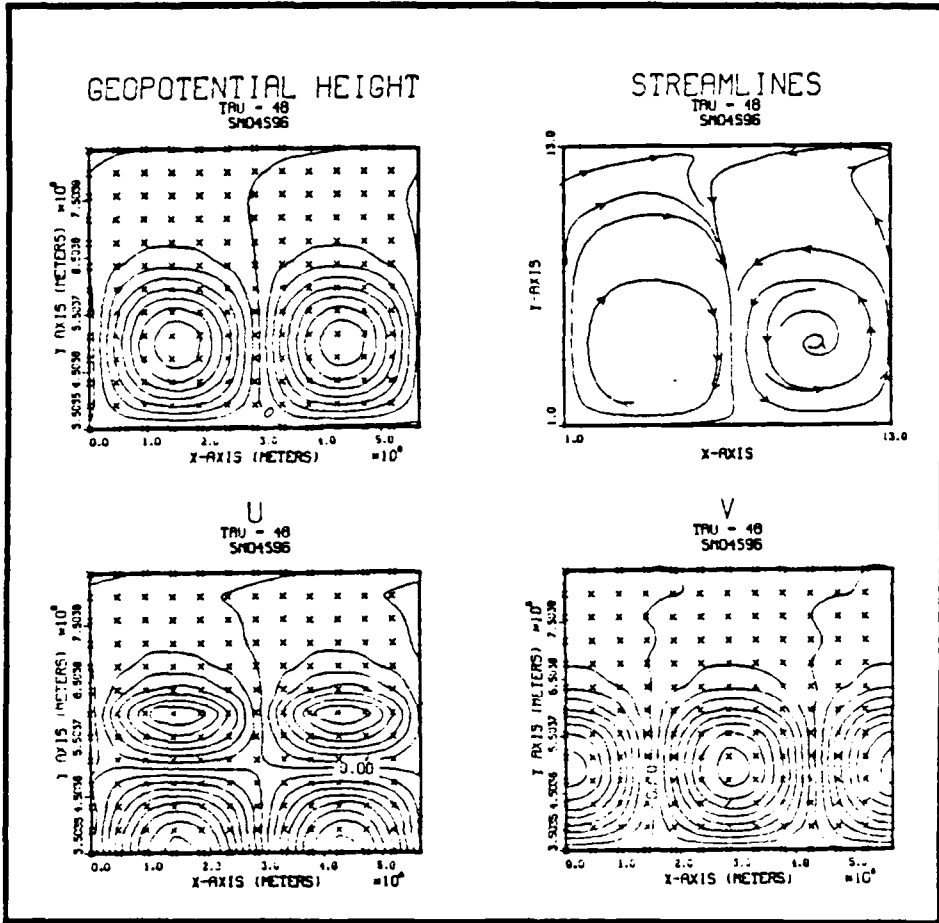


Fig. 7.14 As in Fig. 7.6, except for case V.

for a eastward shifting is evident, as well as a small tendency for westward shifting corresponding to the upper part fields (Figs. 7.15, and 7.16). The same tendency becomes more evident in both the 48, and 96 hour integration, i. e., the significant westward sifting of the forecast fields for the the lower part of the channel, and the eastward shifting of the corresponding upper fields, as it is clearly shown in Figs. 7.17, and 7.18.

At this point, we strongly believe that there is a certain link between the presence of topography and the observed shifting in all the forecast fields, because no shifting at all is been observed in the flat case of no topography. That specific link has to be the topographic Rossby wave whose existence requires the topographic effect in a rotating system (with constant f). The reason is that the Rossby wave in general, can exist only in the presence of an ambient potential-vorticity gradient. In case I, of course, no potential-vorticity gradient is present, and that is why we do not observe any sign of the Rossby wave. In case II, III, and IV, the positive y-direction (shown in Fig. 7.19), is also the direction of increasing ambient potential-vorticity. If we consider a fluid column initially at rest, but later to be displaced in the positive y-direction, then in order to conserve its total potential-vorticity, the wave potential-vorticity $\zeta_0 - F\eta_0$, has to be decreased. This will balance the excess of the ambient potential vorticity in its new place. There are two ways for this to be accomplished.

a. The fluid will have a tendency to be squeezed, since its new position appears to be shallower than the previous one. This will induce the

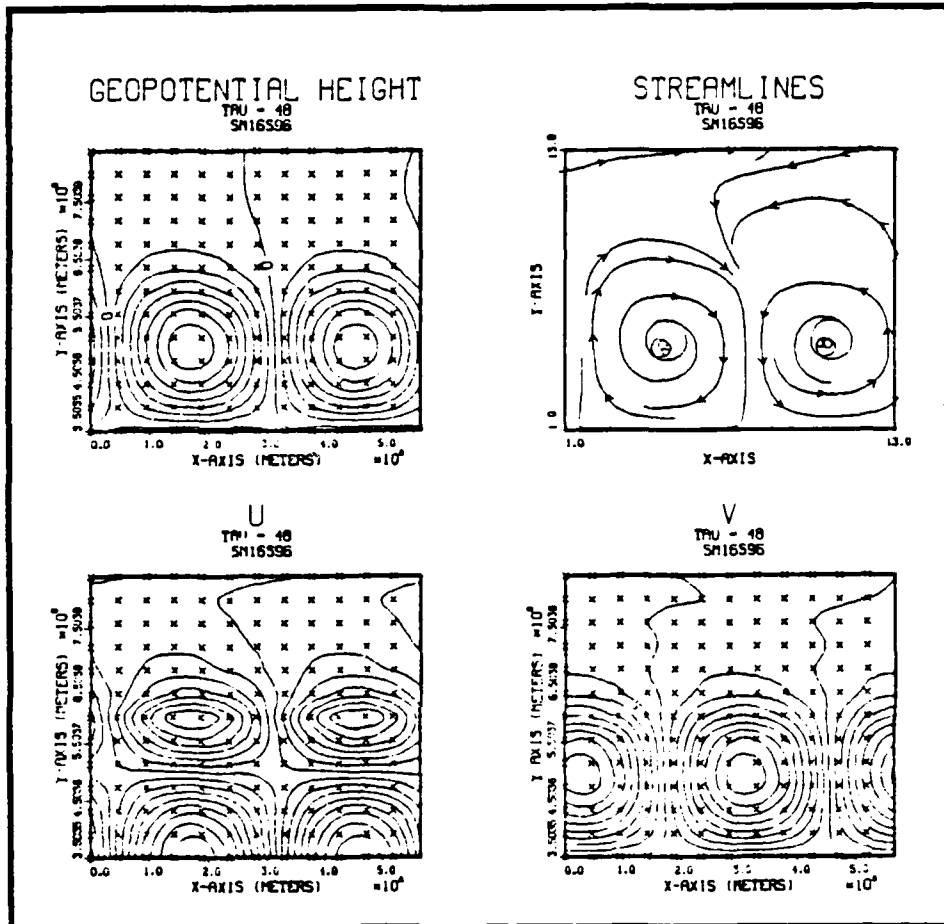


Fig. 7.15 As in Fig. 7.5, except for case VI.

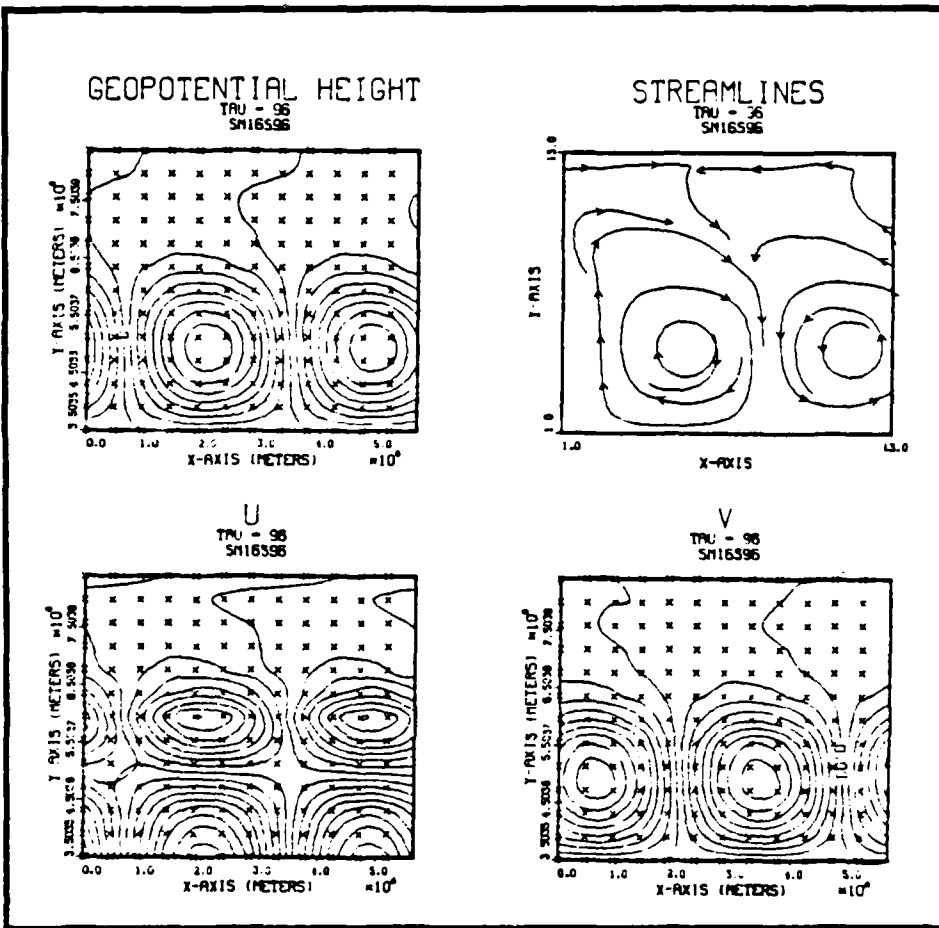


Fig. 7.16 As in Fig. 7.6, except for case VI.

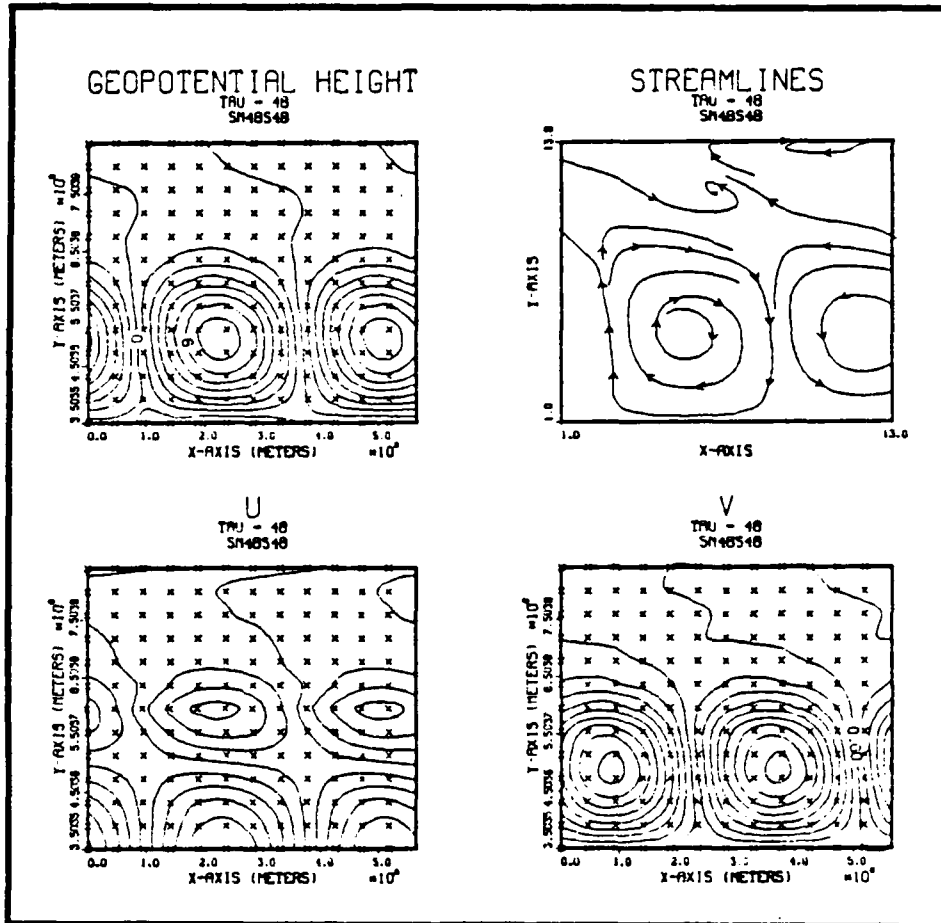


Fig. 7.17 As in Fig. 7.5, except for case VII.

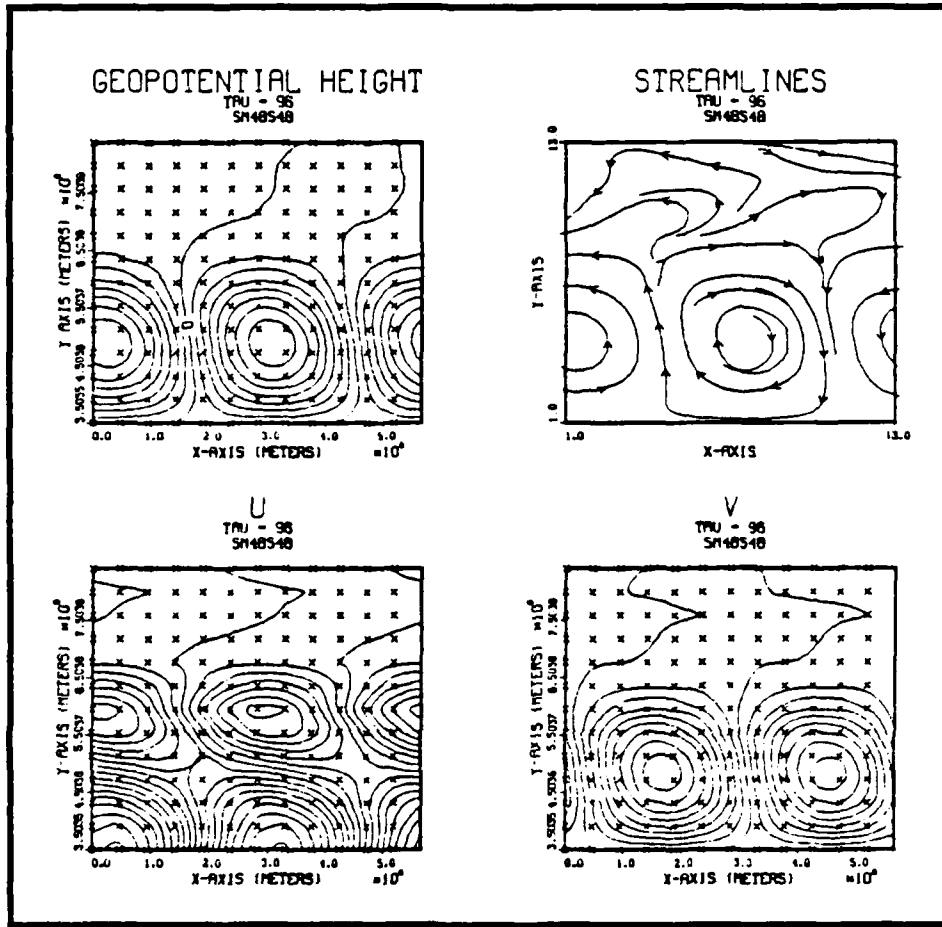


Fig. 7.18 As in Fig. 7.6, except for case VII.

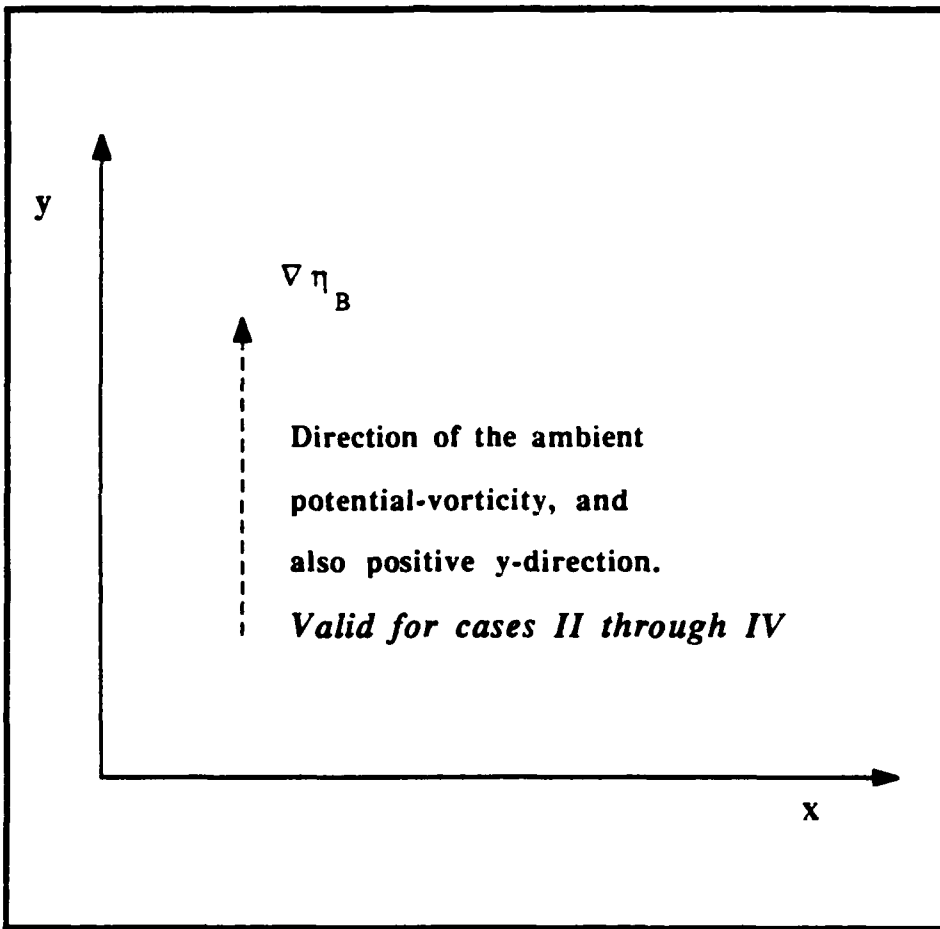


Fig. 7.19 The required ambient potential-vorticity gradient. A clue for the physical explanation of the topographic Rossby wave oscillation.

production of negative vorticity due to the vortex-tube compression.

b. The act of the squeezing can not be complete, since the upper surface is not restricted or bounded. In this case the column will have a tendency to ride at least partially up, the slope resulting in a greater value of η_0 in its new position than its neighbors.

It is important here to note that both effects, $\zeta_0 < 0$, and $\eta_0 > 0$, act to reduce the quantity $\zeta_0 - F\eta_0$. Both effects also, will result in a clockwise circulation in the fluid around the column. The clockwise circulation in the fluid column C, will force the adjacent column to its right, R, into deeper fluid, and the adjacent column to the left, L, to be squeezed into shallower fluid, as shown in Fig. 7. 20. The column R, will become the center of a counter-clockwise circulation, while column L, will become the center of a clockwise circulation. Both contributions from columns L, and R, will force the return of column C, toward its original position. This will result in an overshoot due to the column C inertia, and the oscillation will continue. This is a very simplified view of the phenomenon but it clearly shows a very important aspect. The strength of the restoring mechanism depends on the vigor of the circulation induced on neighboring fluid columns by the displaced column. Following the same approach, in cases V, VI, and VII, the positive y-direction is the direction of decreasing ambient potential-vorticity, and everything described above applies in the opposite sense.

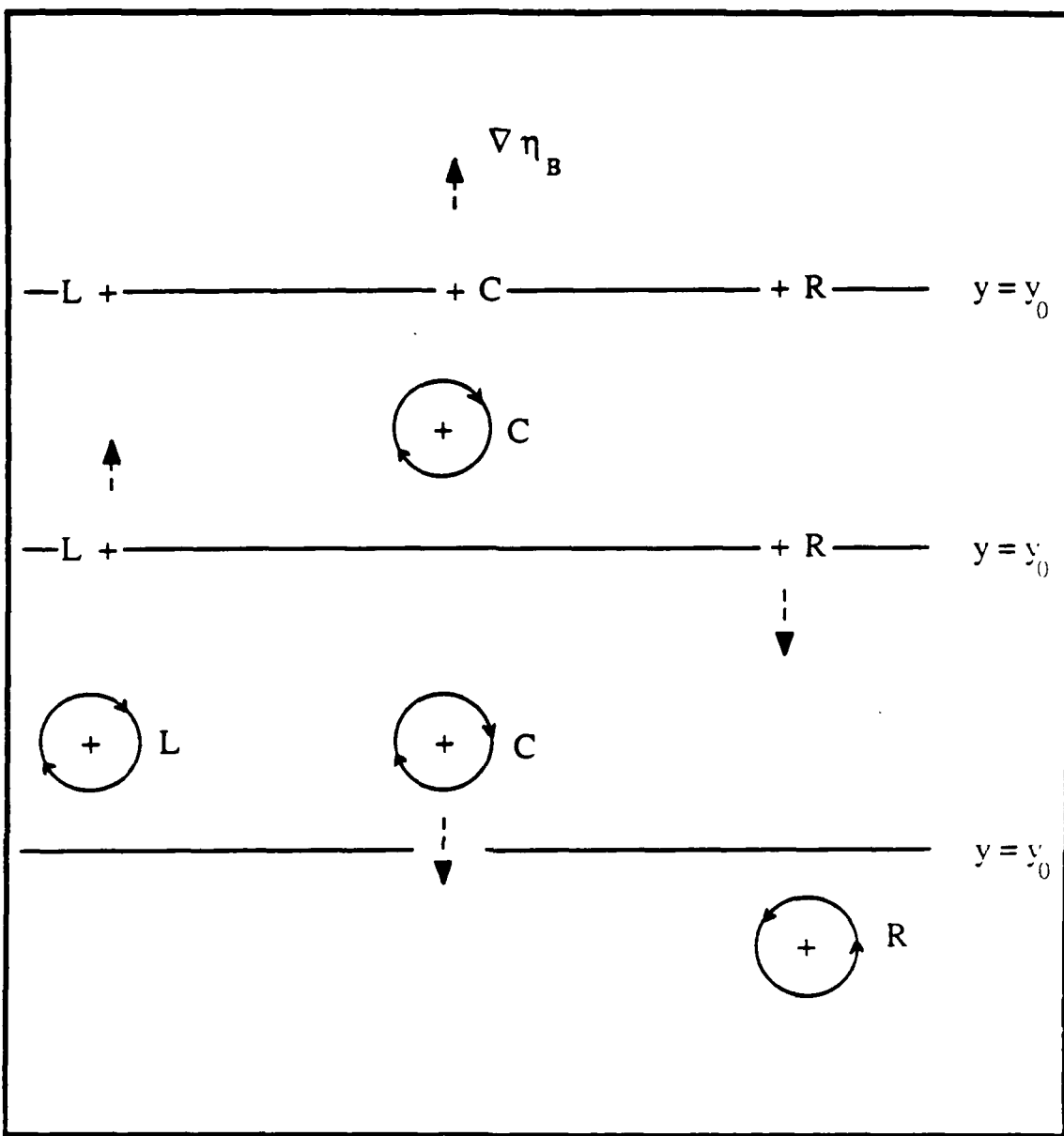


Fig. 7.20 The position of the three-point vortices L, C, and R at three successive times. Initially collinear and positioned along an isobath, C is displaced upwards, producing velocities at L and R which move them as shown. The vorticity induced on L and R produces a velocity at C with a tendency to restore it to its original position.

From a purely theoretical point of view, if we recall equation (3-47) we can easily find out that for positive values of slope s the phase speed in the x -direction is always negative or, referring to our case, westwards. For the opposite case of negative values of s , the propagation of the Rossby wave in the x -direction is always positive or eastwards. Also, from the same equation (3-47), it is obvious that for increasing values of s (in magnitude), the propagation phase speed also increases. In other words, if we keep increasing the peak of our triangular mountain we should expect the presence of the topographic Rossby wave to become more and more evident. In order to examine the actual phase speed in more detail, we can Fourier analyze the v -component field, and obtain the wave component phase speed every 24 hours. The observed phase speed is then given by

$$C_F = \frac{L(\phi_1 - \phi_2)}{2\pi(t_1 - t_2)}, \quad (7-2)$$

where L is the length of the channel. These phase speeds, averaged over 96 hours for cases II through VII, are given in Table VI, and in Figs. 7.21, and 7.22.

The analytic phase speed given by (3.41) can be rewritten in the following form:

	Peak (z)	C (estimated)	C (corr. fs)	C (corr. fs+H)	C (observed)
case II	40.8	- 0.72	- 0.49	- 0.49	- 0.49
case III	163.1	- 2.87	- 1.97	- 1.98	- 1.99
case IV	489.3	- 8.61	- 6.14	- 7.12	- 7.44
case V	- 40.8	0.72	0.49	0.49	0.49
case VI	- 163.1	2.87	1.97	1.85	1.74
case VII	- 489.3	8.61	6.14	5.22	4.89

Table VI Estimated, estimated corrected by the free surface term, estimated corrected by both the free surface and H terms, and observed phase speed values (in m/s), for cases II through VII.

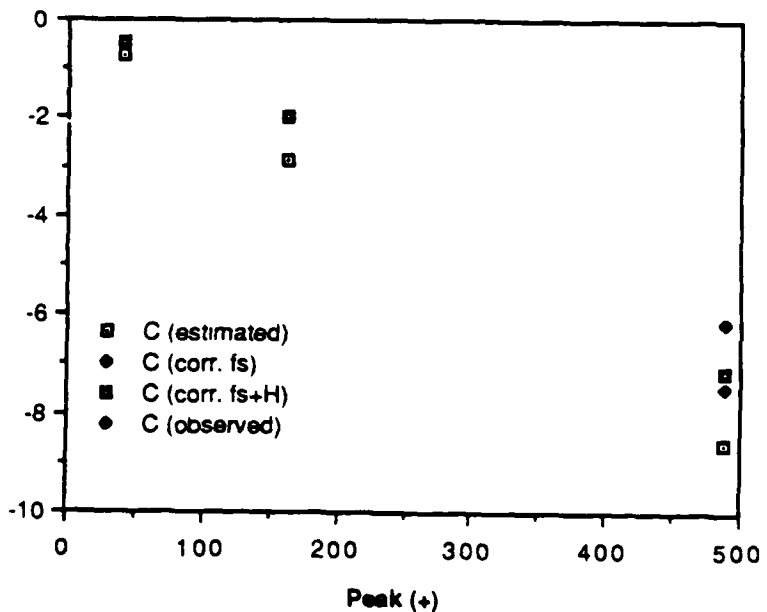


Fig. 7.21 Comparison of the observed phase speed values, with estimated, estimated corrected by the free surface term, and estimated corrected by both the free surface and H terms, phase speed values (in m/s) for cases II through IV (scatter diagram).

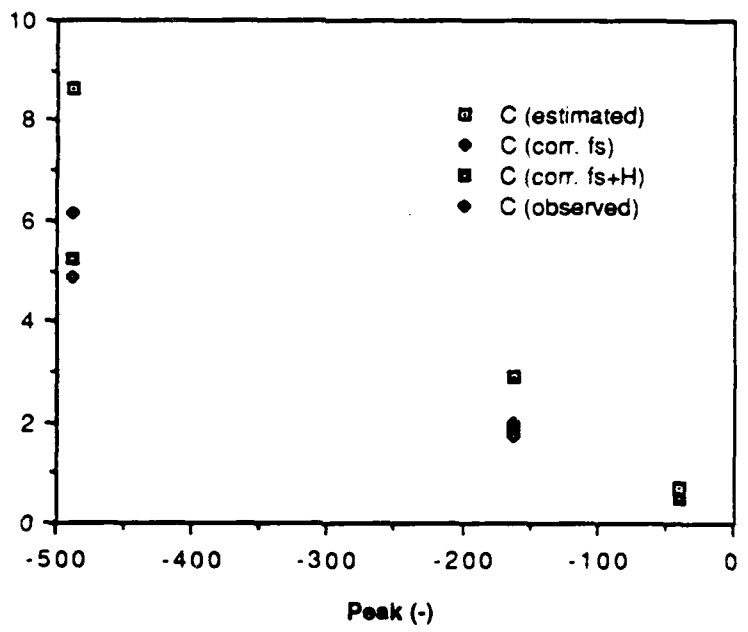


Fig. 7.22 As in Fig. 7.21, except for cases V through VII.

$$C = \frac{-f_0 \frac{1}{H} \frac{h_m}{W}}{\frac{\mu_1^2 + \lambda_1^2}{W^2}}, \quad (7-3)$$

where h_m is the mountain height, and the term $[(\mu_1)^2 + (\lambda_1)^2]$ is non-dimensional. The analytic phase speeds resulting from (7-3) are also given in Table VI.

In general, the analytic phase speeds are all larger in magnitude than the corresponding model phase speeds, obtained from (7-2). The reason why this happens is that the analytic theory developed here is based on a rigid upper lid, but at the same time, the GFEM model used for our forecasts has an upper free surface. If we wish to include the upper free surface effect in equation (7-3), the term $[(f_0)^2 / gH]$ must be added to the denominator, resulting in

$$C = \frac{-f_0 \frac{1}{H} \frac{h_m}{W}}{\frac{\mu_1^2 + \lambda_1^2}{W^2} + \frac{f_0^2}{g H}}, \quad (7-4)$$

where H represents the mean depth value.

The value of the new added term is about the half of the denominator value, so that it will reduce the analytic phase speed value by around 30%, which would bring C and C_F , into more agreement for most of the cases. However, the highest mountain peak case, case IV, or the lowest depth valley case, case VII, can not be satisfied by only considering this change. The above mentioned agreement could be improved for case IV, by using a smaller H value into (7-4), since the true average depth in this case is less than 1 km. Using the same arguments for case VII, the improvement of the desired agreement could be accomplished by using a larger H value into (7-4), since the true average depth in this last case is greater than 1 km.

Table VI and Figs. 7.21, 7.22, 7.23, and 7.24, compare the observed phase speeds with the various theoretical estimates. As expected, each new correction improves the agreement with the model phase speed. The phase speed for the shallower topography are extremely accurate. The reason for the lack of agreement for larger H values is due to the uncertainty for what the correct value of H is to use in equation (7-4). Therefore, for higher values of the bottom topography the error is larger because using the correct value of H in equation (7-4) is most important. Clearly, experiment I shows that our numerical model is able to handle the topographic Rossby wave case extremely well.

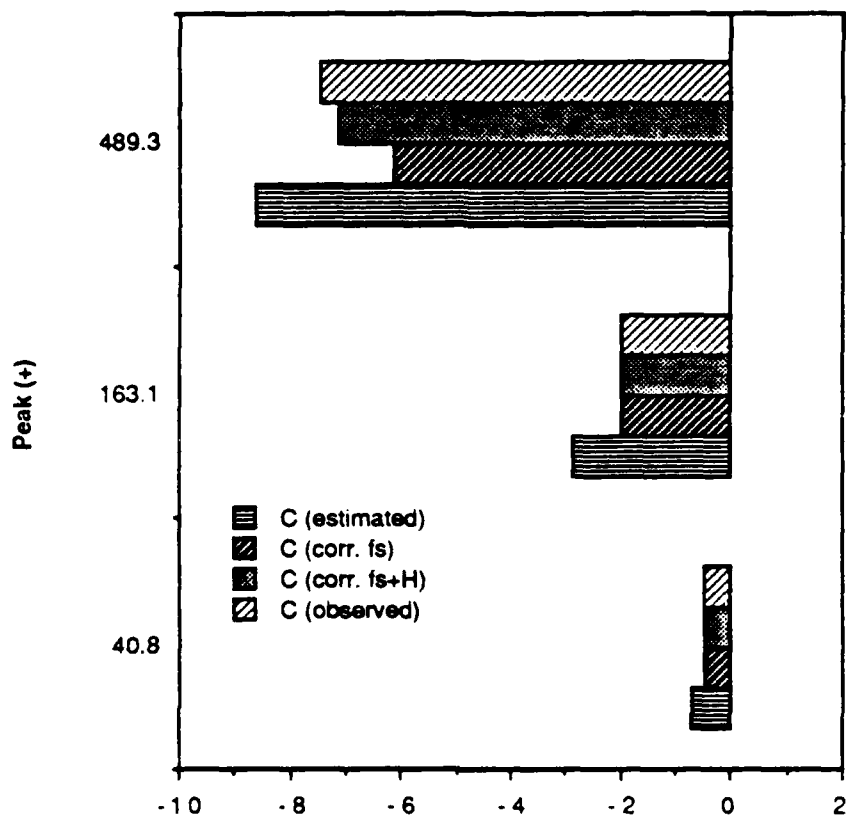


Fig. 7.23 As in Fig. 7.21, except for bar representation.

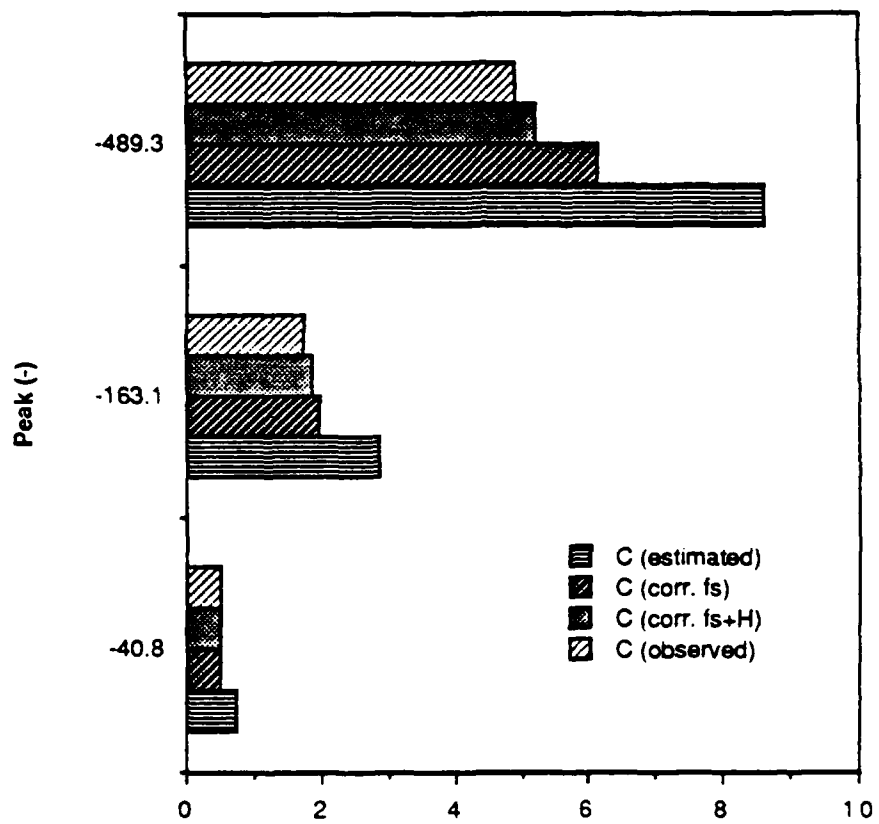


Fig. 7.24 As in Fig. 7.22, except for bar representation.

C. EXPERIMENT II

We perform experiment II using the same GFEM rectangular model, as in experiment I, the only difference is in the resolution of the model. The model now has 24 increments in the x- and y- directions which gives the model 576 degrees of freedom. The domain of integration is 727.6 km in the x-direction, and 630.1 km in the y-direction. The value of Coriolis parameter is taken to be zero for all of the cases, corresponding to a nonrotating system.

The initial conditions for experiment II are described in Chapter VI. The boundary conditions in x are chosen to be periodic once more, that is

$$u(0) = u(L), \quad (7-5)$$

$$\phi(0) = \phi(L). \quad (7-6)$$

These boundaries at $x = 0$, and $x = L$, are placed sufficiently far from the ridge so that the desired asymptotic conditions are well established in the vicinity of the ridge before wave motions are able to be fed back into this region by the periodic boundary conditions. The height profile of the orographic ridge is given by

$$h_M = \begin{cases} H_M \sin^2\left(\frac{\pi x}{Z}\right) & \text{for } 0 \leq x \leq Z, \\ 0 & \text{elsewhere,} \end{cases} \quad (7-7)$$

where Z is the width and H_M the height of the mountain, as shown in Fig. 7.25.

D. RESULTS II

We integrate the forecast equations over a maximum time interval of 50.6 minutes and we plot the results at $t = 5.6, 16.9, 28.1, 39.4$, and 50.6 minutes. The five distinct cases we run (I through V), are summarized in Tables VII and VIII. Cases III and IV are expected to produce a hydraulic jump because they lie in domain II (see Fig. 4.5). In each case the equations are integrated from an initial state where u and h are both uniform. The u -field for case I is shown in Fig. 7.26. It clearly shows the rapid development of a speed maximum over the center area of the mountain and slightly on the lee side. A secondary speed maximum also forms over the ridge area and it moves upstream with time. The ϕ -field, shown in Fig. 7.27, indicates the earlier development of low pressure-field over the lee side of the ridge. The high pressure-field over the east part of this pattern has an obvious tendency to move upstream with time. Since the main feature of the flow, the speed maximum over the center area of the mountain, is quite stable we regard this as a no-jump case in agreement with the theory presented before in chapter IV. The u -field for case II, a case with slightly higher mountain, and stronger mean flow, shown in Fig. 7.28, is generally similar to case I except that the perturbation now represents a larger fraction of the mean flow. The same arguments appear

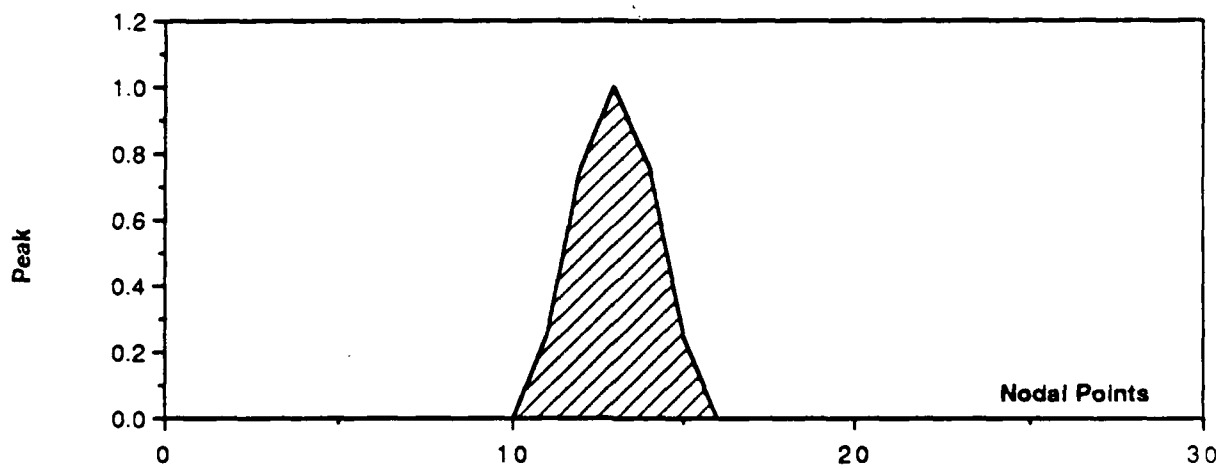


Fig. 7.25 Schematic representation of the position of bottom topography along x-axis, valid for each node per horizontal row, for the hydraulic jump case (experiment II).

	F_0	R	F	H (m)	U (m/s)	D
case I	0.2	0.1	1.010	1000.0	19.80	I
case II	0.4	0.2	1.040	1000.0	39.60	I
case III	0.3	0.7	1.220	1000.0	29.69	II
case IV	0.8	0.2	1.149	500.0	56.00	II
case V	1.4	0.05	1.407	400.0	87.65	III

Table VII Froude number (F_0), maximum height of the ridge (R), parameter F, mean depth (H), mean flow (U), and domain (D), for cases I through V.

	F	R	D	Jump case ?
case I	1.010	0.10	I	no
case II	1.040	0.20	I	no
case III	1.220	0.70	II	yes
case IV	1.149	0.20	II	yes
case V	1.407	0.05	III	no

Table VIII Parameter F, maximum height of the ridge (R), domain (D), and classification of the asymptotic flow conditions, for cases I through V.

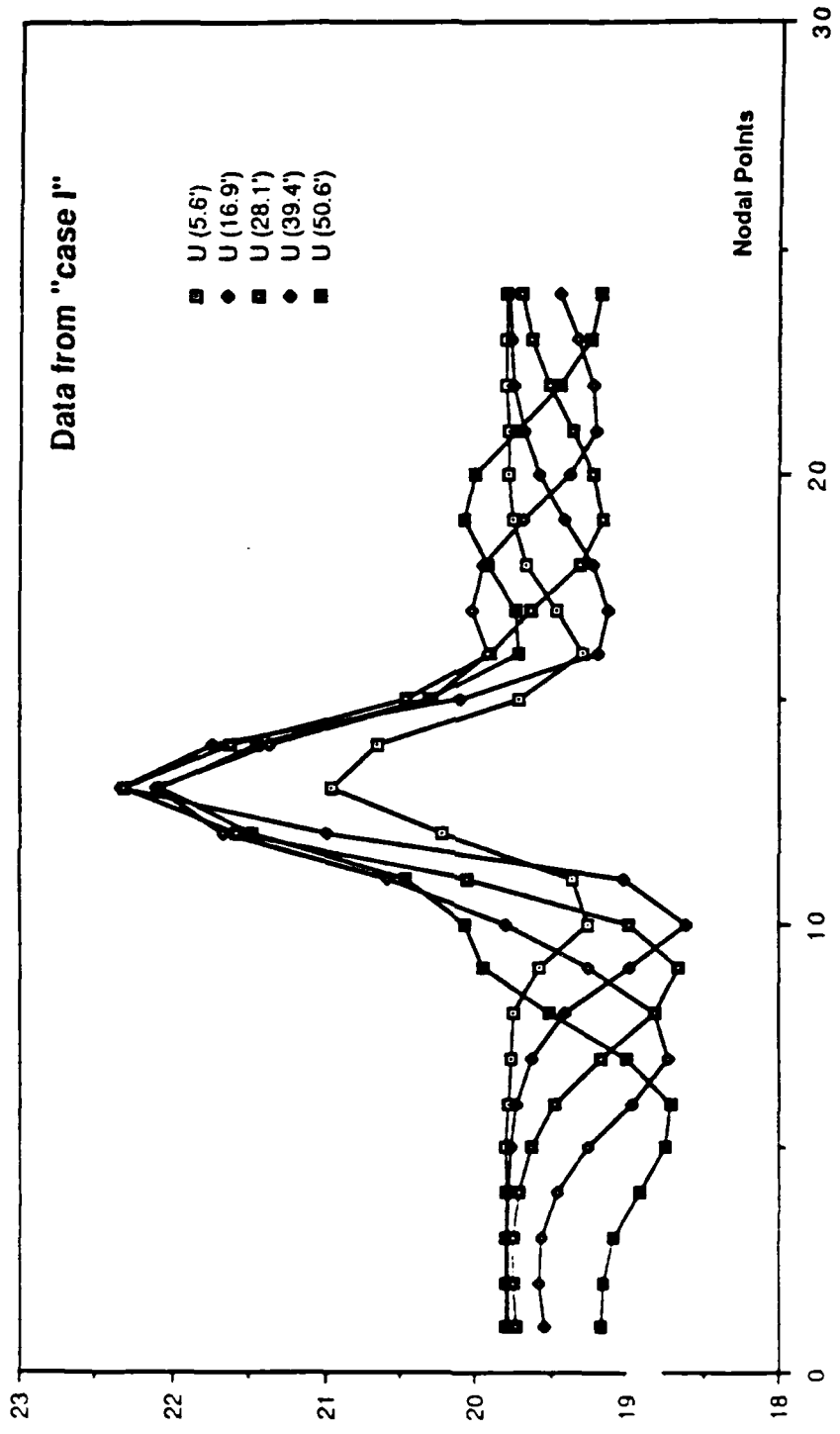


Fig. 7.26 U-component amplitude as a function of time for case I.

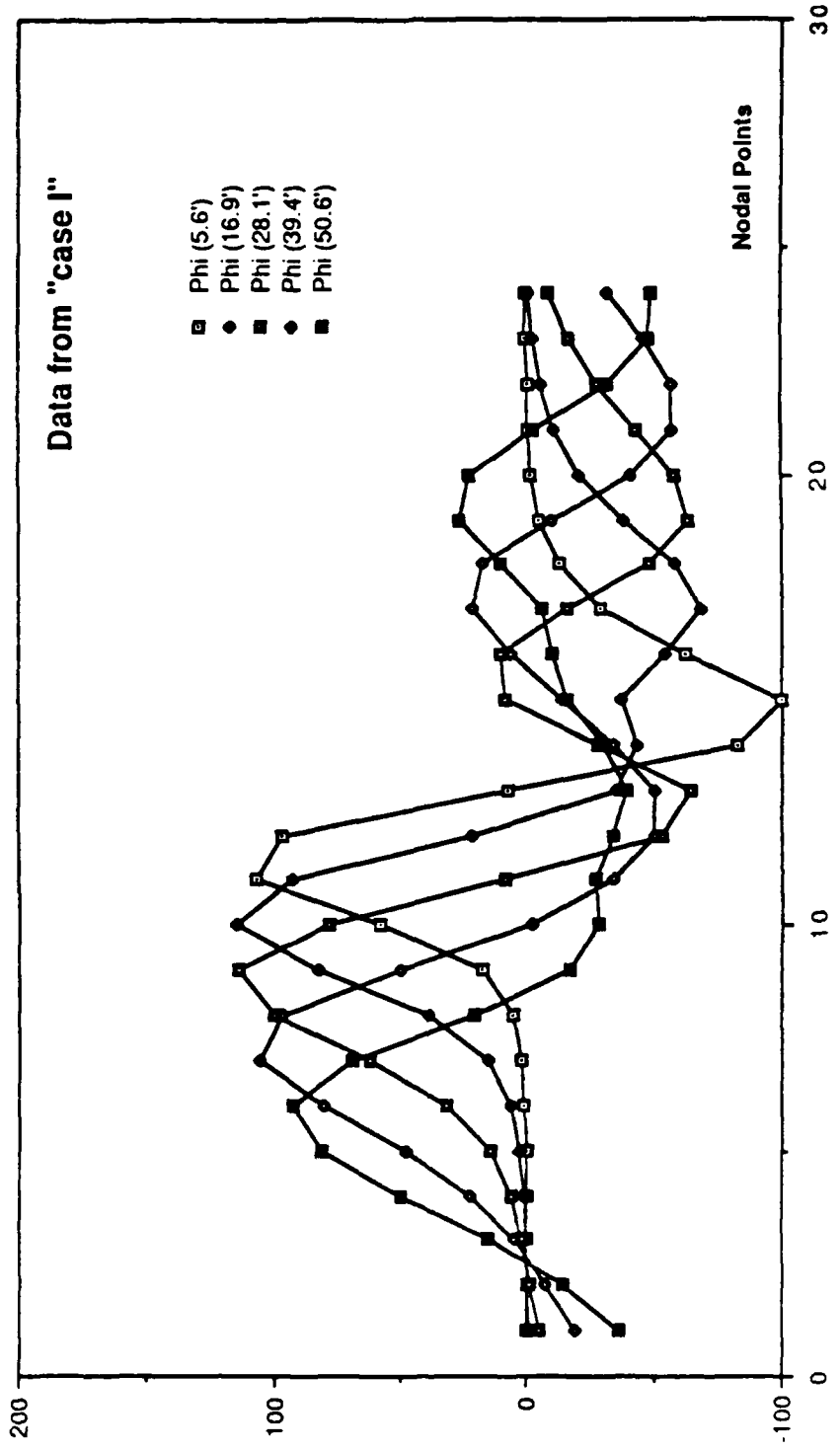


Fig. 7.27 Φ -amplitude as a function of time for case I.

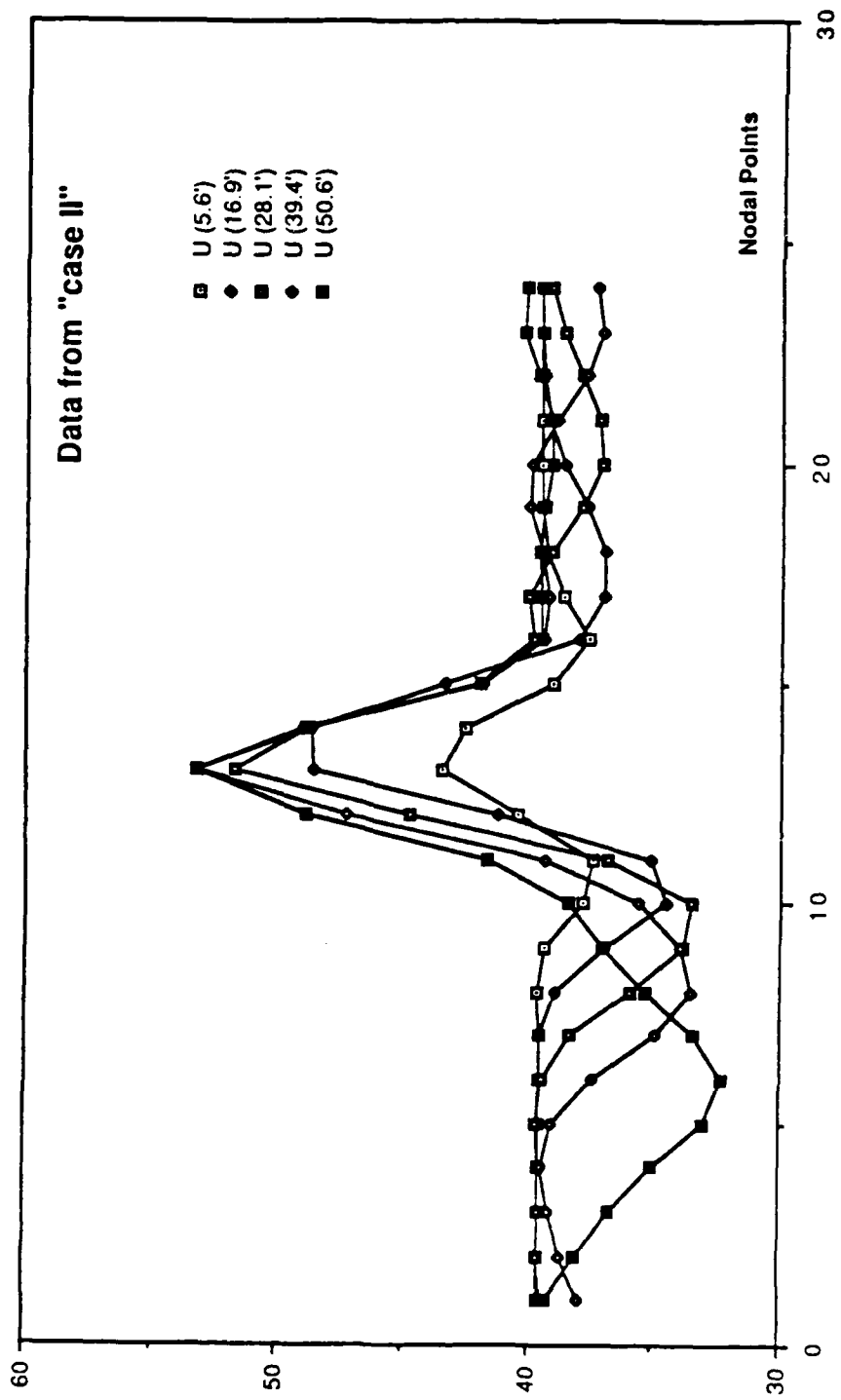


Fig. 7.28 As in Fig. 7.26, except for case II.

to be valid for the ϕ -field also, shown in Fig. 7.29. We also regard case II as a no-jump case in agreement with the theory.

The u-field for case III is shown in Fig. 7.30. In this case the wind maximum on the lee side of the mountain, continues to grow with the time. At the same time the ϕ -field, shown in Fig. 7.31, indicates that the low pressure-field centered on the lee side, changes rapidly to nearly zero. We regard case III as a jump case because it is not approaching steady state. The resolution of the model is too poor to allow a detailed description of the small-scale jump zone. The theory also indicates that this is a jump case. Fig. 7.32 contains the u-field for case IV. The ϕ -field for the same case is given by Fig. 7.33. The behavior of case IV is similar to case III, so that, this is also a jump case in agreement with the theory.

The fields of u and ϕ for case V, are shown in Figs. 7.34 and 7.35 respectively. These field patterns are similar to those of cases I and II, the only difference is a downstream shifting for both the u - and ϕ -fields. The growth in the amplitude of the curves appears to be stabilized, so that we regard case V as a no-jump case in agreement once more with the theory.

In all the investigated cases (I through V), jump formation is indicated by both u and ϕ amplitudes which continue to increase with time. In order to study the behavior of each one of the jump cases in more detail, better resolution will be required as well as a larger domain to reduce the boundary effects.

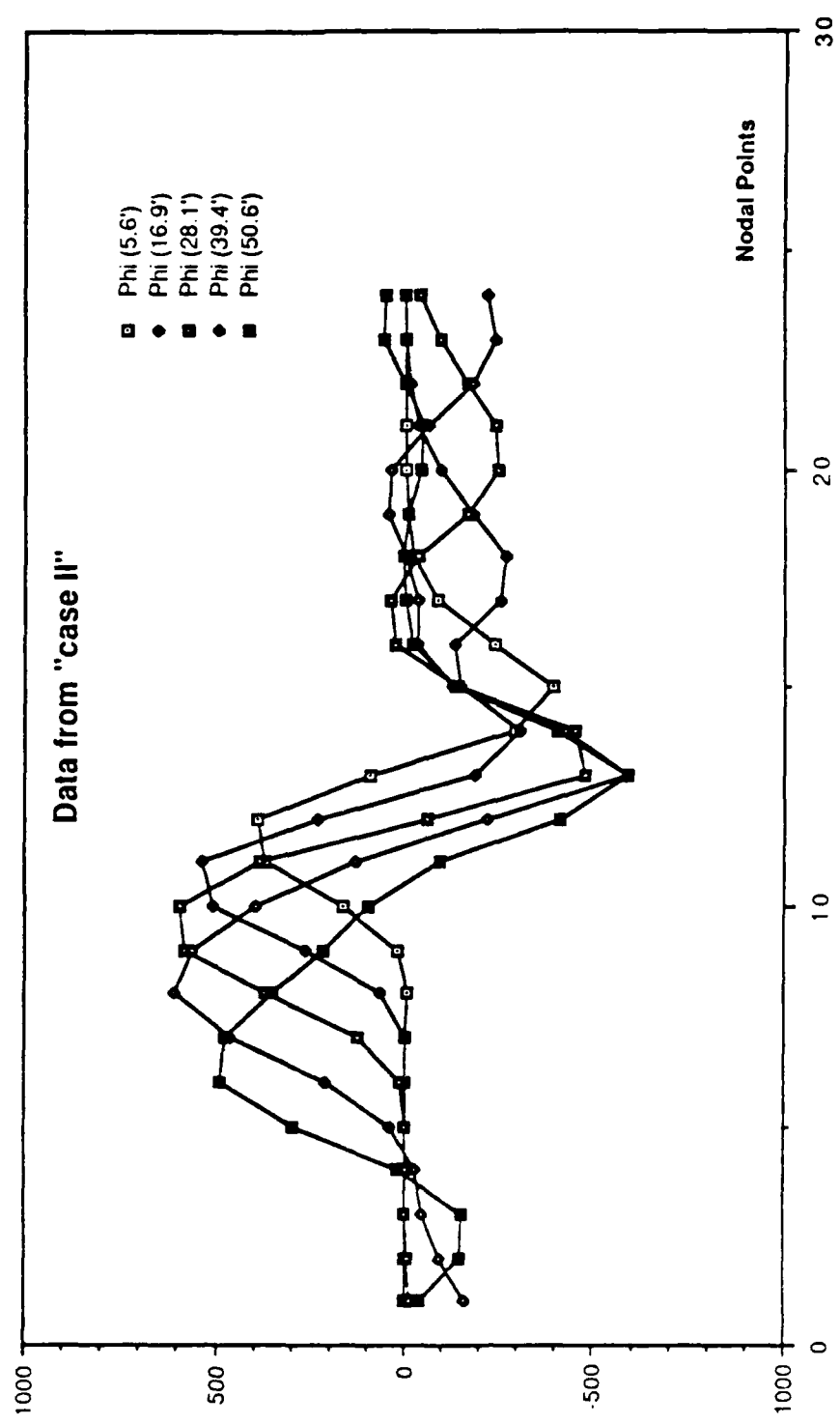


Fig. 7.29 As in Fig. 7.27, except for case II.

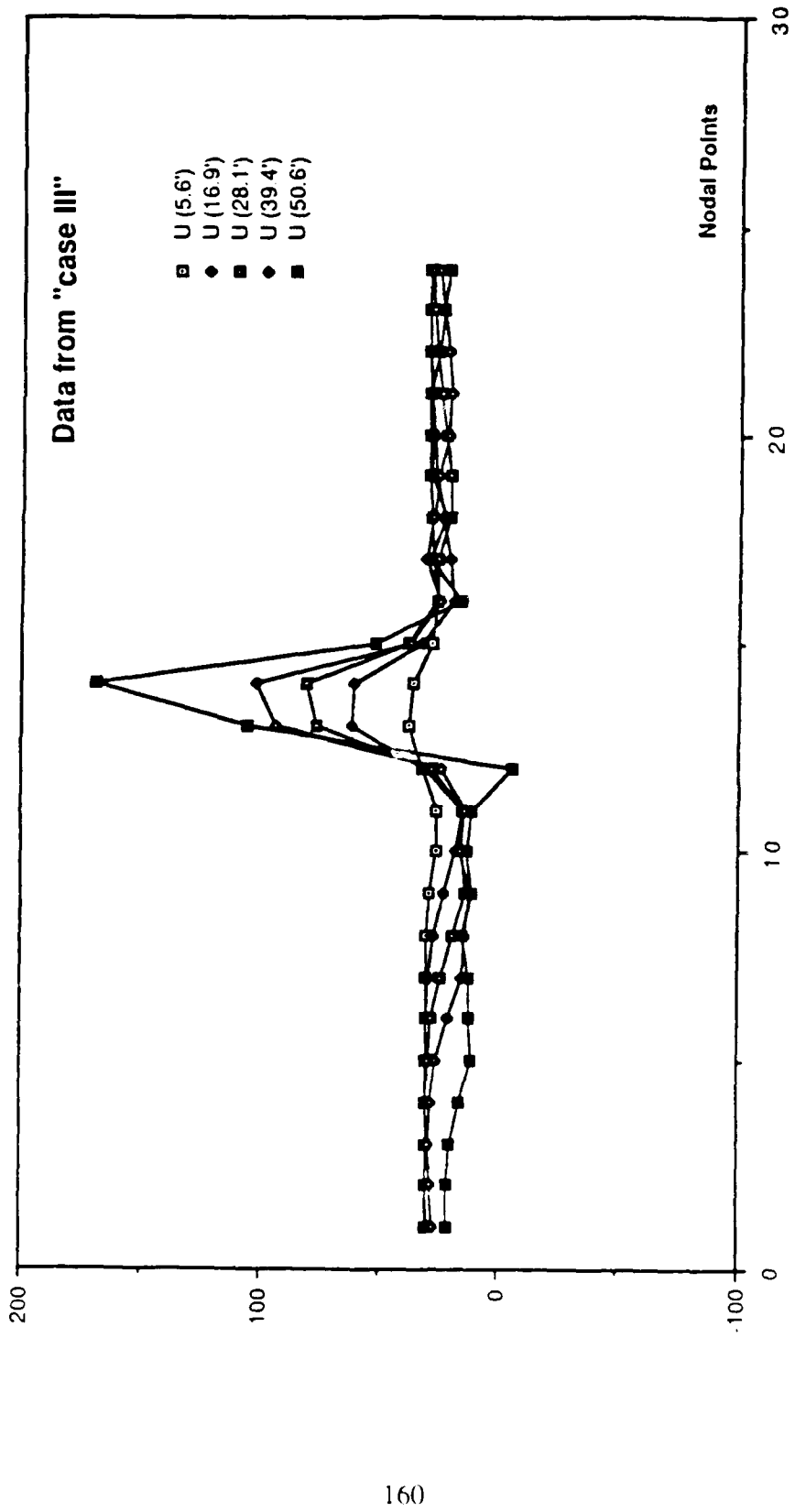


Fig. 7.30 As in Fig. 7.26, except for case III.

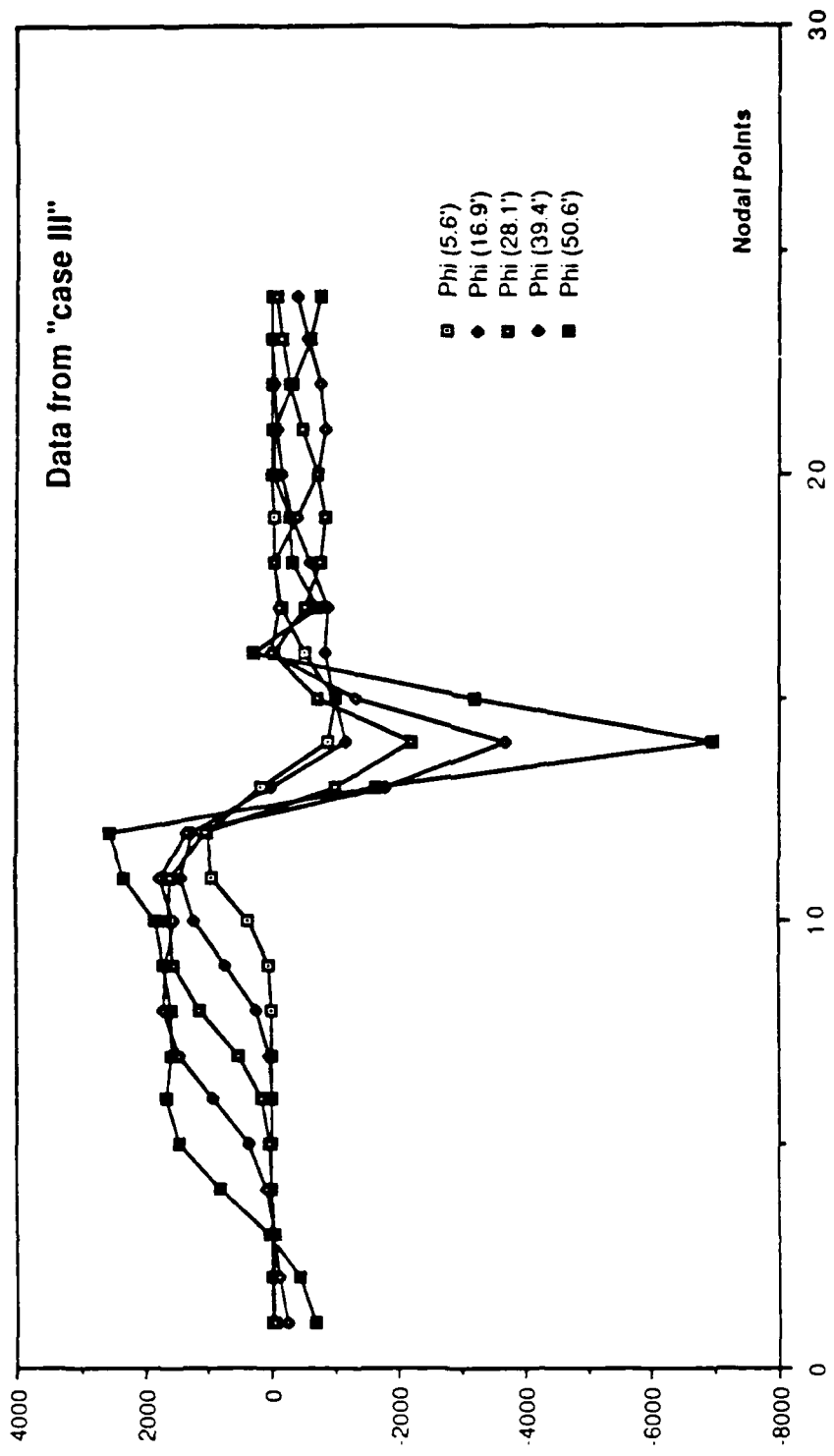


Fig. 7.31 Λ_s in Fig. 7.27, except for case III.

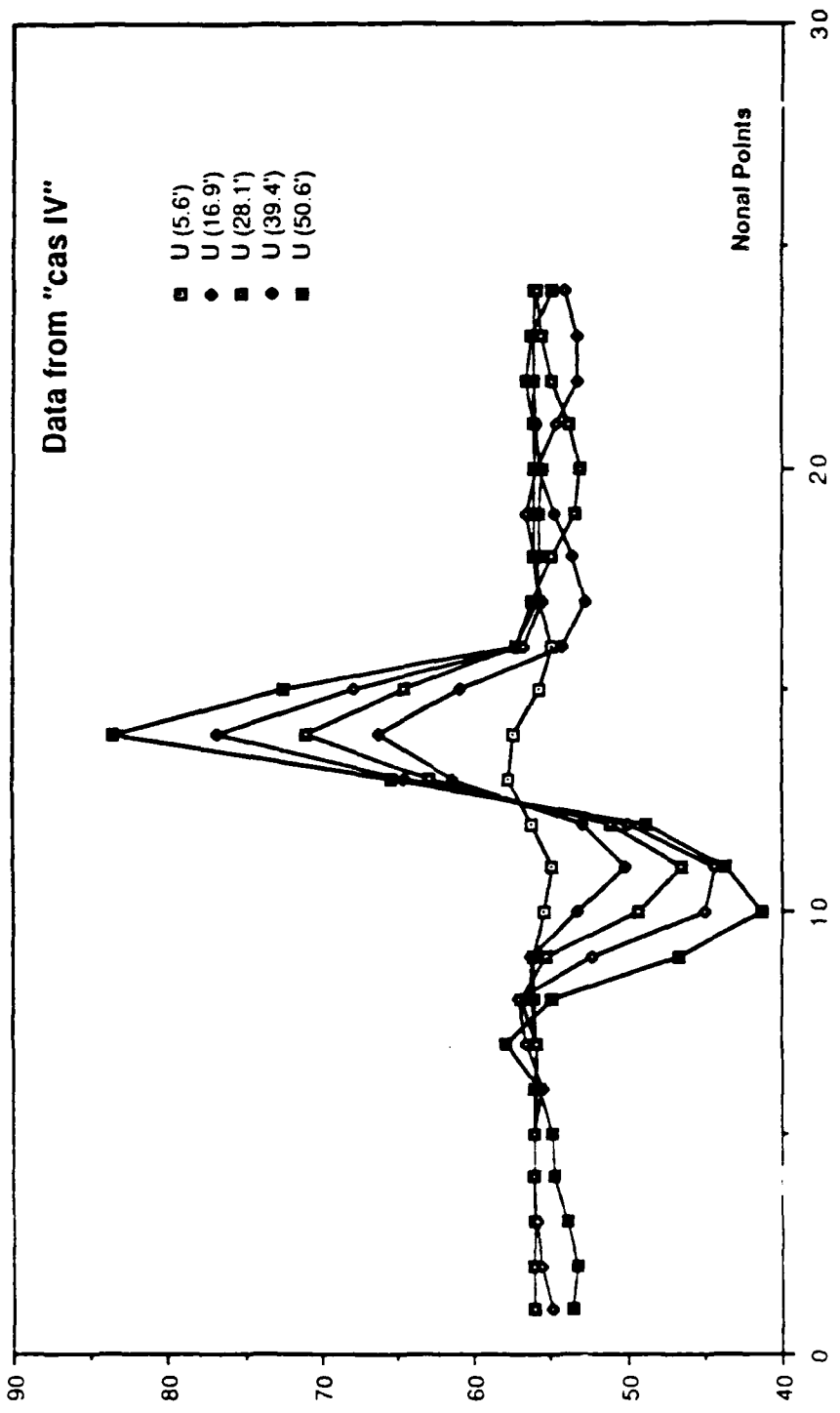


Fig. 7.32 As in Fig. 7.26, except for case IV.

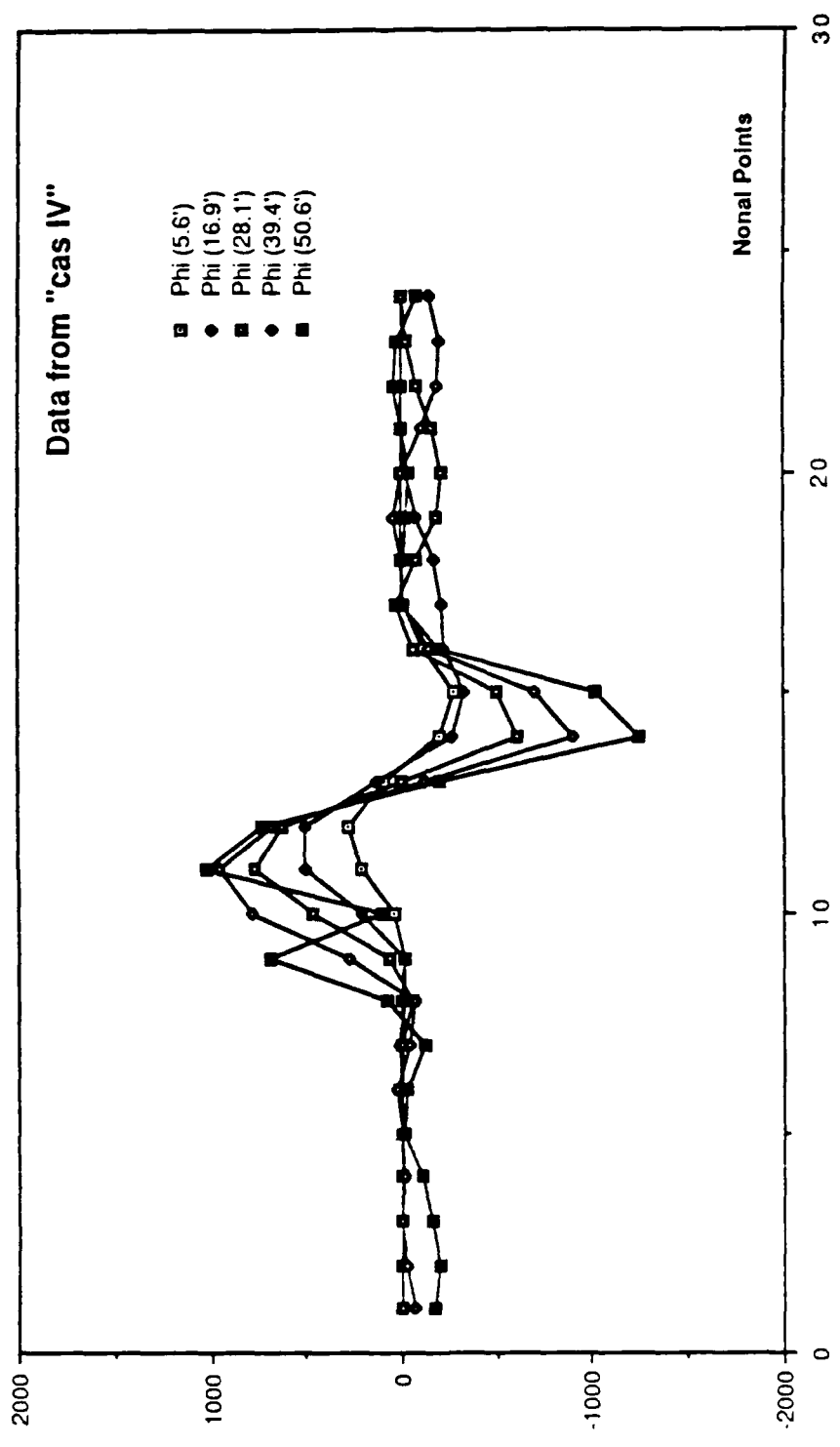


Fig. 7.33 As in Fig. 7.27, except for case IV.

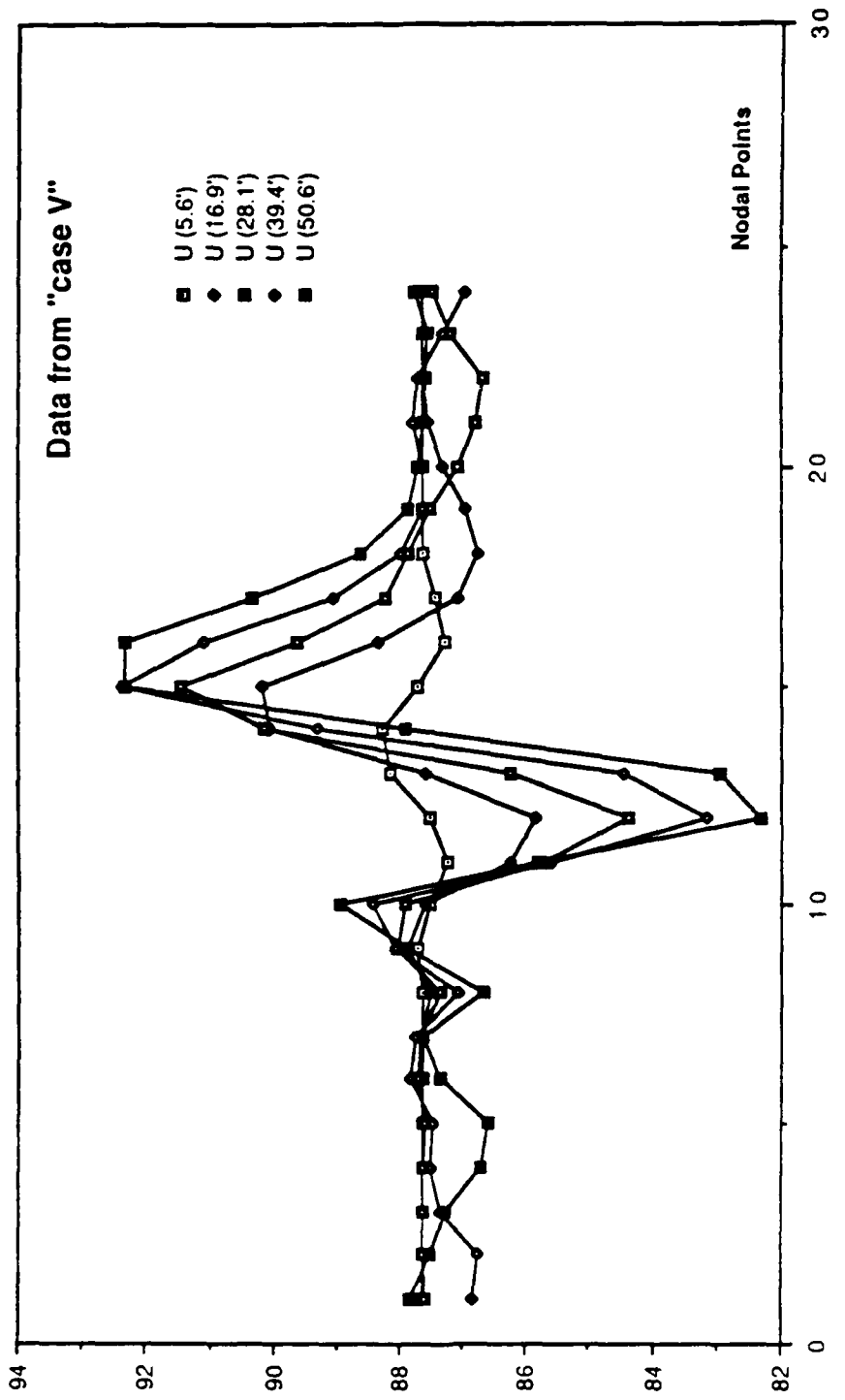


Fig. 7.34 As in Fig. 7.26, except for case V.

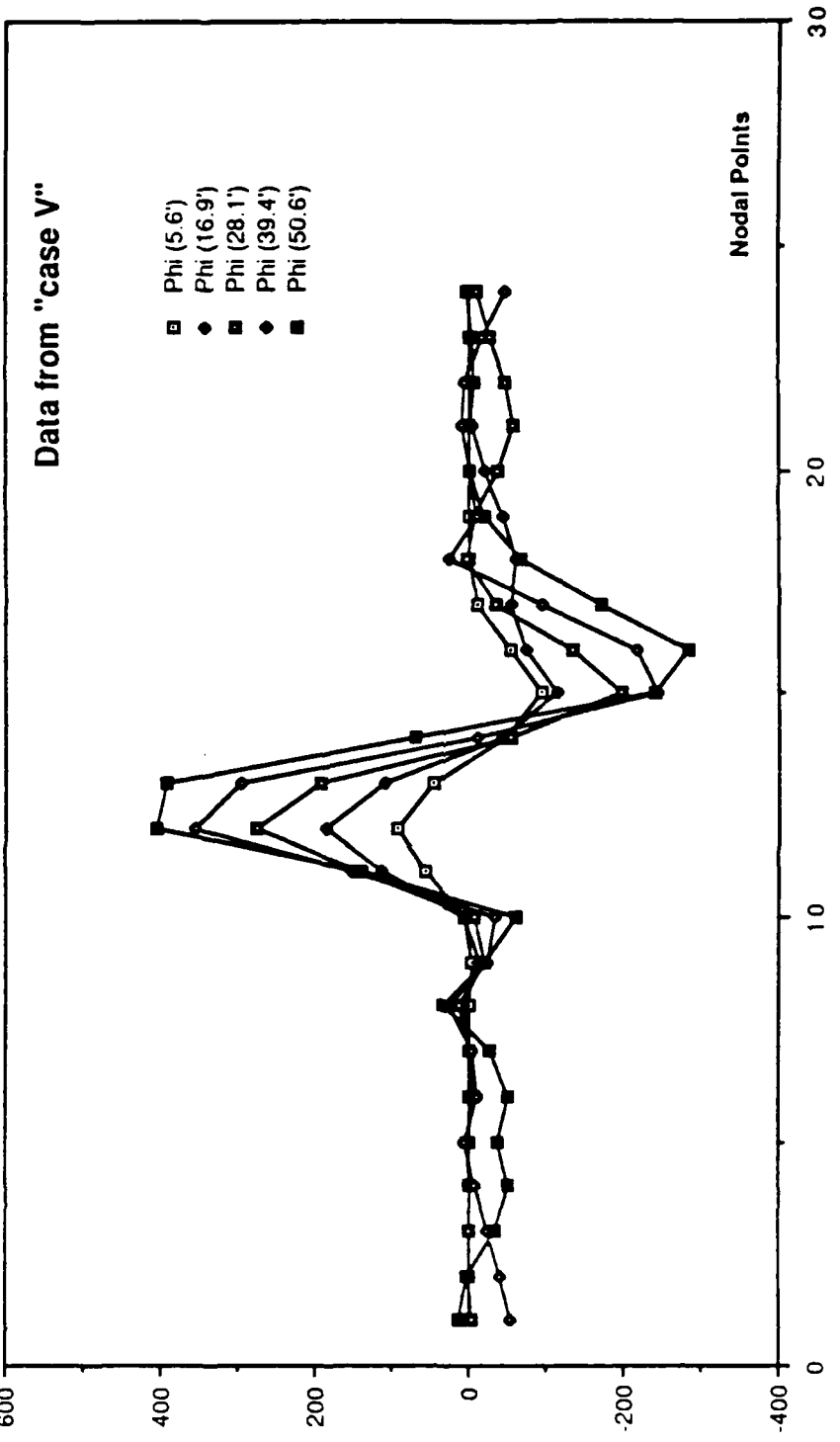


Fig. 7.35 As in Fig. 7.27, except for case V.

VIII. CONCLUSIONS

In this thesis we have investigated how well a particular shallow-water finite element prediction model handles surface topography. In both experiments the flow is confined within an east-west channel with periodic boundary conditions.

In the first experiment the bottom is composed of two regions of constant and opposite north-south slope with no east-west variation, so that the bottom is either an east-west ridge or an east-west valley. In order to have the proper initial conditions, the analytic Rossby wave solutions are derived. These are obtained by solving the linearized quasi-geostrophic equations with the free surface assumed to be rigid. Each solution has a sinusoidal variation with y over one bottom slope and exponential decay over the other slope. With the simple Rossby formula the direction of propagation is determined by the bottom slope in the region which has the largest wave amplitude. These solutions are similar to the trench wave solutions obtained by Mysak *et al* (1979), who used piecewise exponential bottom profiles. The numerical solutions with the initial conditions given by the linear solutions produced smoothly propagating solutions. The phase speeds were very accurate when the Rossby formula was corrected for free-surface effects and mean depth.

In the second experiment a north-south ridge was placed across the channel with sine-squared east-west variation. The Coriolis parameter was

set to zero and the initial u and ϕ were constant. The theory of Houghton and Kasahara (1968) for the formation of hydraulic jumps was reviewed. The equations were integrated for five initial conditions. In each case a speed maximum occurred over or just downstream from the ridge and low heights were found on the lee side of the ridge. For three of the cases the solutions reached an approximate steady state. These agreed with the theory which predicted no jumps. The two other cases lead to increasing winds and decreasing heights with no steady state. These were jump cases according to the theory. In these two last cases the model resolution was inadequate to simulate the formation of the hydraulic jumps in detail.

Finally, the finite element model performed well for two very different topographic effects. Further testing is required on the jump cases with higher resolution. Furthermore, the effect of the semi-implicit discretization on the hydraulic jumps should be determined.

APPENDIX

NUMERICAL QUADRATURE

A very fast and efficient method is required for the evaluation of the integrals obtained by the Galerkin approach. For the rectangular subdivision, integration formulas are based on an orthogonal axis transformation. In this case, the integrals to be evaluated contain either products of the basis functions, products of derivatives of basis functions, or a mixture of both.

An orthogonal axis transformation will allow quadrature formulas for rectangles. We are able to transform the rectangle shown in Fig. A.1 by using the following

$$\zeta = \frac{x - x_0}{a}, \quad (A-1)$$

$$\eta = \frac{y - y_0}{b}, \quad (A-2)$$

where the values of ζ , and η at each corner are shown in parentheses. Using f_i as a basis function, we can express f_i as

$$f_i = \frac{(1 + \zeta_i \zeta)(1 + \eta_i \eta)}{4}. \quad (A-3)$$

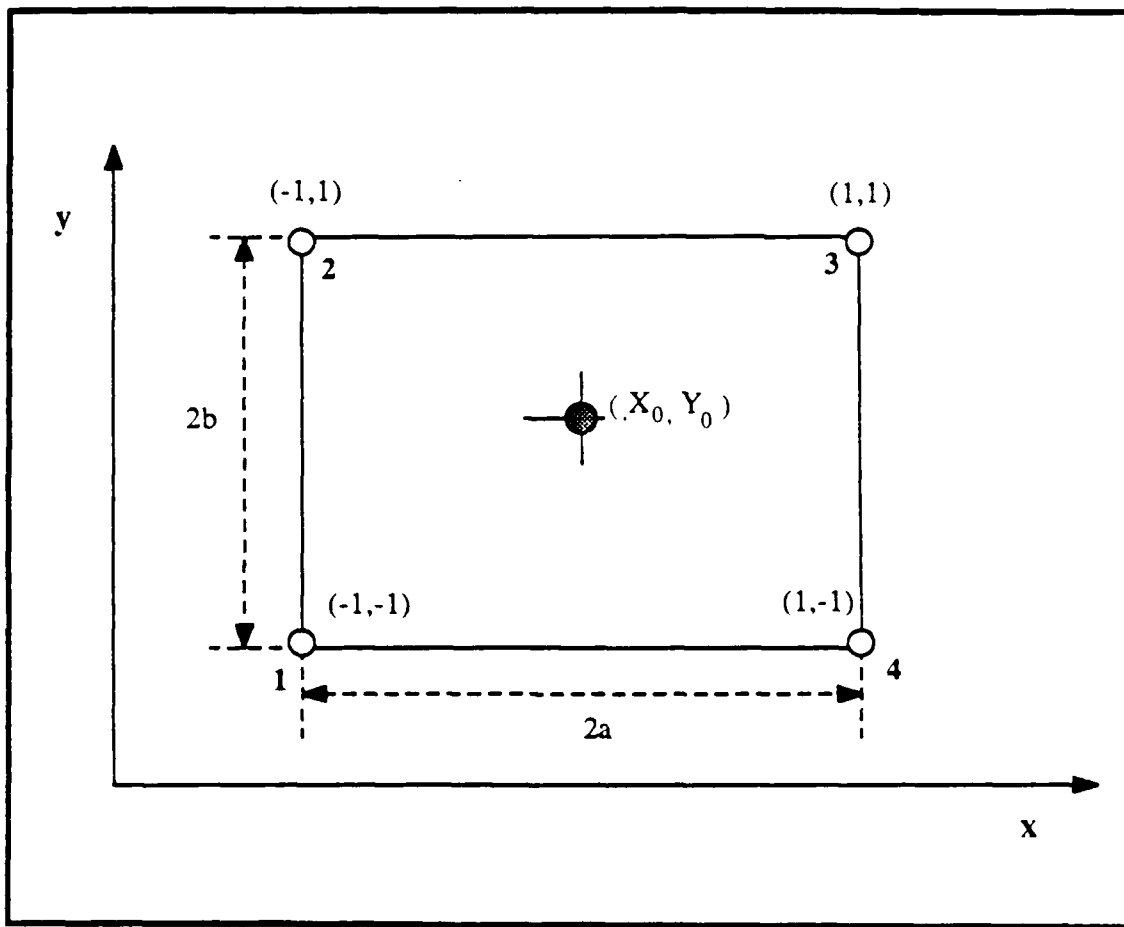


Fig. A.1 Orthogonal axis transformation for rectangular integration formulas.

Derivatives of the basis function are given by

$$\frac{\partial f_i}{\partial x} = \frac{1}{a} \frac{\partial f_i}{\partial \zeta}, \quad (A - 4)$$

and

$$\frac{\partial f_i}{\partial y} = \frac{1}{b} \frac{\partial f_i}{\partial \eta}. \quad (A - 5)$$

The interaction coefficients can now be determined for a derivative or straight inner product. The straight inner product is given by

$$\begin{aligned} c_{ij} &= \iint f_i f_j dx dy = ab \int_{-1}^1 \int_{-1}^1 f_i f_j d\zeta d\eta \\ &= \frac{ab}{16} \int_{-1}^1 (1 + \zeta_i \zeta) (1 + \zeta_j \zeta) d\zeta \int_{-1}^1 (1 + \eta_i \eta) (1 + \eta_j \eta) d\eta \\ &= \frac{ab}{16} \left(2 + \frac{2}{3} \zeta_i \zeta_j \right) \left(2 + \frac{2}{3} \eta_i \eta_j \right). \end{aligned} \quad (A - 6)$$

Also, the mixed derivative is given by

$$\begin{aligned}
 d_{ij} &= \iint \frac{\partial f_i}{\partial x} \frac{\partial f_j}{\partial x} dx dy = \frac{b}{a} \int_{-1}^1 \int_{-1}^1 \frac{\partial f_i}{\partial \zeta} \frac{\partial f_j}{\partial \zeta} d\zeta d\eta \\
 &= \frac{b}{16a} \int_{-1}^1 \zeta_i \zeta_j d\zeta \int_{-1}^1 (1 + \eta_i \eta) (1 + \eta_j \eta) d\eta \\
 &= \frac{b}{16a} (2 \zeta_i \zeta_j) (2 + \frac{2}{3} \eta_i \eta_j). \tag{A - 7}
 \end{aligned}$$

LIST OF REFERENCES

Charney, J., R. Fjortoft, and J. Von Neumann, 1950: Numerical integration of the barotropic vorticity equation. *Tellus*, **2**, 237-254.

Cullen, M. J. P., 1974a: A finite element method for a non-linear initial value problem. *J. Inst. Math. Its. Appl.*, **13**, 233-247.

Cullen, M. J. P., 1974b: Integrations of the primitive equations on a sphere using the finite element method. *Quart. J. Roy. Meteor. Soc.*, **100**, 555-562.

Cullen, M. J. P., 1979: The finite element numerical methods used in atmospheric models, Vol. II Garp Publication Series Number 17, pp. 300-337.

Cullen, M. J. P., and C. D. Hall, 1979: Forecasting and general circulation results from finite element models. *Quart. J. Roy. Meteor. Soc.*, **105**, 571-592.

Haltiner, G. J., and R. T. Williams, 1980: Numerical prediction and dynamic meteorology. John Wiley & Sons, Inc., 477 pp.

Hinsman, D. E., 1975: Application of a finite element method to the barotropic primitive equations. M. S. Thesis, Naval Postgraduate School, Monterey, California.

Hinsman, D. E., 1983: Numerical simulation of atmospheric flow on variable grids using the Galerkin finite element method, Ph. D. Thesis, Naval Postgraduate School, Monterey, California.

Houghton, D. D., and A. Kasahara, 1968: Nonlinear shallow fluid over an isolated ridge. *Comm. Pure Appl. Math.*, **21**, 1-23.

Keyser, D., and L. W. Uccellini, 1987: Regional Models: Emerging Research Tools for Synoptic Meteorologists. *Bull. Amer. Meteor. Soc.*, **67**, 326-338.

Lapidus, L., and G. F. Pinder, 1982: Numerical Solution of Partial Differential Equations in Science and Engineering. John Wiley & Sons, Inc., 677 pp.

Long, R. R., 1953: A laboratory model resembling the "Bishop-wave" phenomenon. *Bull. Amer. Meteor. Soc.*, **34**, 205-211.

Mysak, L., P. H. Le Blond, and W. J. Emery, 1979: Trench waves.
Journal of Physical Oceanography, **9**, 1001-1013.

Neta, B., R. T. Williams, and D. E. Hinsman, 1986: Studies in a shallow water fluid model with topography, in Numerical Mathematics and Applications (R. Vichevetsky, J. Vignes, eds.). Elsevier Sci. Pub., 347-354.

Pedlosky, J., 1987: Geophysical Fluid Dynamics. Springer-Verlag, New York, 1979.

Richardson, L. F., 1922: Weather Prediction by Numerical Process. London, Cambridge University Press/reprinted: Dover, 1965/. 236 pp.

Staniforth, A. N., and H. L. Mitchell, 1977: A semi-implicit finite-element barotropic model. *Mon. Wea. Rev.*, **105**, 154-169.

Staniforth, A. N., and H. L. Mitchell, 1978: A variable resolution finite-element technique for regional forecasting with the primitive equations. *Mon. Wea. Rev.*, **106**, 439-447.

Williams, R. T., and A. M. Hori, 1970: Formation of hydraulic jumps in a rotating system. *J. Geophy. Rev.*, **75**, 2813-2821.

Williams, R. T., and A. L. Schoenstadt, 1980: Formulation of efficient finite element prediction models. Naval Postgraduate School Report NPS63-80-011, 1-37, Monterey, California.

Woodward, E. T., 1981: Development of improved finite element formulation for shallow water equations. M. S. Thesis, Naval Postgraduate School, Monterey, California.

Zienkiewicz, O. C., 1977: The finite Element Method. McGraw-Hill, New York, 787 pp.

Zienkiewicz, O. C., M. Watson, and I. P. King, 1968: A numerical method of visco-elastic stress analysis. *Int. J. Mech. Sci.*, **10**, 807-827.